FACULTY
OF MATHEMATICS
AND PHYSICS
Charles University

MASTER THESIS

Rostislav Králík

Stability of dispersoids in aluminium alloys at elevated temperatures

Department of Physics of Materials

Supervisor of the master thesis: doc. RNDr. Miroslav Cieslar CSc.

Study programme: Physics

Specialization: Physics of Condensed Matter and Materials

Prague 2020

I declare that I carried out this master thesis independently, and only with the cited sources, literature and other professional sources.

I understand that my work relates to the rights and obligations under the Act No. 121/2000 Coll., the Copyright Act, as amended, in particular the fact that the Charles University has the right to conclude a license agreement on the use of this work as a school work pursuant to Section 60 paragraph 1 of the Copyright Act.

In Prague date 28.05.2020   signature

Title: Stability of dispersoids in aluminium alloys at elevated temperatures

Author: Rostislav Králík

Department / Institute: Department of Physics of Materials

Supervisor of the master thesis: doc. RNDr. Miroslav Cieslar

Abstract: The AA8079 aluminum alloy prepared by twin-roll casting is commonly used as foil stock for manufacturing of thin packaging foil. Due to the nature of the casting method and material composition microstructure of the material is not homogenous and contains a fraction of intermetallic particles clustered in eutectic colonies. As such, the material requires heat treatment before further processing. Different temperatures of homogenization annealing affect the microstrucutre of the material in different ways. The homogenized material then undergoes a series of rolling passes which causes work hardening. A recrystallization annealing is required at an intermediate gauge before rolling to final thickness to restore ductility of the material. Recrystallization behavior is affected by the present intermetallic particles, their size and distribution. The influence of different homogenized microstructures on control of the recrystallization process through was studied, recrystallization kinetics were evaluated and two main influencing mechanisms – particle stimulated nucleation and Zener drag were identified.

Keywords: Aluminum alloys, microscopy, homogenization, heat treatment, softening

Contents

1. Motivation

Certain properties of aluminium make the material desireable as a packaging foil stock in food industry. Namely, the material serves as a good barrier for liquids and vapors, a good corrosion resistance due to a passivation of material surface and the fact that aluminium, unlike other metals, does not produce toxic residues. Aluminium is also the most abundant metal present in the Earth's crust, which makes it cheap for use as the packaging foil stock [1].

Pure aluminium does not occur naturaly, but is received from ores, mainly bauxite. The so called Bayer proceess turns the bauxite into a fine aluminum oxide powder [2], which is further electrolyticaly treated. This aluminum contains other impurity elements (most commonly iron, silicon, manganese, magnesium etc.). There are various aluminum purification methods but the purification is generaly expensive. That is why it is easier for packaging foil to use alloys containing impurities from ores. The concentration ranges in which these elements form a substituional or an interstitional solid solution with aluminum is generaly low, mainly in the case of iron. The equilibrium solubility of iron in the aluminium matrix is in hundreths of percent [3]. This causes a formation of Fe-rich precipitates during a solidification of the melted foil stock. While precipitates can improve mechanical properties of the produced alloy (observed yield strength is about 10-50 times the original value depending on the type of alloy and the concentrations of individual elements) the same precipitates may cause the formation of pinholes during cold rolling to very thin gauges. Precipitates may also significantly affect the microstructure of the alloy after subsequent thermomechanical processing, mainly through an effect called particle stimulated nucleation (PSN) and through a retardation of grain boundary motion during recrystalization. The retardation effect is known az Zener pinning.

A final gauge of the packaging foil is about 6 - 11 μm. A rolling of a single sheet of the foil stock is an unstable process and may cause a tearing of the material. This is why co-rolling of two sheets of stock material to twice the desired gauge is commonly used, which stabilises the process [1]. After rolling to the desired gauge these two sheets of foil could be easily separated. The co-rolling process makes the foil more susceptible to the formation of pinholes because harder precipitates or their colonies might be imprinted into the co-rolled layer during the rolling, leaving a pinhole in it after a foils separation. A large number of pinholes is detrimental to the foils value as a barrier for liquids and vapors and makes them more susceptible to tearing. Some aluminium foils are further coated by layers of polymer.

The coated side is actively dried and the material is then coiled into a single roll. A leak of coating material through pinholes to the undried side will stick the layers together after the coiling and the entire roll becomes worthless. Therefore, a formation of pinholes should be limited during processing.

Another demand on foils is a homogenous fine grained structure resulting in enhanced ductility and strength. Homogenization annealing of the cast material is performed at high temperatures above 500 °C, which affects the precipitates formed during manufacturing of the foil stock. Significant cold working of the material is performed during rolling to the final gauge. Subsequent annealing may induce static recrystalization and the final recrystalized structure is heavily affected by the structure of the cold worked material.

The thesis describes microstructure of a AA8079 aluminium alloy used commonly as foil stock on a microscopic and mezoscopic level. Individual processes occuring in the alloy during high temperature annealing are described employing in-situ annealing experiments and post mortem characterizations. The data are then used to design an optimal homogenization annealing temperature and a temperature of intermedial recrystalization annealing in order to receive input material for a production of thin foils of desired properties.

2. The current state of knowledge

2.1. Plastic deformation and heat treatment of materials

By definition, plastic deformation is a process during which a material is deformed by an outer force in a nonreversible way. A majority of plastic deformation of metals is controlled by a motion of dislocations. Mobile dislocations interact with other defects (grain boundaries, precipitates, other dislocations) preventing their movement and causing hardening of the material on a macroscopic scale.

In the following parts an influence of microstructure on macroscopic mechanical properties of material is discussed. The focus is mainly on hardening mechanisms in polycrystaline alloys with particles of other phases present.

2.1.1. Plastic deformation of polycrystaline materials

A dislocation substructure is formed during plastic deformation of materials. During cold working of materials disordered dislocations are formed through stress activated dislocation sources. Due to grain boundaries serving as barriers for dislocation movement a pile up of dislocations occurs and the material hardens. This is so called grain boundary hardening and can be quantified by the Hall-Petch equation (Eq. 2.1). The equation is generaly considered to hold true for grain sizes of hundreds of µm to tens of nm which is in line with most polycrystaline metals prepared by standard casting methods [4].

$$\sigma = \sigma_0 + \frac{k}{\sqrt{d_G}}.$$

$$(2.1)$$

In the Hall-Petch equation σ is yield strength of the material, d_G is a linear grain size, k is a constant characterizing the material and σ_0 is a grain size independent constant also characterizing the material. This simple form of the Hall-Petch equation considers homogenous grain size disribution and is not valid in the case of heterogenous distributions.

2.1.2. Plastic deformation of alloys

Unlike single component polycrystals alloys dislocation interaction with solute atoms and precipitates should be considered.

For solute atoms a large number of interactions can be found. These include elastic interaction through latice strain caused by the presence of a foreign atom, electrical

interaction, chemical Suzuki effect, the effect of stacking fault energy difference and interactions caused by both long and short range orderings [5,6]. An equation can be used to characterize the magnitude of these effects as

$$\Delta\sigma = M \frac{3^{\frac{3}{4}}}{2} \left(\frac{1+v}{1-v}\right)^{\frac{3}{2}} G |\varepsilon|^{\frac{3}{2}} \sqrt{c} \tag{2.2}$$

where M is Taylor factor reported as 3.06, G is the Shear modulus of the material reported as 26.9GPa, v is the Poisson ratio reported as 0.347, ε is the elastic misfit of solute atoms in the matrix reported as 0.61 for Si in Al and 3.9% for Fe in Al and c is the solute contentration in the matrix [7].

Precipitates are generally much stronger barriers for a dislocation motion than solute atoms. Depending on the size of the precipitate mobile dislocation can either cut the precipitate (called the Friedel hardening mechanism) or form a loop around the precipitate (called Orowan looping) [8]. Cutting through precipitates is generaly more energeticaly beneficial as far as the precipitate is fairly small. The type of interface between the precipitate and the matrix also has to be taken into account – it is easier for dislocations to cut through a coherent precipitate. Influence of Orowan strenthening mechanism for incoherent dispersoids can be calculated as

$$\Delta\sigma = \frac{2\alpha G b}{\lambda - r} \tag{2.3}$$

where b is the Burger's vector length of a dislocation reported as 0.286 nm for aluminum assuming a standard {111} slip plane in a FCC system, r is the diameter of a particle, α is a constant of dislocation line tension and λ is average interparticle spacing [9].

2.1.3. Softening, recovery, recrystalization and grain growth

A part of a mechanical energy spent to during cold rolling is stored in a form of new lattice defects, mainly dislocations and stacking faults. A dislocation substructure is often formed by plastic deformation consisting of dense dislocation walls in between which lie coherent areas of the material with low dislocation density. This substructure is called a cell structure. Due to deformation the Gibbs free energy of the material is higher than the equilibrium energy, serving as driving force towards the equilibrium state and making the substructure less stable. The transition towards the equilibrium state is performed through recovery, recrystalization and grain growth. Some of these processes can be further classified as static or dynamic ones. Since dynamic processes consider the presence of external stress, which is not the case presented in the thesis, we will further focus only on static processes [10].

The intensity of above mentioned processes is temperature dependent because diffusion is always behind them. Recovery generaly occurs at lower temperatures than recrystalization and grain growth. Local elastic strains disappear and point defects generally anihilate during recovery. Dislocations are subject to temperature activated climb as well as cross slip during recovery, causing a motion and anihilation of dislocations and a formation of low angle grain boundaries. Cross slip is essential for dislocation anihilation. Split dislocations can not cross slip and should form perfect dislocations first. Materials with a high stacking fault energy are thus more prone to recovery due to a smaler seperation of partial dislocations [11]. Similarly, materials with low stacking fault energy generally do not recover at all and recrystalization is the first softening process. Because the aluminium stacking fault energy is relatively high compared to other commonly used metals recovery is a regular process [12].

Recrystalization is a process during which the original grain structure, dislocation and subgrain structure are replaced by newly grown grains [10]. Even though the grain newly formed during recrystallization could be larger than the original ones, it is still not considered as a grain growth. Grain growth is a separate process during which the driving force of growth is caused by the tendency to decrease the materials nonequilibrium grain boundary energy towards its minimum. The driving force of recrystalization is a removal of the remaining stored deformation energy by a replacement of deformed grains by undeformed ones and thus decreasing the dislocation density by several orders of magnitude. The speed of the recrystallization process depends on the magnitude of the driving force and grain boundary mobility of the material. Grain boundary mobility M is a temperature dependent property of the boundary given by the equation

$$M = M_0 \exp\left(-\frac{E_{GB}^M}{k_B T}\right),$$ (2.4)

where k_B is the Boltzmann constant, T is the thermodynamic temperature of the material, M_0 is a temperature independent constant and $E_{GB}{}^M$ is activation energy for grain boundary mobility, and for Al alloys is often reported as 0,1eV [13].

The process of nucleation and growth of grains during recrystalization can be described by the Avrami equation (Eq. 2.4) [14]. For isothermal annealing the equation can be written as

$$x(t) = 1 - \exp\left(-X_e(t)\right),$$ (2.5)

where x is the volume fraction of recrystalized grains and X_e is the so called extended volume fraction of recrystalized grains. The extended volume is often written as

5

$$X_e = kt^n, \tag{2.6}$$

where k is a temperature dependent constant related to the activation energy of the recrystalization process and n is a temperature independent constant, which varies with the dimension of the recrystalization process [14,15].

Generaly the value of n is between 2 and 4 increasing with the dimensionality of the process for standard static recrystalization in a single phase material. Additional structural features might impede recrystalization and thus lower the exponent [16,17]. The value of n can be received by plotting a double logarithm of the recrystalized volume against a logarithm of time of the isothermal recrystalization as follows

$$\ln\left(-\ln\left(1 - x(t)\right)\right) = n\ln(t) + \ln(k). \tag{2.7}$$

In an ideal case this plot would be linear however additonal effects such as finite volume of the sample or surface grain nucleation can change this expected form of the curve [17]. In an ideal case of an infinite single phase material with random grain nucleation the value of n is equal to 4. Lower dimensions of random nucleation space further reduce the value by 1. For example random nucleation in a 2D space has n value of 3 and so on. A study made on iron materials also states that an interaction between recovery and recrystallization can also reduce the n parameter as the Avrami model does not include recovery [18]. Another study made on a 7XXX aluminum alloy shows that the retarding effect of impurities is a reason for the n value decrease [19]. In general any effect retarding grain boundary motion would have an effect on recrystallization kinetics and on the n parameter.

There are multiple ways to measure the recrystalized grain volume fraction. The most straightforward way is from LOM by performing a Barker etch or by SEM by performing EBSD. However both of these methods can be quite time intensive when measuring a large number of samples. This is why a microhardness model of measurements is often employed. A simple equation

$$x(t) = \frac{HV_0 - HV(t)}{HV_0 - HV_R} \tag{2.8}$$

where HV_0, $HV(t)$ and HV_R are measured Vicker's microhardness values of a non-recrystallized sample, at the time t during recrystalization and of a recrystallized sample respectively [20]. This model should give a rough estimation of the recrystalized volume fraction required to determine the n constant of the Avrami curve.

Grain growth occurs in materials with a high grain boundary energy, which is often influenced caused by the type of a used manufacturing process. A deviation from these

processes is the so called secondary recrystalization also called abnormal grain growth which occurs under certain conditions [21].

Because these processes increase grain size and remove lattice defects dislocation motion becomes easier and the material is softer.

2.1.4. Particle stimulated nucleation and Zener pinning

The presence of particles, their size and distribution have high importance during the recrystallization of the material.

Numerous experiments show that the surrounding area of a nondeformable particle contains a higher concentration of dislocations after cold working [22]. This high deformation serves as a primary site for nucleation of new grains during recrystalization (particle stimulated nucleation – PSN). Larger particles are responsible for larger deformation zones, which in turn promotes a faster recrystalization process [23].

While large particles promote recrystalization by creating high dislocation density zones in their vicinity, small homogenously spread particles create a mesh of inpenetrable obstacles for dislocations and grain boundaries, preventing or retarding recrystallization [24]. To properly impede dislocation motion a homogenous dispersion of particles close to their critical radius is required. The critical radius r_0 is given by the relation between energy needed for the dislocation or grain boundary to cut through (Friedel mechanism) or loop around the particle (Orowan mechanism). The energy required to penetrate a particle increases with its radius r as a square root of the radius. The energy required to loop around a particle decreases with increasing radius as r^{-1}. The relation of these conflicting effects is visualized in Fig. 2.1.
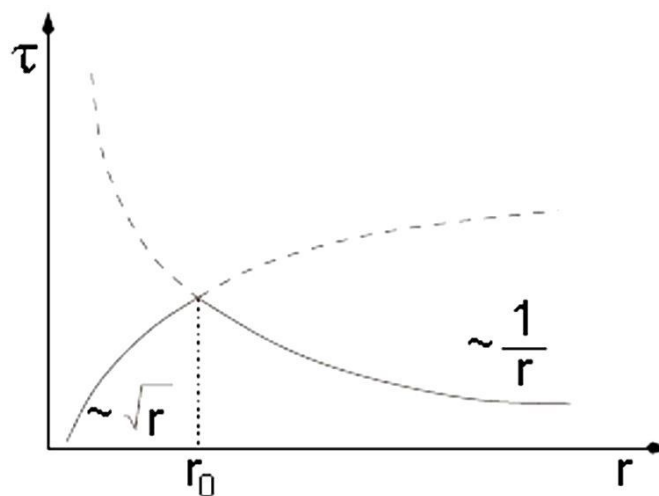

Figure 2.1: Friedel vs Orowan mechanism depending on the particle radius [25]

The backpressure presented by the particles in the material can be quantified by a single number – the Zener backpressure coefficient

$$P_z = \frac{3f\gamma}{4R},$$ (2.9)

where f is the volume fraction of particles, γ is the moving grain boundary energy and R is a linear radius of the retarding particle [24].

PSN is an effect caused by the presence of large non deformable particles in the matrix, while Zener pinning is generaly attributed to the presence of small closely spaced dispersoids [26]. The critical size of particles in order to promote either PSN or Zener pinning in the material depends on the degree of cold working the material undergoes prior to recrystalization annealing [26]. Generally a larger reduction implies more stored energy and the lower the required particle size for initiation of PSN. In general the size of particles that promote PSN in Al is always in units of μm [23].

2.1.5. Ostwald ripening

Ostwald ripening, also called competitive growth or simply coarsening, is an effect which occurs in a wide variety of systems ranging from solid particles emulsions to liquid droplets in gas clouds to solid particles in solid solutions [27].

A simple qualitative explanation of coarsening of particles in all systems has existed for decades. It claims coarsening is a result of a two phases system existing outside the state of thermodynamic equilibrium. A system with a large number of small particles has a high amount of excess surface energy associated with the particles and as such tends towards minimalization of this energy by a dissolving of a fraction of these particles and redistribution of their content into coarser particles [28].

Commonly this effect occurs in metals in general as well as in aluminum alloys during annealing at elevated temperatures [29].

2.2. Aluminium and its systems

The following chapter focuses on the studied systems of aluminium in combnation with some of its alloying elements present in the studied materials. The focus lies mainly on the properties of these systems and the commonly occuring intermetalic phases in them.

The most widely used norm for classifying aluminium alloys is the EN 573-1 norm, which classifies them by the most abundant alloying element [3].

The commercialy pure aluminium 1XXX is the only series in this norm where the XXX

numbers have a particular meaning as the last two numbers denote the minimal concentration of aluminium above 99%. In all the other series the three numbers used are purely arbitrary [3].

Most of the systems of aluminum in combination with other metals are fairly non trivial, containing many intermetalic phases with wide concentration ranges of existence. Some elements form simple eutectic systems with aluminium (such as silicon or zinc) as described in part 3.3. In some cases a monotectic system can form with some (sodium, potassium) elements. In general the liquid phases undergoes an eutectic transformation and a substitutional face centered cubic solid solution with high aluminium content is formed [3].

While most metals are highly soluable in liquid aluminium, there is no element fully soluable in solid aluminium. Highest soluability is attained at the eutectic, peritectic or monotectic temperatures with the exception of tin. Due to a low solubility of metals in solid aluminium intermetalic phases containing high amounts of alloying elements form.

The main alloying elements in the studied alloys are iron, silicon and manganese. Our focus is on the low level alloyed systems because the concentration of solutes does not exceed 3%. The studied alloy shows trace amounts of titanium, though they are low to have any significant effect and will not be further discussed.

2.2.1. Pure aluminum
Pure aluminum is a silvery, malleable metal with FCC structure. The matrix of the studied materials is expected to retain this structure [3].

Pure aluminum or pure aluminum based alloys are mainly valued for their outstanding electrical and chemical properties. Aluminium is also significant for its good heat conductivity, corrosion resistance and ductility. On the other hand, pure aluminium has a fairly low yield point, which could be further increased by the concentration of impurities, most commonly silicon and iron. Pure aluminium can be subjected to work hardening, but in general will not reach the hardness of its age-hardenable alloys even after intense work hardening [30].

2.2.2. Aluminum – silicon
Silicon forms a simple eutectic system (Fig. 2.2) in combination with aluminium in which no intermetalic phases form as far as the concentration of impurities remains at zero. At eutectic concentration of 12.6 wt.% of silicon alpha and beta phases coexist containing

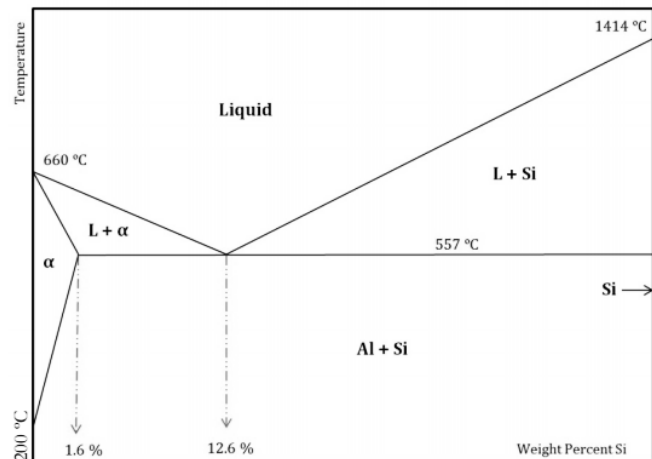1.65 wt.% of silicon and 0.5 wt.% of aluminium respecively. The eutectic temperature for this system is 580°C [3].

Figure 2. The schematic phase diagram of Al-Si.

Figure 2.2: The binary Al-Si phase diagram [31]

When present as the most primary alloying element silicon forms the basis of the 4XXX series of aluminium alloys. The mere presence of impurities causes

their precipiation in a form of impurity rich precipitates. Silicon is also highly common in alloys of other series [3].

2.2.3. Aluminum-iron

Iron is the most abundant impurity present in nearly all commercialy attainable aluminium ores, which makes it the most abundant alloying element in commercial alloys. In some cases iron is further added, although rarely above 1% concentration. At high aluminium concetration this system behaves as a eutectic system (Fig. 2.3) when alloyed to 1.7% to 2.2% of iron concentration.

The equlibrium phase is denoted as Al_3Fe sometimes denoted as the Al_7Fe_2 phase or, in the case of some of the more recent publications, the $Al_{13}Fe_4$ phase [32]. This phase nucleates directly from the liquid phase. In rapidly cooled alloys the Al_6Fe non-equilibrium phase may form.

While iron is highly soluable in liquid aluminium, the solubility in the aluminium matrix is among the lowest when compared to other metals at only 0.04% of iron concentration. When iron is present above these concentrations precipitates form in the alloy containig both iron and other elements if present.
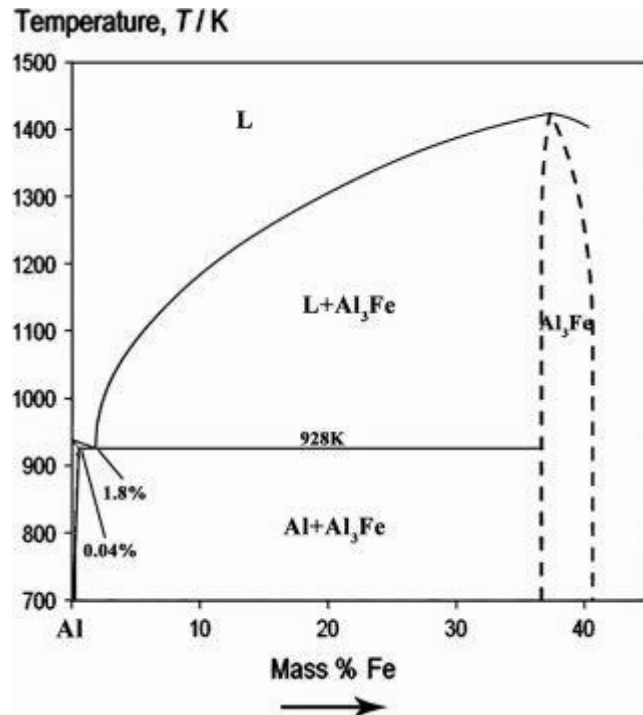

Figure 2.3: The binary Al-Fe phase diagram [32]

The $Al_{13}Fe_4$ phase is monoclinic [33] often present in a form of platelets or thin needles [34,35]. Being the equilibrium phase it forms from the supersaturated matrix by diffusion in the case of rapidly cooled alloys [36]. Other phases, such as the orthorombic Al_6Fe may be present in these alloys when manufactured under certain conditions [37].

A fine grained structure often forms as a result of presence of intermetalic phase particles, preventing dislocation motion and causing grain boundary hardening while lowering the alloys formability and elasticity. The Al_6Fe phase, if present, might increase the materials susceptibility to crack formation and propagation lowering the materials ductility [38].

2.2.4. Aluminium-iron-silicon

Iron and silicon are basic elements of 4XXX and 8XXX series of alloys.

Close to Al rich corner three equilibrium intermetallic phases might be present. Those are the Al_8Fe_2Si phase, so called α-AlFeSi phase, sometimes denoted as $Al_{12}Fe_3Si$, the Al_5FeSi phase, the so called β-AlFeSi phase and $Al_{13}Fe_4$ phase at low Si contents. At very low Fe contents only Al and Si matrices coexist. Similarly, if the Si content is low enough, the stable $Al_{13}Fe_4$ phase forms instead. Along with these equilibrium phases some metastable phases might be present. Those are the Al_3FeSi phase and the Al_4FeSi phase, also called the γ AlFeSi and δ AlFeSi phases respectively. The ternary AlFeSi diagram is shown in Fig. 2.4.
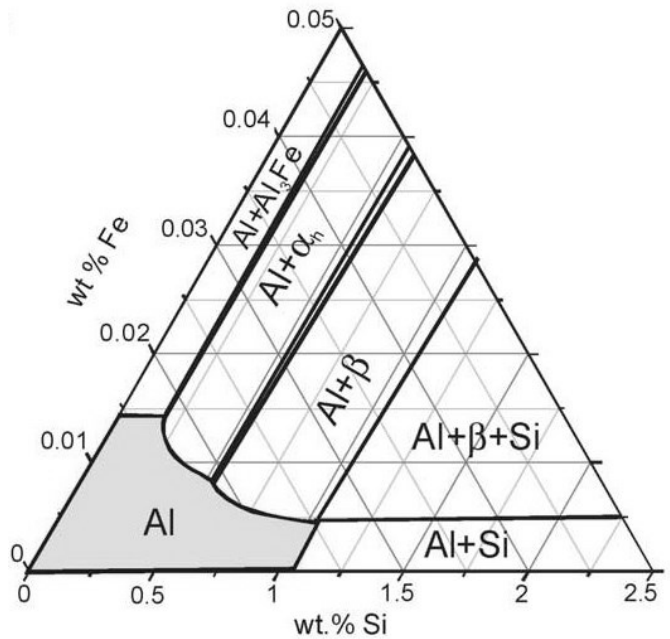

Figure 2.4: The Al rich corner of the ternary Al-Fe-Si phase diagram [39]

In nonequilibrium alloys both the equilibrium and the metastable phases can coexist along with some of the phases from the aluminium-iron system, notably $Al_{13}Fe_4$ and Al_6Fe. Chinese script and platelet morphologies are common for these particles. The alpha phase can be observed as either hexagonal, face centered cubic [40] or simple cubic [41]. The beta phase can be observed as either monoclinic or orthorombic [40].

Mechanical properties of this system are similar to those of the aluminium-iron system. Alloys containing iron and silicon are heat treatable and subject to precipitation hardening. Silicon can be added to facilitate precipitation of iron from the supersaturated matrix.

2.3. Resistivity and Mathiessen rule

Conduction electrons in metals are subject to dispersion causing electrical resistivity. This resistivity is a parameter of a material that is temperature and lattice defect dependent. In a way, resistivity can be used to describe the magnitude of lattice deformation. An experimental method called resistometry is based on measuring the temperature dependence of resistivity since electrical resistance R of a sample can be easily measured. By definition of Ohm's law it is the ratio of voltage between ends of a sample and the electrical current flowing through it. The relation between resitance and resistivity is

$$R = f . \rho, \tag{2.10}$$

where f is the formfactor of the sample, and for simple geometry is equal to

$$f = \frac{l}{S}, \tag{2.11}$$

where l is the length of the sample and S is the size of its cross section.

Mathiessen's rule

$$\rho(T) = \rho_T(T) + \rho_P, \tag{2.12}$$

applies to the materials resistivity if the situation is simplified to consider homogenous dispersion of independent defects. This rule splits resistivity into additive elements – the temperature dependent element ρ_T, which stems from dispersion on the crystal lattice phonons nad temperature independent element ρ_P stemming from lattice defects, which remains even when cooled to the temperature of liquid helium 4.2 K [42].

Different types of lattice defects affect resistivity differently. Considering independent defects we can further split the temperature independent part into several aditive components connected with different defects

$$\rho_P = \sum_k \rho_{Pk}, \tag{2.13}$$

where ρ_{Pk} is the total element of resistivity added by k-type defect. Considering homogenous dispersion of defects each element can be written as

$$\rho_{Pk} = \chi_k c_k, \tag{2.14}$$

where χ_k is a constant for each of the k-type defects and c_k is its concentration (or density).

As with other simplified models the conditions of their validity are rarely fulfilled. In real materials the χ_k constant is temperature, concentration and dispersion dependent [42].

Since grain boundaries, dislocations and precipitates are considered when calculating resistivity through Mathiessen's rule it is possible to pinpoint temperatures at which recovery, recrystalization and phase transformations occur. Resistivity rapidly changes during these

13

processes and in the resitivity annealing spectrum (negative derivative of resistivity) they are represented by local extrema. Significant changes in matrix saturation can also be identified. The contributions of various material defects to the total resistivity of aluminum are listed in Table 2.2.

For changes in matrix saturation it is important to note that the magnitude of the change differs for different solute elements. Resitivity related to single weight percent of different elements present in our materials outside and inside the matrix is listed in Table 2.1.

Element	In Matrix	Outside Matrix
Fe	2,56	0.058
Si	1,02	0.088

Table 2.1: Resistivity contributions of alloying elements outside and inside the aluminum matrix in μΩ.cm per wt. % [3]

Defect	Resistivity contribution
Vacancy	3.4 μΩ.cm/at%
Dislocation	$1.8.10^{-13}$ μΩ.cm^3/unit dislocation density
Grain boundary	$2.7.10^{-16}$ μΩ.cm^2/unit boundary surface

Table 2.2: Resistivity contribution of material defects in aluminum [43]

These elements are aditive to resistivity of pure aluminum, which is 2.56 μΩ.cm at room temperature and 0.25 μΩ.cm in liquid nitrogen.

Since a sample with exact dimensions reflecting the sensitivity of resistometric measurements could not be easily prepared, it is often simpler to measure properties which are independent of the formfactor. This includes normalized values of resistance and normalized annealing spectrum derivative which are essentialy the same as the normalized values of resistivity or the so called residual resistivity ratio (RRR). RRR is calculated as

$$RRR = \frac{R(293\ K)}{R(4.2K\ )} = \frac{\rho(293K)}{\rho(4.2K)}$$ (2.15)

where $R(T)$ is the resistance of the material at temperature T. Since measurements in liquid helium are rather difficult measurements at liquid nitrogen temepratures are used instead.

At low temperatures material defects are the major contributors to the resistance of the material. A high RRR ratio then indicates a higher purity of the measrued material or a presence of less defects in the material.

2.4. Aluminum foil stocks, their casting and processing

The goal of aluminum foil production is to produce a thin flexible sheet of material that is corrosion and tear resistant and maintains its ability as a barrier for gases and liquids. Through the years several types of alloys have risen to prominence in this field, mainly the alloys of the 1XXX, 3XXX and 8XXX type [44]. The 3XXX series contains manganese as a primary alloying element. The 8XXX ones used as foil stock contain mainly iron and silicon as do the 1XXX alloys. The quality of the produced foil depends heavily on the selected casting method as well as a sequence of processing steps taken before rolling to the final gauge.

Every casting method is affected by the non-uniformity of cooling rates across the cast strip or ingot. This in turn causes an inhomogenous structure of the cast product, which constitues of different grain sizes and distributions of alloying elements. The distributions of alloying elements can then further affect precipitate formation causing a different size, distribution and even structure of these precipitates across the strip or ingot. This effect is called segregation.

Segregation is further distinguished as macro- and microsegregation. These effects differ in the length scales on which they occur. Macrosegregation is only considered in order of centimetres and metres [45].

2.4.1. Twin roll casting method

In twin roll casting the melt is poured inbetween two water cooled rolls (Fig. 2.5). The material solidifies on the surface of the rolls and is then rolled producing a sheet of desired thickness [46]. While the method itself was patented in the late 19th century actual use for it was not found until midway through the 20th century. The reason for it is that there is only a narrow range of materials castable by this method and the ones that are castable are susceptible to casting defects such as but not limited to sticking, buckling and surface bleeding [46]. A fairly low productivity also had to be considered historicaly for industrial use of this method [47]. Aluminium alloys were among the first to utilize this method producing a sheet 0,5-10 mm thick depending on the manufacturer and the particular cast material [48]. While the strip width does not affect the casting process as thickness does it is still more industrialy beneficial for a wider strip to be cast. Currently the strip width in the order of

15

metres is attainable [44]. It was shown that higher production of material can be reached through casting at lower gauges [48], but thinner sheets are more susceptible to mechanical damage during rolling.

The main benefit of this method, especialy for casting materials used as foil stock, is that the cast material is already only several milimetres thick. This potentialy eliminates several hot and cold rolling passes during downstream processing. The acquired material is rapidly cooled, the cooling rates for twin roll casting - cited as 10^3 K/s for certain types of twin-roll casters - severely outweigh the cooling rates for other conventional casting methods such as direct chill casting, which is said to have cooling rates below 10^1 K/s [49]. Conventionaly, the acquired sheet is reeled onto a roll and undergoes homogenization annealing before further processing.

Centreline segregation occurs in TRC materials [50] which has been observed in various alloys of different series [51,52] as well as the 8XXX series alloys [53]. Centreline segregation is a form of microsegregation occuring in the centre of the cast strip due to a high saturation of alloying elements in the
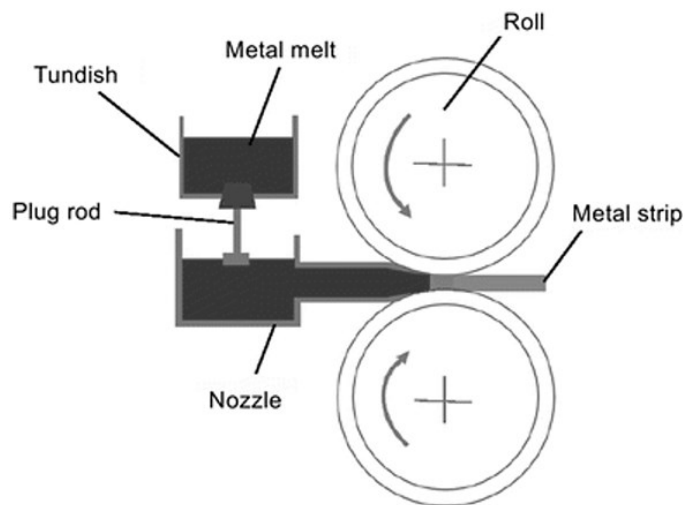

Figure 2.5: The twin-roll caster schematic [54]

last remnants of the unsolidified melt at the centre of the strip during casting. Centreline segregation can be an issue during further processing and rolling to thin gauges as a high degree of segregation can produce dense clusters of particles possibly unsoluable by homogenization annealing leading to a heterogenous structure and increased pinhole formation [55]. Similarly the aggregates of precipitates can lead to a localization of mechanical deformation during subsequent rolling steps and thus influence grain structure of the strip after a recrystallization annealing. High degree of segregation can be suppresed when lower casting speeds and thinner casting gauges are used [55]. Other defects can also lead to formations of pockets of precipitate rich regions such as hot tears and surface bleeds. Both of these defects create voids in the material which fill with solute enriched melt similarly to the centre of the strip. The nature of the TRC strip however does not allow for the formation of macrosegregation as the thickness of the strip is lower than the length scales at which

macrosegregation generaly occurs.

Similarly, hetrogenous grain distribution is commonly observed in TRC strips. Heterogenous grain distribution can prove destructive when rolling to very thin gauges without previous homognization as a result of heterogenous load distribution in the strip causing a strip break [55].

Regardless of the quality of the strip the inhomogenities in structure can never be fully avoided and a homogenization annealing should be generally performed.

2.4.2. Foil stocks and their processing

As previously discussed all of 1XXX, 3XXX and 8XXX series were commonly used as foil stock. However due to poor corrosion properties of 3XXX series alloys shift was made towards 1XXX and 8XXX alloys [44]. Alloys of both of these series have similar compositions, however the 1XXX series containins only up to 1% of alloying elements. This may be beneficial in preventing certain undesireable effects during casting, but the overall strength of the foil may suffer from it. The AA8079 contains a higher Fe/Si ratio than other commonly used alloys [56].

Mechanical properties of the cast strip strongly depend on casting parameters especially strip thickness and casting speed are important as they affect the microstructure of the strip by a modification of cooling speeds at different points of the strip cross-section. Thinner strip however

Figure 2.6: A 3mm strip cross section as observed by Birol [57]

undergoes a higher degree of deformation and might behave differently during downstream processing. Lower casting speeds have been shown to lead to a material with a coarser grain structure, however given a sufficient strip thickness the centre of the strip is unaffected by the casting speed [58]. While the casting speed affects the overall grain structure, the gradient of grain size is inevitable by the nature of the casting method, and very fine grains on the surface and coarser grains in the centre are always formed (Fig. 2.6).
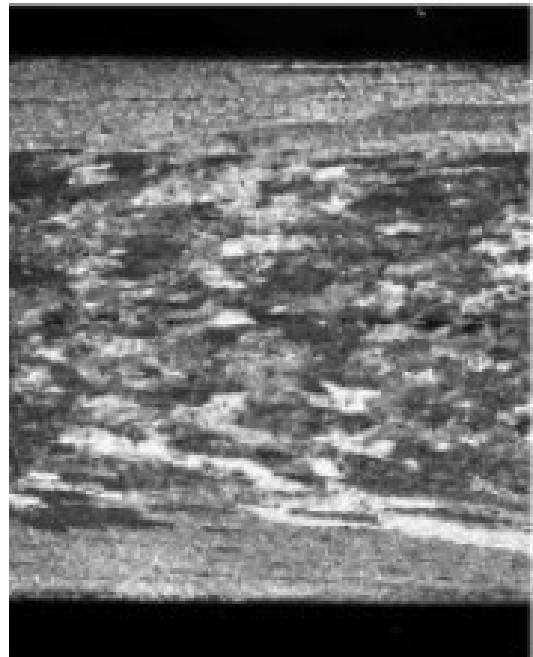
Variations of the composition of the alloy affect a type of primary phases significantly. For example the AA8079 alloy which composition could vary the Fe/Si ratio from >>1 to alloys with Fe/Si $\approx$ 5 or lower [56, 59]. As a result of the variation the alloys with the lowest content of Si contain a mixture of $Al_{13}Fe_4$ and other metastable constituent particles such as Al_mFe and Al_xFe [59]. These two types of metastable particles differ in the concentration of Fe as well as in the crystallographic structure. While these are the most commonly observed metastable particles in these alloys there have been multiple other metastable phases identified [60]. The formation of the stable $Al_{13}Fe_4$ phase is related to solidification rate of the alloy with lower solidification rates promoting its formation [61]. The partciles clusters around eutectic grain boundaries are mostly needle shaped with aspect ratios between 3 and 6 (Fig. 2.7).
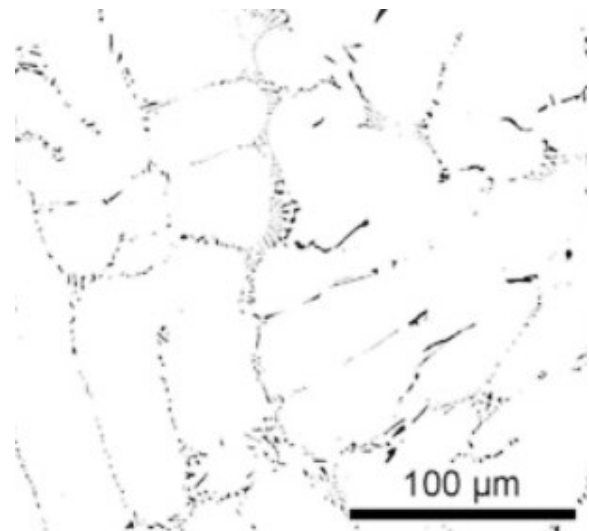

Figure 2.7: An optical micrograph of the as-cast state of low Si alloyed 8079 alloy

An increase in Si leads to a formation of phases from the AlFeSi ternary system, mostly the cubic α-AlFeSi phase [50], however, a mixture of α and β AlFeSi phases has been reported [59]. The particles again form at bounderies of eutectic cells but in comparison with low Si content alloys they are less numerous and coarser (Fig. 2.8). An adition of Mn, which substitutes Fe in these particles, modifies the phases and ternary or quarternary Al(Fe,Mn) or Al(Fe,Mn)Si particles could appear in the material. Since Mn has much higher solubility in the Al

Figure 2.8: An optical micrograph of as-cast 8011 alloy with higher Si content

matrix the ratio of Fe/Mn in the particles is usualy higher than the nominal Fe/Mn content in the alloy, because a majority of Mn remains dissolved in the matrix [57]. The studied alloy does contain Mn, however the total content is very low and as such should not have effect on
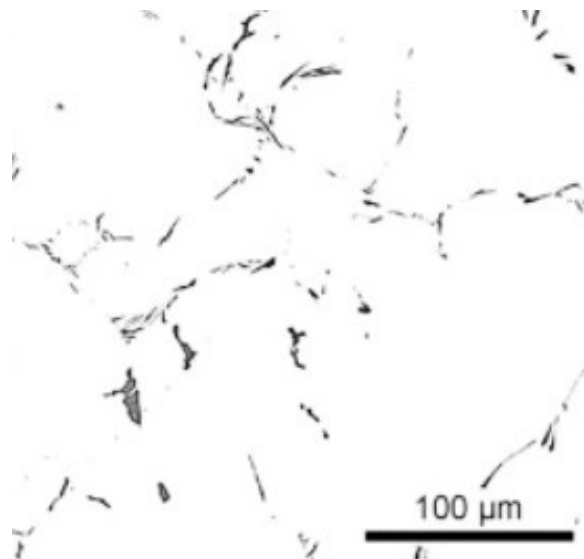
18

particle structure. A review of crystallographic information about all above mentioned phases is shown in Table 2.3.

Phase	Bravais lattice	a[nm]	b[nm]	c[nm]	α[°]	β[°]	γ[°]
$Al_{13}Fe_4$	Centered monoclinic	1.549	0.808	1.248	90	108	90
Al_6Fe	Centered orthorombic	0.649	0.744	0.879	90	90	90
Al_xFe	Centered orthorombic	0.600	0.700	0.470	90	90	90
Al_mFe	Body centered tetragonal	0.844	3.160	3.160	90	90	90
α-AlFeSi	Simple or face centered cubic	1.256	1.256	1.256	90	90	90
α-AlFeSi	Hexagonal	1.230	1.230	2.620	90	90	120
α-AlFeSi	Monoclinic	0.890	0.635	0.632	90	93.4	90
β-AlFeSi	Monoclinic	0.612	0.612	4.150	90	91	90

Table 2.3: Common phases found in the 8XXX series alloys [62]

A homogenization annealing is a necessary step in material processing resulting in a more homogenous distribution of solutes, particles and the grain structure. There are multiple ways in which homogenization can be adressed starting with simple single phase homogenization treatments when the material is held at a single temperature up to multiple phase annealing. A beneficial effect on the structure has been reported when employing two phase annealings at a higher and subsequently a lower temperature for similar periods of time were used [60]. Birol even claims that a cold rolling pass before the actual homogenization can improve the homogenization behaivour [58]. Similarly there is not a single clearly defined homogenization time that ought to be employed. In literature it is mostly the temperature range of 500 °C to 600 °C that is studied. These temperatures are generaly required in order to facilitate phase transformations and formation of the stable $Al_{13}Fe_4$ phase. Extensive studies on the kinetics of these phase transformations were performed. It was shown that after 1 h at 400 °C the transformation of the metastable Al_mFe phase into the stable $Al_{13}Fe_4$ phase begins. However the Al_6Fe phase does not transform below 500 °C [62]. An argument was also made that the rate of transformation in Al-Fe systems depends on the Si content. There is a partial, but very small, solubility of Si in AlFe phases. This solubility is higher for the stable $Al_{13}Fe_4$ phase

than the for the metastable phases. Even such a low Si content can facilitate the formation of the stable phase already during casting. These particles then serve as nucleation centres for further growth of the stable phase during homogenization thus accelerating the transformation [62]. A study made by Birol showed that 550 °C is required for the initiation of transformation of the cubic α-AlFeSi phase [50]. However, this transformation depends on specific Si content, and a lower Fe/Si ratio shifts this temperature and annealing time required to higher values [63,64].

In adition to phase transformations the particles also undergo significant changes in morphology and size. A spheroidization and precipitation of new particles was observed at 500 °C and higher temperatures [56, 59, 63]. These can either be the α-AlFeSi phase particles or $Al_{13}Fe_4$ phase particles (depending on the Si content) that precipitate for a short time before they dissolve or transform into a stable phase at higher temperatures. Remaining particles that are still present (whether they are the $Al_{13}Fe_4$ phase or the α-AlFeSi phase particles) further grow through Ostwald ripening [56 ,59]. Spheroidized and coarse particles are visible in Fig. 2.9.

The contentration of solutes in the matrix changes during homogenization. Lentz has shown that concentration of solutes in the matrix decreases first in order to reach a more equilibrium state while at 600 °C the solute level of both Si and Fe increases again , not too much, but still bellow the value measured in the as-cast state [59].
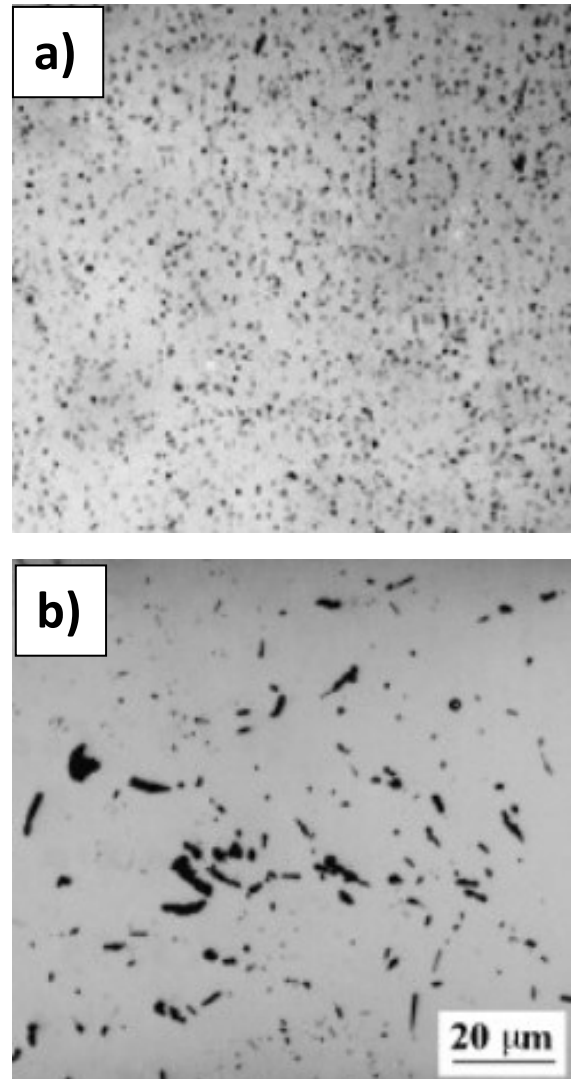

Figure 2.9: Spheroidized and coarsened particles of an alloy homogenized at a) 520 °C, b) 600 °C

The strip is continuously thinned through a series of cold rolling passes after homogenization. A work hardening imposed by rolling of the material should be released during intermediate annealing in order to restore the formability of the material for subsequent rolling passes. The material is once more annealed after rolling to a final gauge at relatively low temperatures ($\approx$ 300 °C) that should assure an evaporation of lubricants from foil surfaces but low enough to prevent potential grain growth of a recrystallized structure. Generally, higher temperatures of homogenization show a finer grain structure after a final annealing while a significant grain growth occurs at lower homogenization temperatures [65]. Birol attributes this to the presence of coarse particles and their effect on PSN and reduction of Zener drag [56].

3. Experimental methods

The chosen experimental methods were typical metalographic methods with the aim to characterize the microstructure of the material during various stages of a simulated down-streaming processing. Various microscopical methods were employed to analyze different properties of the material such as grain size, particle size and morphology, and a structure of particles.

Further methods were then employed for the characterization of mechanical properties and electrical properties of the material at different stages of thermomechanical treatment.

3.1. Light optical microscopy (LOM)

Observations were performed on Zeiss Axio Observer 7 LOM (Fig. 3.1). Depending on the selected etching method LOM allows to observe particles or a grain structure of the material.

LOM samples were prepared by mechanical polishing using SiC grinding papers, then further polished using 3µm and 1µm diamond suspensions in water and finaly OPS suspension [66].

Etching by submersion in a 0,5 % HF in a water solution for 10 s was employed in order to facilitate particle observations. These observations do not require the use of polarized light in the LOM.

The so called Barker etch method was employed to facilitate grain observations. Unlike the chemical etching for particle observations this etching is electrolytical using the matrial as an anode. The electrolyte used is the so called Barker's reagent, which is a HBO_4 in water solution [67]. The polished surface can then be analyzed by a polarized light [68].

Figure 3.1: Zeiss Axio Observer 7 optical microscope

3.2. Scanning electron microscopy (SEM)

SEM observations were performed in a FEI Quanta 200F. The SEM is equipped with back-scattered electron (BSE) detector for a phase contrast and secondary electron (SE) detector for morphological observations, back-scattered electron diffraction camera (EBSD) and energy dispersion X-ray analysis were used for the analysis of a grain structure and chemical composition.

Observations were performed on specimens examined by LOM for particle observations.

3.3. Transmission electron microscopy (TEM)

TEM JEOL JEM 2000FX (Fig. 3.2) was used and operated at 200kV in transmission (TEM) and scanning transmission (STEM). The samples used in TEM are thin discs with a diameter of 2.7 - 3 mm. Discs were mechanicaly polished with SiC papers to about 150 µm thickness and then electrolyticaly polished in a 30 % solution of HNO_3 in methanol to at -20 °C.

A heating holder with a Pt-PtRh thermocouple was used for in-situ heating experiments.
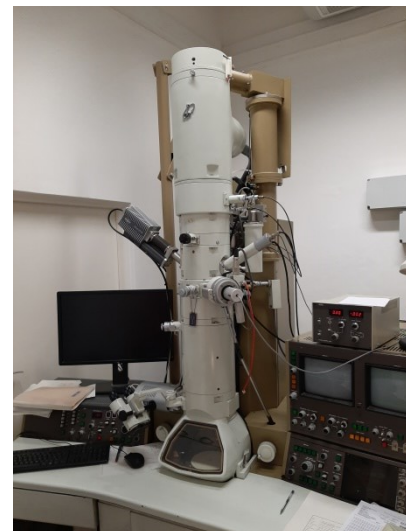
Figure 3.2: JEOL JEM 2000FX

3.4. Microhardness measurements

Microhardness measurements were performed in a Qness Q10 device (Fig. 3.3). To determine the microhardess of the sample an indentor is indented into a polished surface of the sample with a defined load. The size of the imprint is then measured with a microscope (Fig. 3.4). Depending on a shape of the indentor and a used load and the indentation size a microhardness value is calculated from an equation

$$HV = \frac{1,854F}{D^2},$$ (3.1)

which is the Vicker's microhardness value measured with the indentor in a shape of a pyramid. F is the applied load in kilograms, D^2 is the area of the indentation in square milimetres and 1,854 is a coefficient for Vicker's indentor [69].

While there are multiple models connecting measured Vicker's hardness to other material properties such as ultimate tensile strength, yield strength and more, the simplest way to estimate yield strength σ_y from measured microhardness seems to be an equation [70]

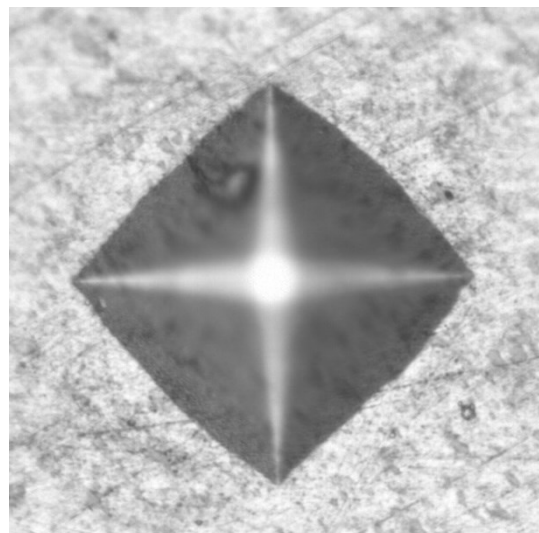$$\sigma_y = \frac{HV}{0.3}.$$ (3.2)
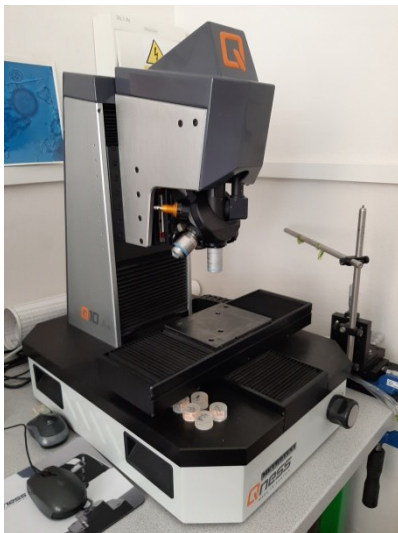
Figure 3.3: Qness Q10

Figure 3.4: Imprint under a microscope

Microhardness values can be measured at different areas of an inhomogenous sample. A suitable measurement matrix of indentations ought to be designed to ensure an accurate statistic for the measurement (Fig. 3.5) by covering the sample over at least half-width in its cross section.

The presented results are Vicker's microhardness measurements with a 100 g load – designated as HV0,1 or 10 g load should the sample be too thin for a 100 g load. The measured samples were the bulk samples used for LOM and SEM observations as no specialized polishing is required for these measurements.
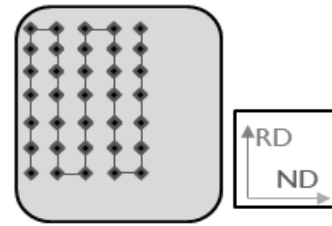

Figure 3.5: HV measurement matrix

3.5. Resistometry

To obtain resistivity the resistance of a sample is measured by a simultaneous four-point measurement method. This is a well established method based on measurements of current and voltage (Fig. 3.6). For more details see [71].

Both in-situ measurements of resistivity (both isochronal and isothermal) [72] with a defined heating step as well as remanent resistivity ratio (RRR) [73] measurements can be performed using this method.
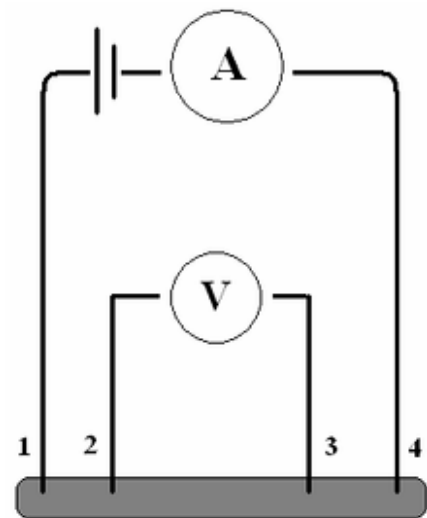
Figure 3.6. Four point method of resistivity measurement

3.6. Annealing

In-situ annealing experiments were employed during TEM observations and resistivity measurements.

In order to simulate the industrial annealing process laboratory annealing was performed in a LAC Ht40P furnace (Fig 3.7). The heating regime consisted of a 8 h heating step from room temperature (RT) up to homogenization temperature, 8 h annealing at the desired temperature and 8 h cooling step back to RT (Fig. 3.8).

Recrystalization annealing was performed in both isochronal and isothermal regimes. Isochronal annealing was performed with a 50 °C/50 min step resulting in an effective step of 1 K/min. Isothermal annealing was performed at selected temperatures with a pseudologarythmic time interval starting at 10 min and ending at up to 16 h.
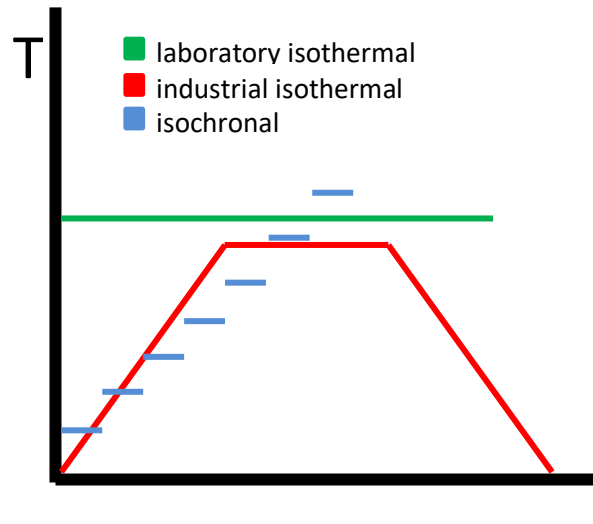

Figure 3.7: LAC Ht40P furnace

Figure 3.8: Schematics of annealing experiments

3.7. Material

The studied material is a standard AA8079 alloy containing Fe and Si as primary alloying elements provided by AL Invest Břidličná Ltd. Exact concentrations of main alloying constituents are in Table 3.1.

Alloy	Al	Fe	Si	Mn
AA8079	bal.	1.06	0.06	<0.01

Table 3.1: Composition of the AA8079 alloy in wt.%

The material was provided in a form of 8 mm thick cast strips which were further processed.

4. RESULTS

The material was studied at stages simulating the industrial process of production of thin aluminum foil. Specificaly in the cast state after TRC, after homogenization annealing at various selected temperatures, after subsequent rolling to medium gauges and finaly after a second intermediate annealing.

4.1. As-cast material

The cast billet is a silvery block of metal with a discernible texture in the direction of rolling during TRC. This texture has no other distinguishable features visible by the naked eye without further polishing and employment of microscopical methods. For further clarity, the billet has three main directions denoted in Fig. 4.1 – rolling direction (RD), transversal direction (TD) and normal direction (ND). All observations and measurements were performed in the TD of the material unless noted otherwise.
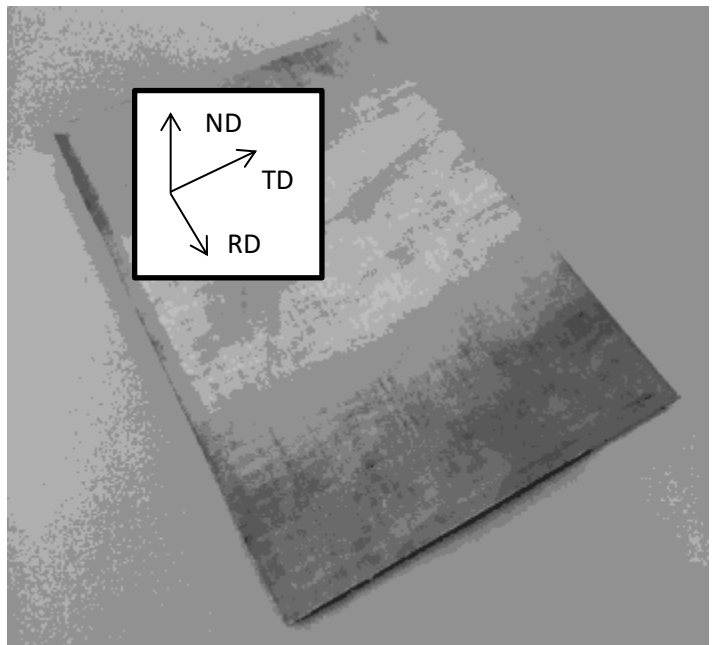

Figure 4.1: The as-cast 8079 billet

4.1.1. LOM

LOM reveals colonies of secondary phase particles present in the material (Fig. 4.2 a)). However a finer detail of these particles is not achievable through the available LOM methods. These colonies are elongated in the rolling direction, which could be seen on a detail in Fig. 4.2 b).
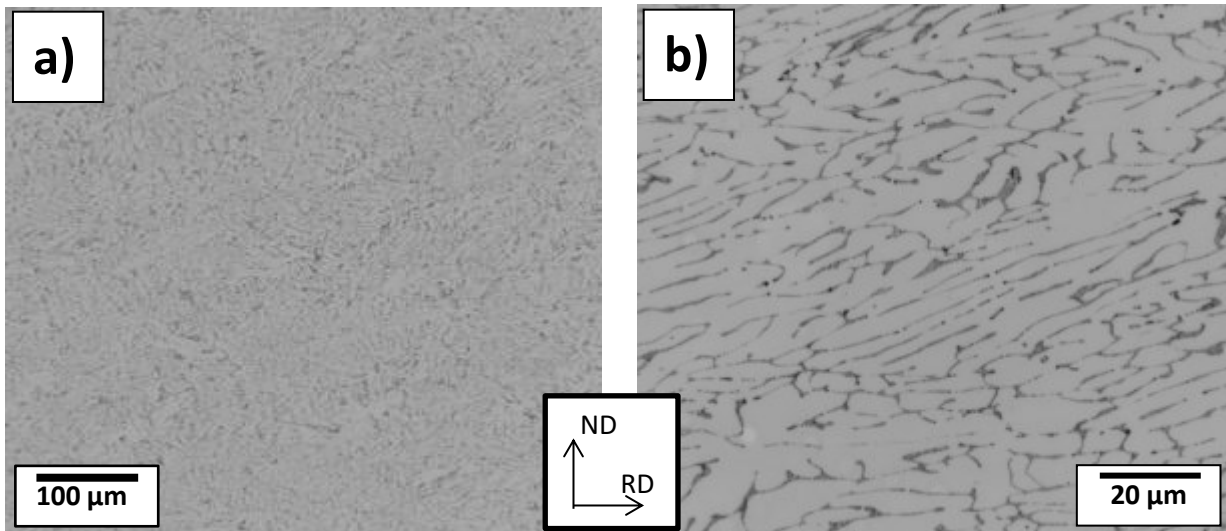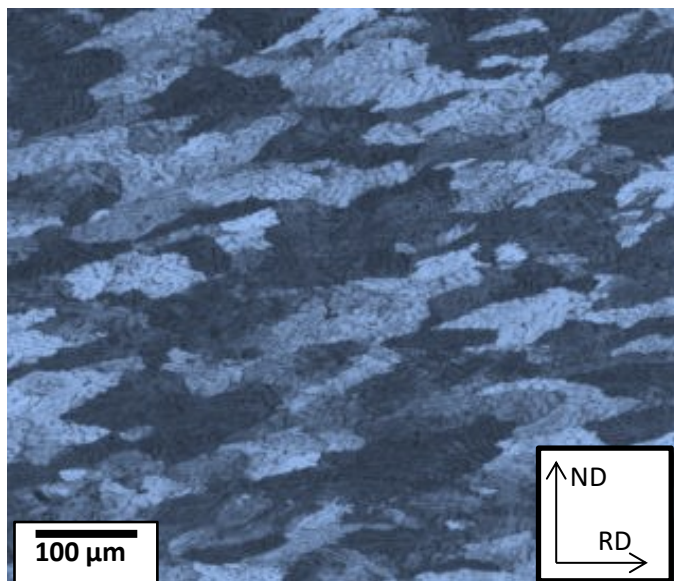
Figure 4.2: LOM images of the as-cast material: a) sample structure overview, b) eutectic structure (a detail from Fig 4.2 a))

Electrolytic anodizing in combination with polarized light allows to observe grains in LOM. The images reveal grains approximately 100 µm long and 50 µm wide (Fig. 4.3). The dimensions of individual grains are much larger than the ones of individual colonies of particles and a single grain contains multiple particle colonies.

Figure 4.3. Grain structure of the cast material

There is a variation in grain shape across the cross section of the sample (Fig. 4.4). Grains closer to the surface are longer, flat and slanted towards the center of the strip with thicker grains closer to the center almost parallel with the rolling direction (Fig. 20). This is in accordance with findings mentioned in literature [74].

The surface of the strip contains very small grains which appear in accordance with literature [63] as a result of rapid solidification during contact of the melt with a cold roll during TRC.

Figure 4.4: Grain structure of the cast strip cross section

4.1.2. SEM of the as-cast material

The observations were performed at 15 kV. The images presented are BSE ones. The detail of particle colonies (Fig. 4.5 a)) reveals a needle shape of observed particles (Fig. 22 b)). Many particles are oriented perpendicular to the sample surface and therefore their length is apparently shorter (Figure 4.5 b)).
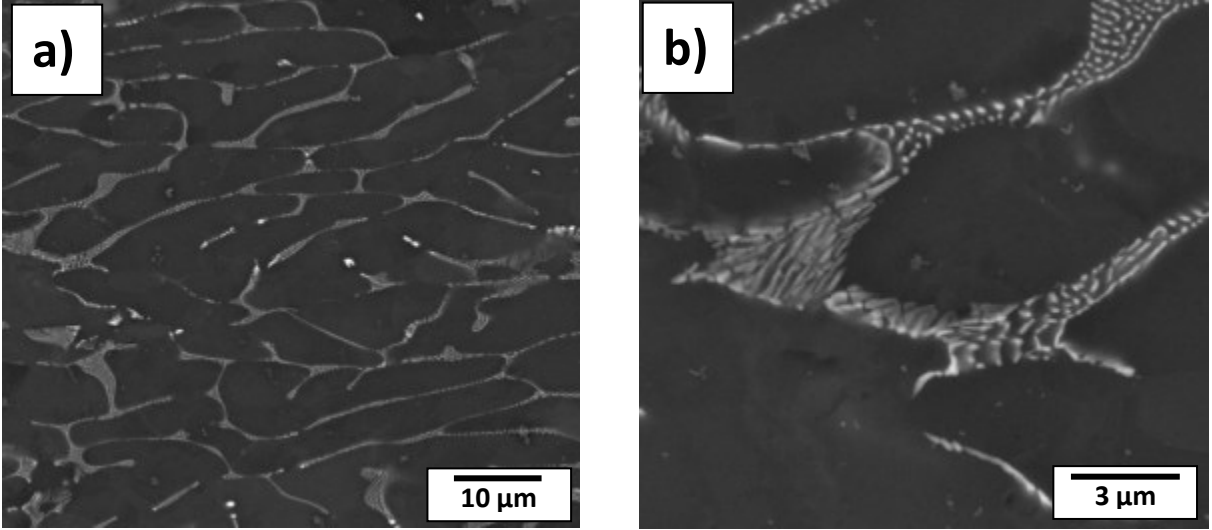

Figure 4.5: SEM of the as-cast material: a) eutectic colonies of primary phases, b) detailed view on primary phases

4.1.3. TEM

While highly detailed the particle images offer no new information (Fig. 4.6 a)), but a contrast between spaces between individual colonies can potentialy stem from a degree of

29

misorientation between individual subgrains, which would further support the theory of formation along subgrain boundaries (Fig. 4.6 b)).
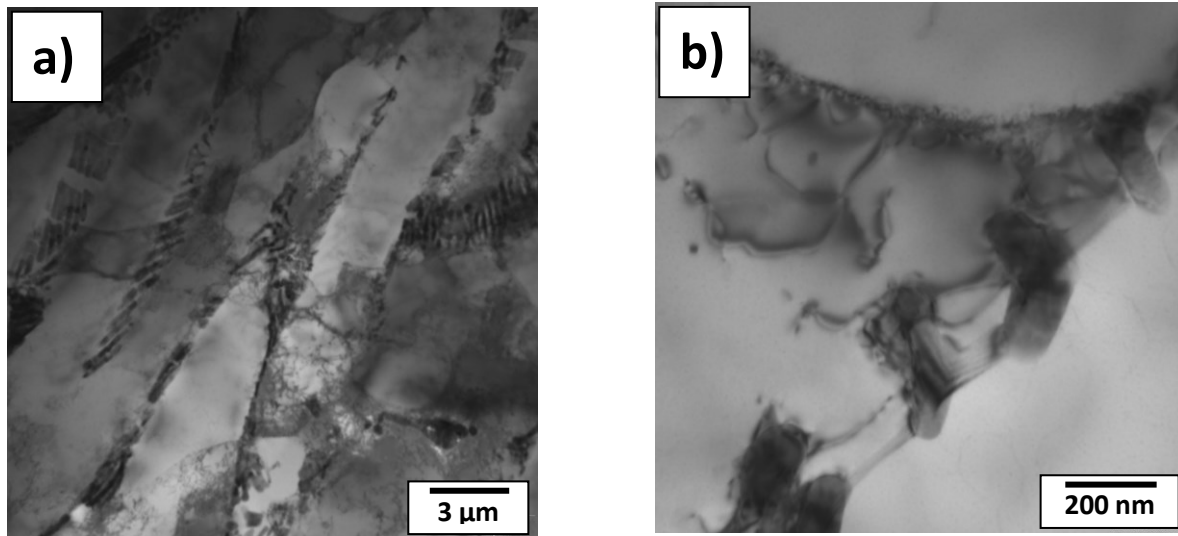

Figure 4.6: TEM of the as-cast material: a) colonies of primary phase particles situated at subgrain boundaries, b) detailed view on particles and dislocations

TEM analysis confirms a needle shape of primary phase particles. The position of their aggregates often coincides with subgrain boundaries confirming a strong dragging effect on a mobility of dislocation walls (Fig 4.6 a)). Fig 4.6 b) confirms a very low dislocation density in the as-cast material.

4.2. Isochronal annealing of the as-cast material

To get an idea of processes occuring during high temperature annealing of the material and the temperatures at which these processes occur two isochronal annealing experiments were performed – measurements of resistivity and an in-situ TEM annealing.

4.2.1. Isochronal resistivity curve

The curve was measured on a H-shaped sample about 7 cm long with a step of 20 K/20 min resulting in an effective step of 1 K/min and quenched into water at room temperature. The presented results are a curve of relative resistance change measured in a liquid nitrogen and resistivity spectrum (Fig. 4.7 a)), and RRR curve of the material (Fig. 4.7 b)) measured in liquid nitrogen and 20 °C ethanol.

The relative resistance change curve remains almost constant up to 300 °C with only a

2 % decrease of resistivity compared to room temperature. A steep decrease follows and the material reaches a a 28 % decrease in resistivity at 480 °C. The resistivity then remains constant for 40 °C and at 520 °C begins to increase again. The decrease of resistivity implies a desaturation of the supersaturated matrix and a subsequent reversion of solute saturation with the increase of resistivity. Possible changes in phase structure are not expect to heavily influence resistivity as the possible intermetallic particles present are materials with significantly lower conductivity than the Al matrix. Similarly the observed dislocation density in TEM (Fig. 4.6 b)) was low, suggesting a small change in resistivity by means of recovery.

The resistivity spectrum contains three notable peaks. Two smaller peaks correspond with a change in rate of the decrease at 400 °C and a slight deviation from the plateau at 500 °C. These could be the result of a measurement fault. While the measured values are very precise mishandling of the sample during quenching or a deviation from improper furnace settings can lead to these faulty points. The major peak at 420 °C points out the temperature at which the matrix desaturates the fastest. An additional peak is observed at 550 °C implying the highest rate of reversion.

The RRR curve appears to be the inverse of the relative resistivity change curve. RRR remains close to consant until 300 °C is reached then increases up to 480 °C and decreases again above 520 °C. RRR being the measure of purity of the material supports the presumed desaturation of the matrix.
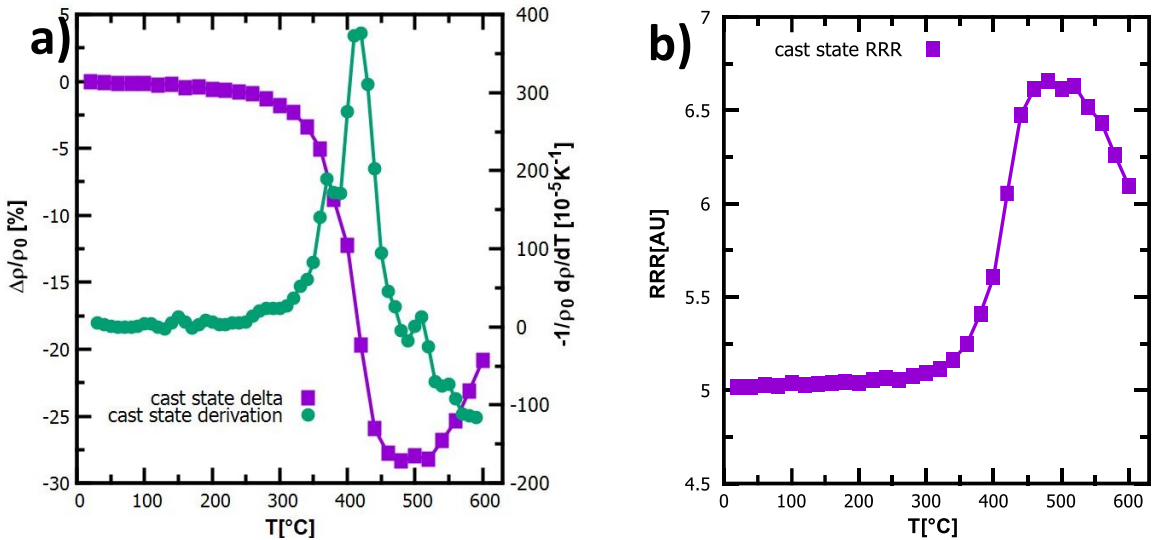

Figure 4.7: Resistivity curves of the cast material a) relative resistivity change and resistivity spectrum, b) RRR curve

31

4.2.2. In-situ TEM experiment

In-situ TEM observations give an estimate image of processes occuring in the material. However, results could not be interpreted directly as they might be affected by the nature of the TEM sample – a thin foil - with increased contribution of surface diffusion which does not occur in the bulk material.

The annealing was performed with a 25 K/5 min step starting at 300 °C up to temperatures close to 600 °C. Above this temperature the specimen was damaged. This means an effective heating rate of 5 K/min, which is higher than the rate setting of the resistivity measurement. The results should however provide an overview of processes occuring in the material.

A full recovery of the dislocation substructure appears below 400 °C. As follows from Fig. 4.8 a) nearly no dislocations could be found in the material. Because resistivity has not changed in this temperature interval it is clear that dislocation recovery does not affect resistivity of the as-cast material (Fig. 4.7 a)).

Structure of colonies and particles remains unchanged up to 400 °C temperature. An onset of particle spheroidization is observed at 475 °C with a still persisting colony structure (Fig. 4.8 b)). Nucleation of new particles outside of the original colonies is also observed at this temperature.

At 525 °C and higher temperatures a dissolution of the spheroidized particles occurs in favour of growth of a several particles both inside and outside the original colonies (Fig 4.8 c)). These newly grown particles are much coarser than both the original needle shaped and the spheroidized particles. At 575 °C only a few undisolved spherical particles still remain (Fig 4.8 d)). This is a result of Ostwald ripening of particles, because the redistribution of alloying elements into several coarse particles is more energeticaly beneficial (lower surface energy) than a presence of solutes in a larger number of fine particles.

In terms of foil stock manufacturing, the dissolution of original colonies during homogenization of the cast material should prove beneficial as a more homogenous dispersion of coarser particles should lead to a preferrable recrystalized structure after interannealing at intermediate gauges during downstream processing. As mentioned earlier, these results can not be reliably transferred to cast material and an analysis of annealed bulk material ought to be performed.
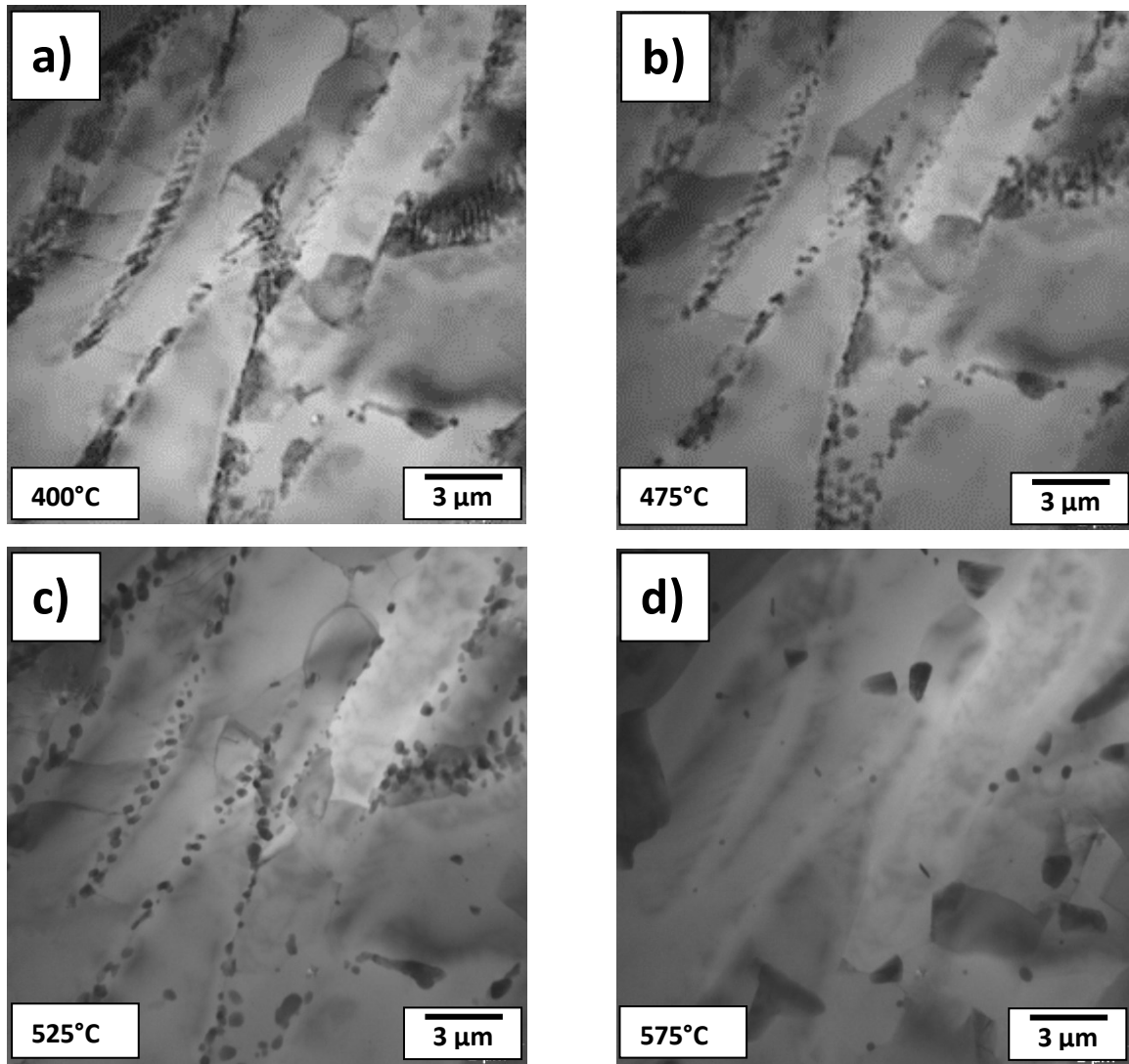
Figure 4.8: In-situ isochronal annealing experiment: a) 400 °C , b) 475 °C, c) 525 °C, d) 575 °C state

4.3. Isothermal annealing of a bulk material

As previously discussed the results of isochronal annealing experiments serve mainly as an overview and experiments performed on annealed bulk material are required for absolute certainty. The annealing was performed with the 8/8/8 h heating regime in place to simulate industrial homogenization annealing. The annealed samples were 1x1x1 cm^3 cubes for measurements other than TEM and thin 0,5 mm thick strips for TEM observations.

The selection of annealing temperatures was based on previous observations during isochronal annealing. The samples were annealed at temperatures between 400 °C and 580 °C.

4.3.1. Microhardness curve

Microhardness measurements for each of the annealed samples were performed through a series of indentations with a 100 g load. The value of microhardness measured for the cast state was (39 ± 1) HV0.1. This is a significantly higher value than measured values for pure aluminium [75] stemming from the presence of alloying elements and employment of a casting method with a cooling rate. However it is fairly standard for TRC 8079 as similar values have been measured by other researchers [73].

There is a slight drop from the original value (Fig. 4.9) after homogenization at the lowest selected temperature. The change in microhardness is fairly low however and is likely related to recovery of the material. Above 400 °C the microhardness continues to decrease at a higher rate reading a minimum at 500 °C, after which it remains constant within the statistic scatter of each mesurement.

The major decrease of microhardness could be related to some of the processes observed in TEM. Changes in a particle distribution, subgrain structure and matrix saturation all could influence yield strength of the material which in turn influences the measured hardness.

Figure 4.9: Microhardness development of the homogenized material

4.3.2. Evolution of grain size during homogenization

The grain size in the centre of the strip does not change throughout the homogenization process even when annealed at 580 °C (Fig. 4.10 c)) because the driving force in a relatively slowly solidified centre is not high enough to cause a motion of grain boundaries. However there is a significant growth of the surface grains proceeding further towards the centre of the strip. At 580 °C a singular surface grain grows up to several hundreds of μm into the strip. This process starts at 500 °C (Fig. 4.10 a)) and the grain size increses proportionaly with increasing temperature (Fig. 4.10 b)).
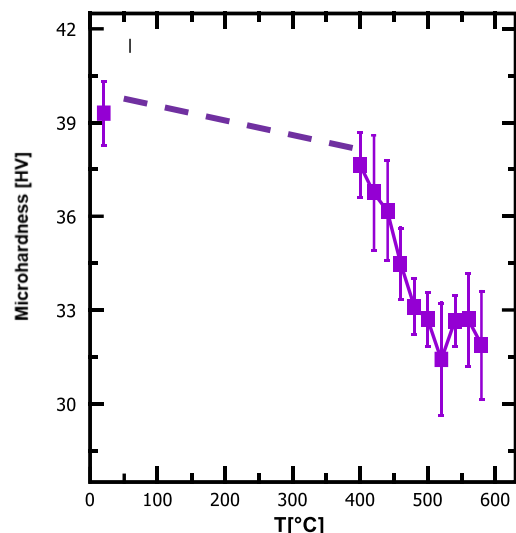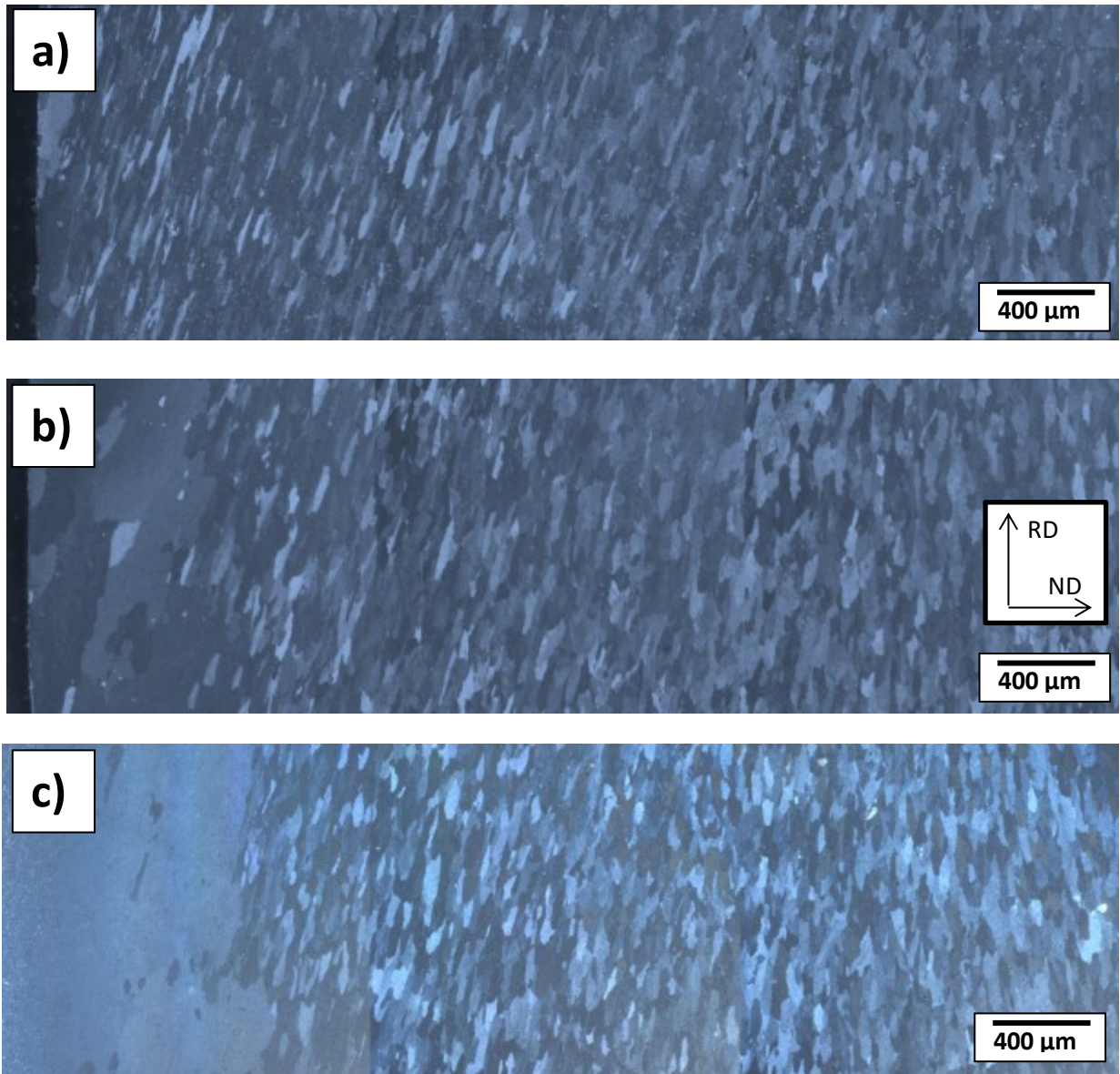
Figure 4.10: LOM image a TRC strip homogenized at: a) 500°C, b) 520 °C, c) 580 °C

The grain growth along the surface is caused by a rapid solidification of the surface layer and associated formation of very fine grains at the surface. The surface area then serves as center for a nucleation of recrystallized grains which can further grow. Majority of grains in the strip remain stable during homogenization.

4.3.3. Material homogenized at 420 °C

A LOM image indicates that original distribution of particles in colonies remains preserved (Fig. 4.11). The larger black spots not observed in such a high frequency in the cast material might indicate the beginning of transformation of primary phase particles.

This is partialy confirmed by SEM observations (Fig. 4.12), because a local fusion of several particles could be recognized (Fig. 4.12 b)).
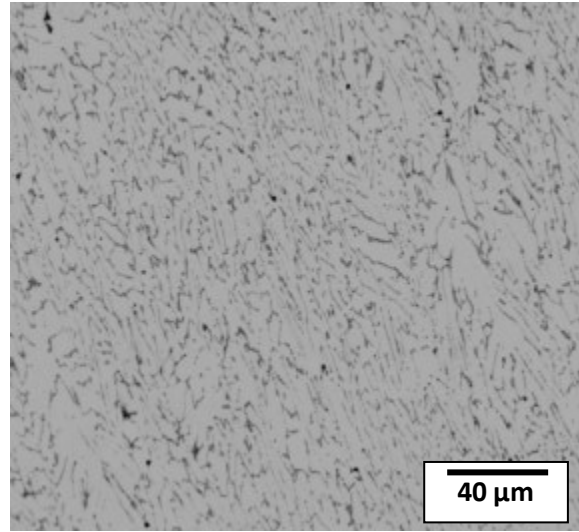

Figure 4.11: LOM of the material homogenized at 420 °C

However, no significant difference was observed in TEM (Fig. 4.13). A slightly higher density of dislocations than in the in-situ sample can be attributed to mechanical polishing and handling of the sample, which is not present at the corresponding temperature during in-situ annealing. The distribution of particles remains unaffected, which might be an artifact of a smaller field of view in TEM (Fig. 4.13 b)).
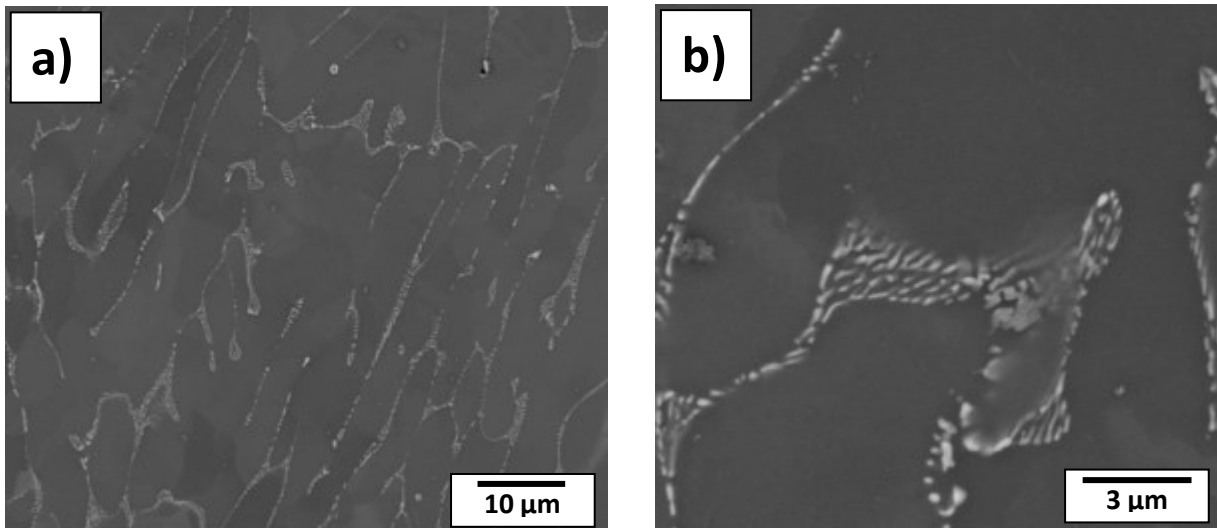
Figure 4.12: SEM of the material homogenized at 420 °C: a) structure of eutectic colonies, b) detailed view on particles
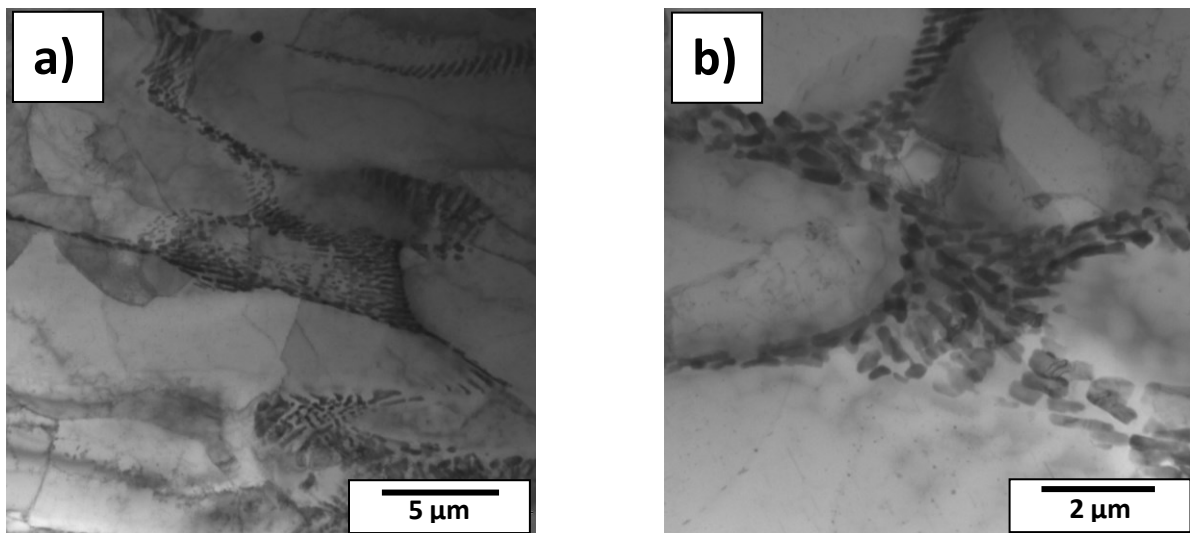

Figure 4.13: TEM of the material homogenized at 420 °C: a) structure of eutectic colonies, b) detail of particles

Microhardness tests as well as results of imaging methods do not report strong changes in the structure of original particles or in their distribution.

Disputable is a shape of resistivity curves. The material exhibits the most rapid drop in resistivity which is especialy noticable in the derivative curve having a global maximum at approximately 420 °C. This is however understood if we work with the assumption that the drop is caused by a change in a matrix saturation which could not be noticed by imaging techniques. Microhardness measurements could respond to solid solution strengthening, but its magnitued remains to be evaluated.

4.3.4. Material homogenized at 480 °C

During the in-situ experiment the particles have started to spheroidize at about 475°C. The closest temperature in the model homogenization regime is 480 °C. At this temperature the resistivity of the material has already a stable value with no extrema in the derivative curve and microhardness of the homogenized sample is already at a minimum value.

LOM shows (Fig. 4.14) that the colony structure continues to withstand the increased temperatures however a change in the shape of individual particles and their aggregates is more noticeable than in samples annealed at 420 °C (Fig. 4.11).
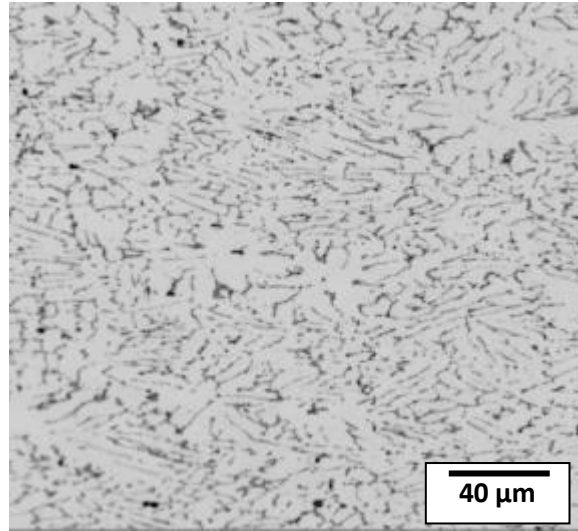

Figure 4.14: LOM of the material: homogenized at 480 °C

Details of the particles revealed by SEM confirms a beginning of a spheroidization of particles (Fig. 4.15 a)), and a high number of new particles throughout the sample outside the original particle colonies (Fig. 4.15 b)).
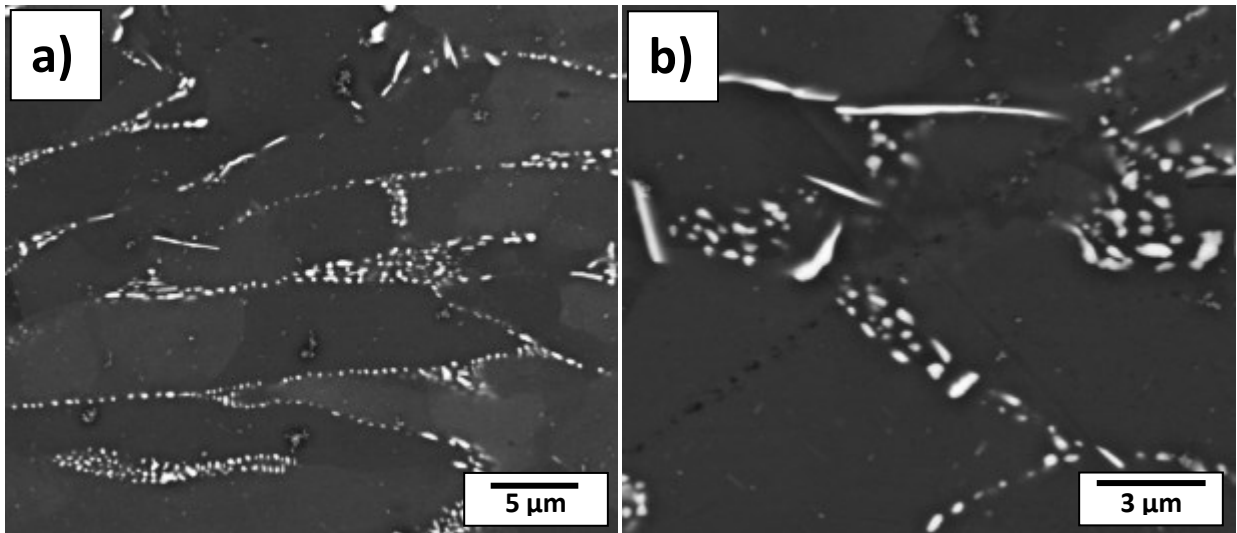
Figure 4.15: SEM of the material homogenized at 480 °C: a) eutectic structure b) particle detail

The difference between the number of new particles could be one of the differences between in-situ observations and ongoing bulk annealing observations as it is confirmed by TEM observations (Fig. 4.16).
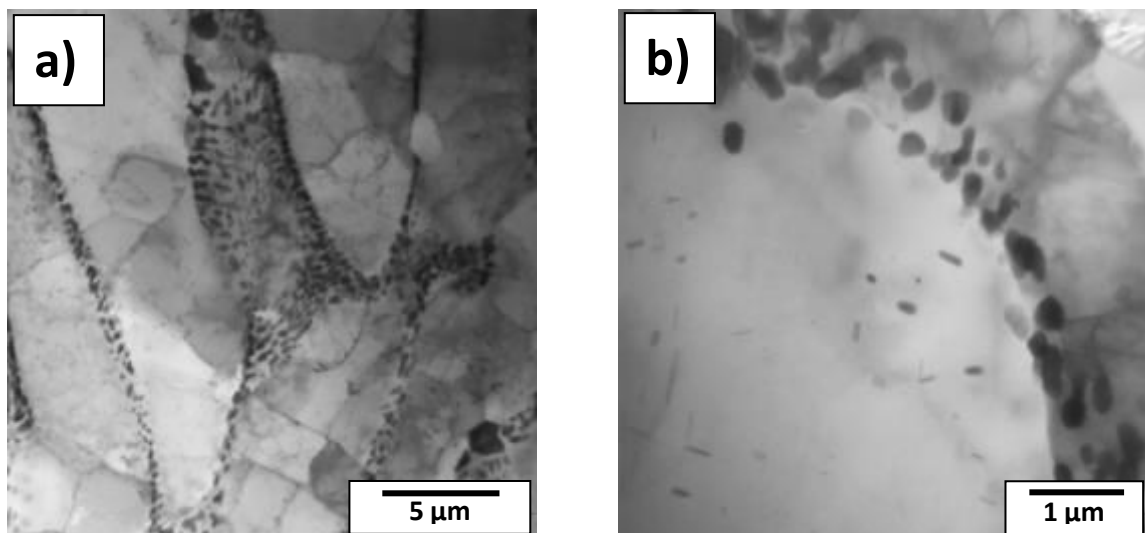

Figure 4.16: TEM of the material homogenized at 480 °C: a) distribution of particles in eutectic colonies, b) detail with newly found particles

One more thing to take into consideration is that the spheroidization of particles is not a process that occurs in all particles at once. It is also difficult to pinpoint the exact breaking point for the process in post-mortem samples because some particles might simply be oriented in a way in which their cross-section is spherical.

4.3.5. Material homogenized at 520 °C

The microstructure is similar to the one observed in in-situ annealed samples, with the bulk of the particles being already spheroidized, even in LOM images (Fig. 4.17) the change in a particle shape and numerous coarse particles could be recognized. The original shape of colonies is still evident, however an increasing number of separate particles could be distinguished even in the LOM images (Fig. 4.17 b)) continuing their growth.
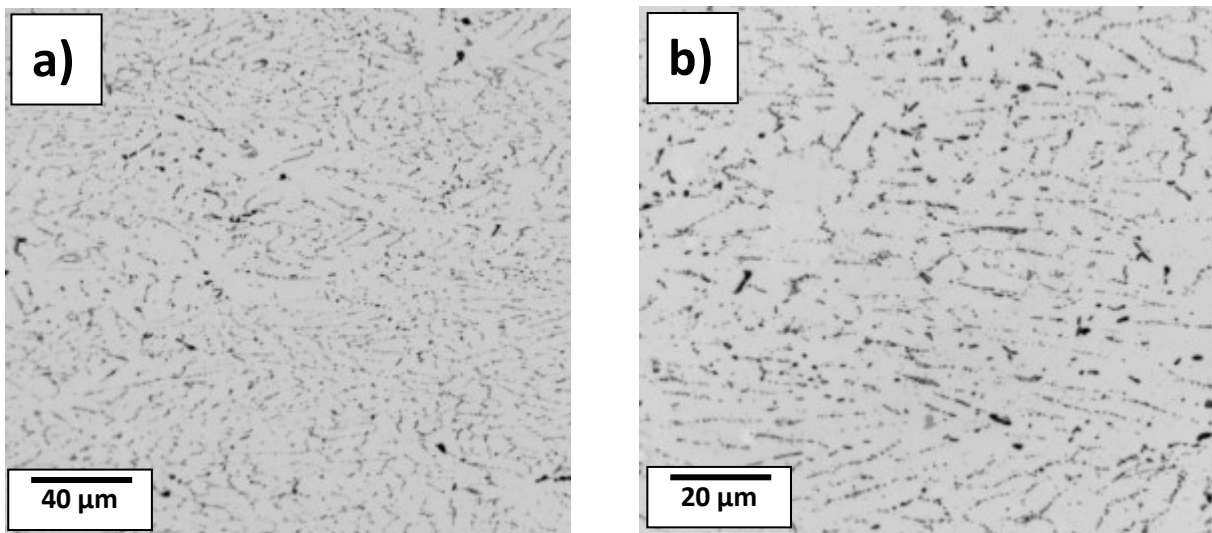

Figure 4.17: LOM of the material homogenized at 520 °C: a) overview, b) closer detail

The ongoing phase transformations are even better evidenced by SEM (Fig. 4.18).
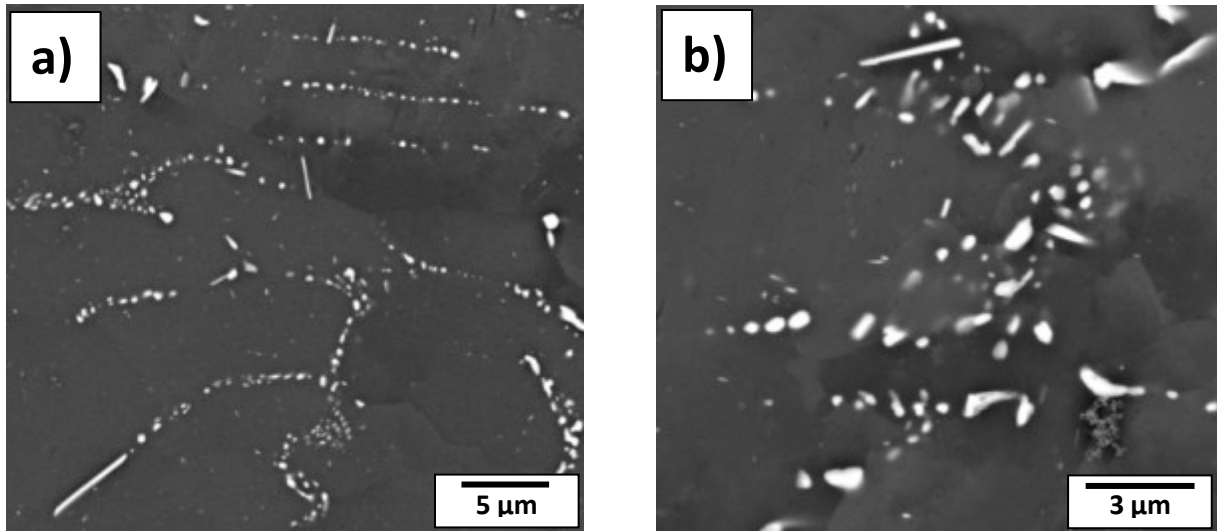
Figure 4.18: Material homogenized at 520 °C: a) overview, b) detail of transformed particles

Certain amount of particles from original colonies transformed into elongated ones, however the majority of particles in colonies has still a spherical shape. This is apparent from TEM imaging (Fig. 4.19).

Although the material homogenized at 520 °C contains a large number of small intermetallic particles scattered throughout the grains the measured microhardness of the material remains unaffected by their presence. This fact indicates a minor role of a dispersion strengthening in the material.
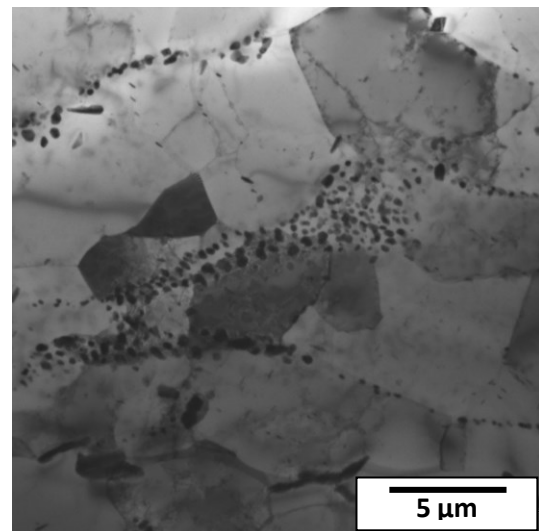

Figure 4.19: TEM image of the material homogenized at 520 °C

4.3.6. Material homogenized at 560 °C

While the colony structure still remains at least remotely coherent even at 540 °C (Fig. 4.20) at 560 °C the material is fully broken and contains a mixture of finer and coarser particles (Fig. 4.21). The coarser particles have formed primarily through growth of the original particles from eutectic colonies after their transformation while the fine particles are either remnants of the spheroiditzed untransformed particles or newly formed ones that havent grown in size. The particles are rather homogenously spread through the material.
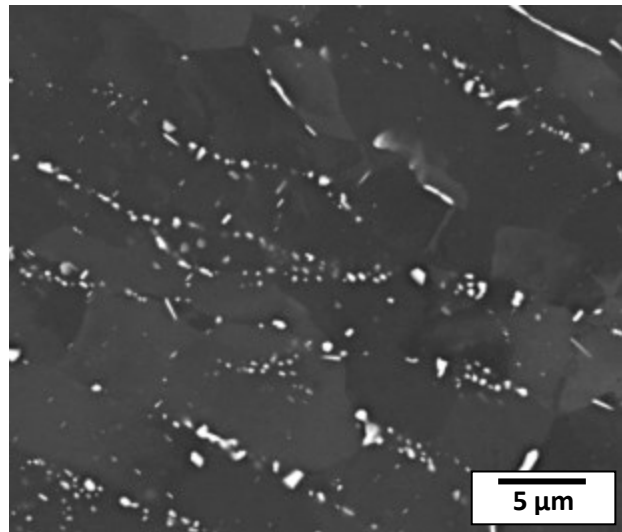

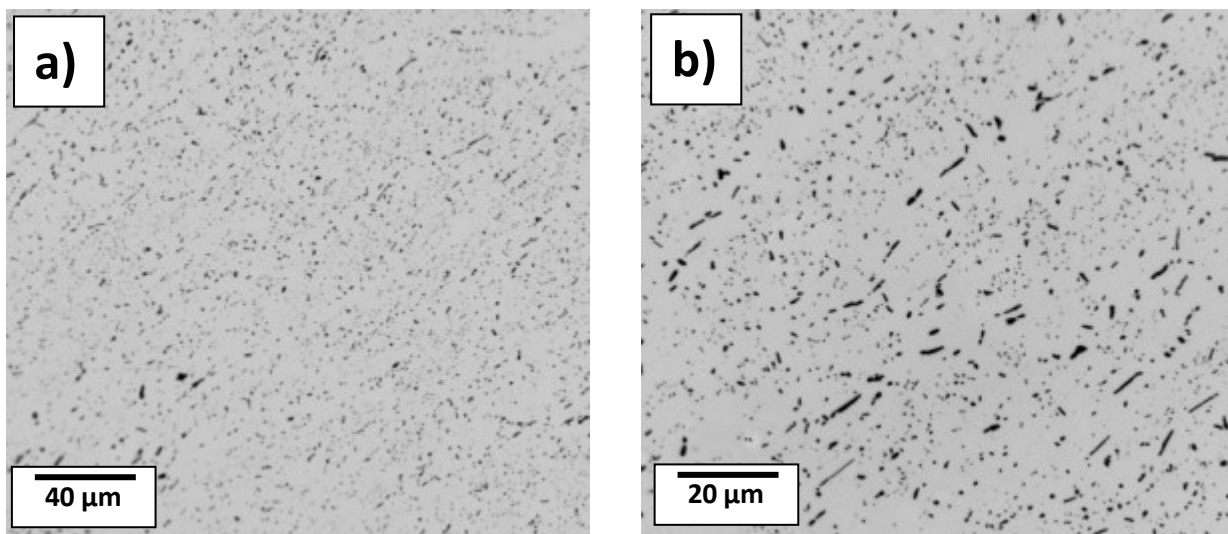Figure 4.20: Residues of colony structures of material homogenized at 540 °C

Figure 4.21: LOM of the 560 °C homogenized material: a) structural overview, b) detail of coarser particles

The SEM image shows the mixture of finer and coarser particles more clearly (Fig. 4.22) with an interesting aspect of the fine particles being their orientation either in the original RD or in TD. Some of the particles appear ball shaped still however it is possible it is the same type of particle as the needle shaped ones just oriented perpendicular to the observation plane in the ND. TEM imaging only reveals slightly more detail considering the individual particles and

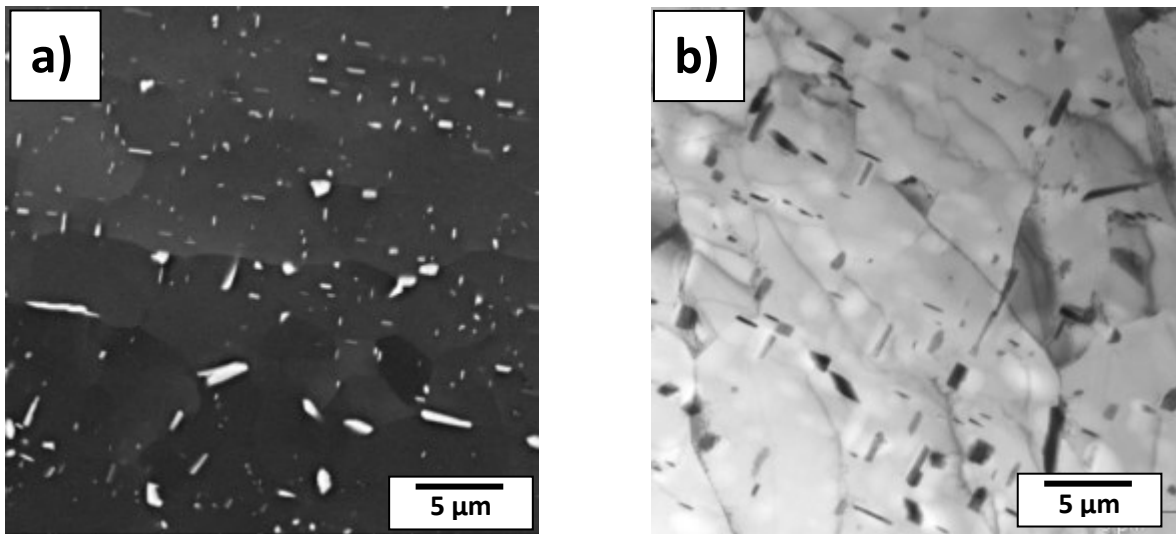their position in relation to grain and subgrain boundaries (Fig. 4.22 b)).

Figure 4.22: Particle detail of the 560 °C homogenized material a) SEM, b) TEM

No structural differences could be recognized in samples annealed at 580 °C (Fig. 4.23).

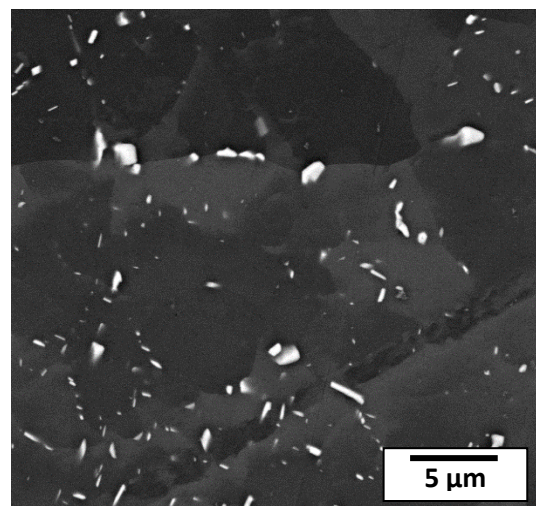Figure 4.23: SEM image of the material homogenized at 580 °C

4.4. Isochronal annealing of the homogenized and rolled material

Homogenized materials were further rolled to gauges of 600 μm and 60 μm. These two sets of materials were prepared for the analysis of intermediate annealing at medium gauges.

Because the number of variations was too high only several representative ones were studied in detail.

4.4.1. Resistometry of the rolled homogenized material

Similarly to the cast material H-shaped samples were cut from the rolled strips and a resistivity evolution was measured.

The RRR graphs reveal a higher RRR value in both rolled materials. Aditionaly the initial RRR values of the thinner material (Fig. 4.24 b)) are lower as the defect originated component of the resistivity are probably more significant than the same values in the thicker material (Fig. 4.24 a)).

The measured values comprise an influence of deformation structure and substructure and phase and solute atoms dirstributions imposed by previous homogenization annealing.
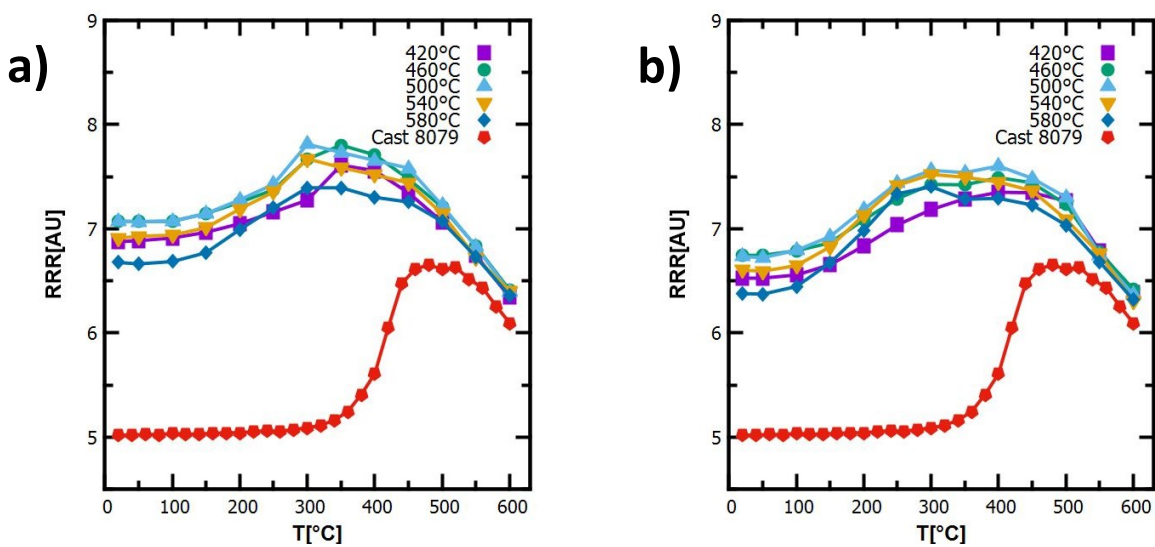

Figure 4.24: Comparison of RRR curves of as-cast state and homogenized materials: a) 600 μm thick, b) 60 μm thick

The increase of RRR of rolled materials starts at much lower temperatures. For all the materials the increase starts almost immediately above room temperatures most probably as a result of recovery. Following peaks and decreases probably indicate a continuation of solutes redistribution in deformed materials similar to processes observed in the as-cast materials, however enhanced by an increased number of sites for a heterogenous nucleation and growth.

Resistivity change curves (Fig. 4.25, 4.26 a)) show a higher change in thinner materials probably as a result of higher degree of recovery. The processes contributing to resistivity evolution seem to be significantly retarded in materials with low homogenization temperatures as their resistivity minima as well as corresponding peaks in the resistivity spectra (Fig. 4.25, 4.26 b)) are shifted towards higher annealing temperatures. Similarly this

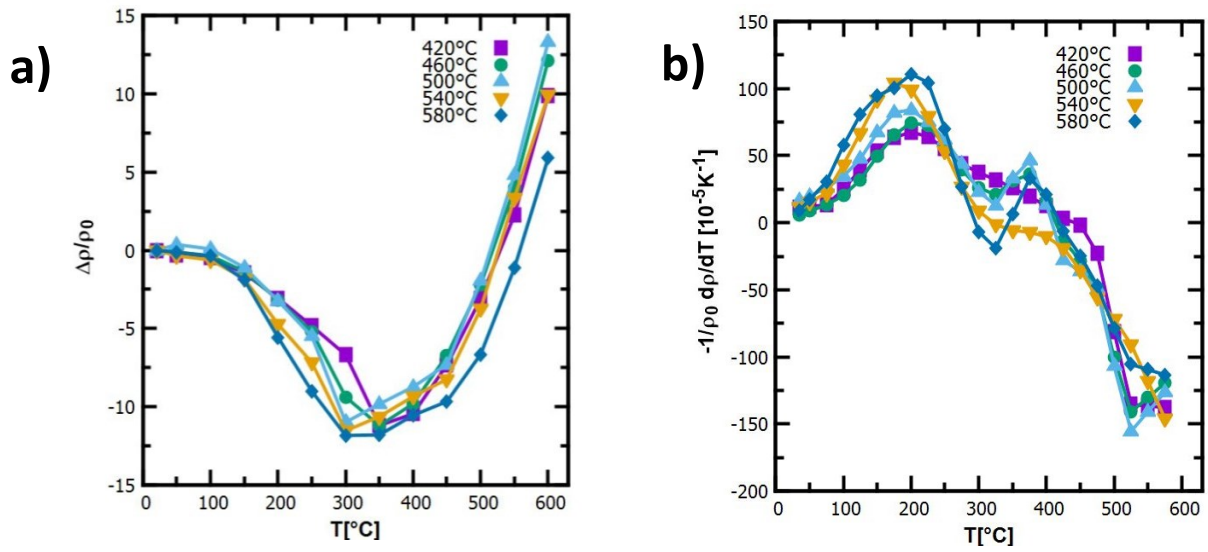retarding effect seems to be higher in thicker materials.

Figure 4.25: Resistivity curves of the 600 μm thick material a) relative resistivity change, b) corresponding resistivity spectra
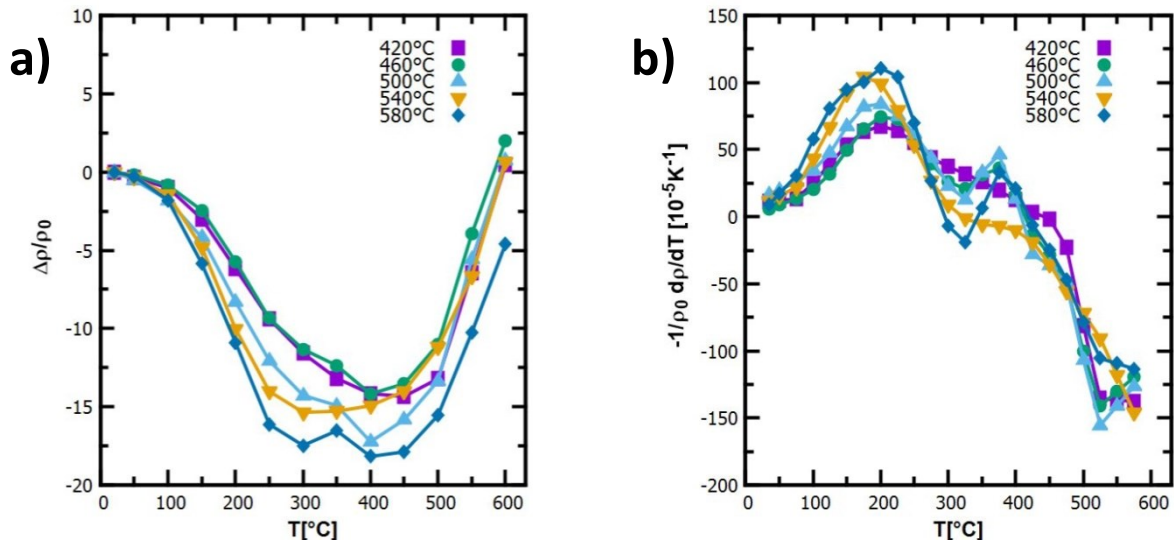

Figure 4.26: Resistometry curves of the 60 μm thick material a) relative resistivity change, b) corresponding resistivity spectra

4.4.2. Microhardness of the homogenized rolled material

While the thicker material was tested by the Vickers indentor with a load of 100 g the process had to be slightly modified for the thinner material. To compensate a limited thickness a 10 g load was chosen instead. This however presents another issue – the measured hardness values for different loads are intrinsicaly different and generally are higher for lower loads. This presents a disconnect between absolute values of the thinner and thicker material. Therefore absolute values could not be compared between the two groups of materials.

Microhardness curves of the thicker material (Fig. 4.27 a)) is higher than the one observed in the as-cast material with small variations between individual homogenization temperatures. This is likely a result of different structures behaving differently during rolling. Just like the as-cast material the hardness decreases slightly at the beginning, then a drop of hardness occurs followed by relatively constant microhardness values. However in the rolled materials the onset of softening occurs at lower temperatures between 150 °C and 250 °C. Materials with higher homogenization temperature ones soften at lower temperatures. All the materials reach their lowest hardness at 300 °C with the exception of the one homogenized at 500 °C. The softening of the material homogenized at 580 °C is the most pronounced the most reaching even lower hardness values than the as-cast material while materials homogenized at lower temperatures experience a drop to essentialy the same value as the cast one.

The evolution is less systematic for thinner materials (Fig. 4.57 a)). Partialy it is a result of larger scatter of measured values. Not only are the indentations much smaller resulting in a higher intrinsic measurement error of the length of the diagonals, the sample is also more prone to external factors such as slight tremors of the room. While this was irrelevant for the thicker material many of the indentations in the thinner material were shifted towards the surface of the sample as opposed to their position in the preprogrammed matrix and yielded unusable results lowering thus the overall statistic sample size.

The material displays a variation in initial hardness values once again with the onset of softening at 150 °C in materials homogenized at 580 °C and 540 °C. The remaining samples begin to soften at 200 °C. This is where, after a limited local increase of microhardness, the evolution starts to differ. Only the 580 °C homogenized one reaches its final, lowest hardness at 350 °C, the 540 °C and 500 °C homogenized samples reach this point at 400 °C and the two samples with the lowest homogenization temperature do not reach the minimum until 550 °C at which point all the samples display the same microhardness value within the

experimental error.

The derivative curves (Fig. 4.27 and 4.28 b)) exhibit a presence of a large peak lying between 250 °C and 300 °C in thicker materials correlating with the decrease of microhardness for all but the material homogenized at 500 °C which shows two peaks indicating a potential two stage process with a more pronounced fraction of recovery delaying the final recrystalization.

Similarly, thinner materials exhibit the presence of a series of peaks shifted to higher temperatures with decreasing homogenization temperatures indicating clearly a shift of recrystalization temperatures in the thinner rolled materials.
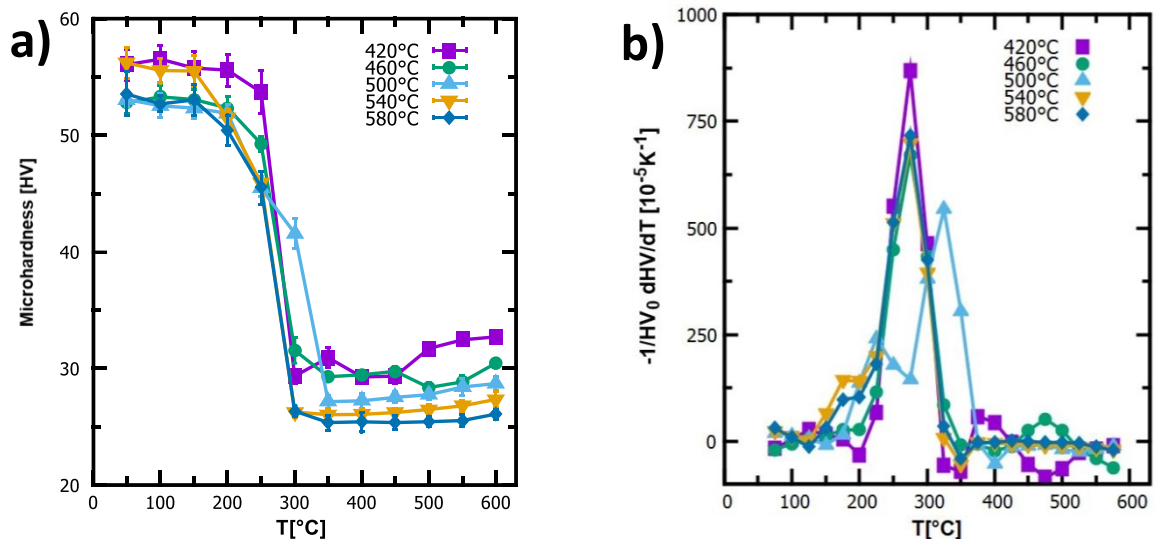

Figure 4.27: Microhardness curves of the 600µm thick homogenized materials: a) the microhardness, b) normalized temperature derivative
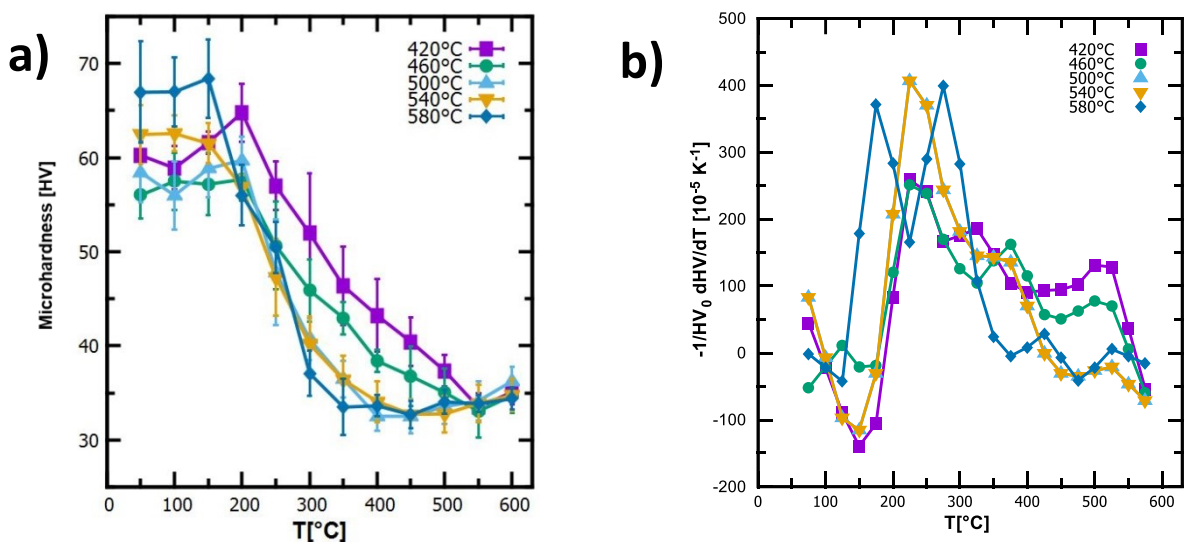

Figure 4.28: Microhardness curves of the 60µm thick homogenized materials during

isochronal annealing a) the microhardness, b) normalized temperature derivative

4.4.3. LOM for microhardness measurements

The samples were subsequently repolished to remove the indentations and both polsihings with HF for intermetallic particles observation in the samples and a Barker etch for the grain structure visualization were performed.

Analysis of microhardness curves (Fig. 4.27, 4.28) shows that the most significant changes of grain structure could be expected at about 250 °C and and higher temperatures for all the thicker materials. The onset of softening occurs at lower temperatures for thinner materials however the decrease of microhardness observed is not so fast implying the recrystalization process might be spread over a longer temperature interval.

The homogenized material rolled to 600 µm

The observed grain structure for the material annealed at 50 °C is typical for rolled materials showing flat grains, significantly elongated in the rolling direction regardless of the selected homogenization temperature (Fig. 4.29).

There are however exceptions. The 580 °C material and to an extent the 540 °C homogenized one as well have much thicker elongated grains near the surface of the strip. This is a result of the grain growth at the surface of the cast strip during homogenization discussed earlier in the text (Fig. 4.10). This shows that the structure imposed by the homogenization could not be fully broken by the rolling process, at the very least not when rolled to a 600 µm gauge.

The elongated rolling structure of the grains remains stable up to 250 °C (Fig. 4.30) which is just before the largest microhardness decrease was observed. However the Barker etch does not fully reveal subgrain structure which can affect the measured microhardness.

Corresponding to the drop of microhardness the grain structure also abruptly changes upon annealing to 300 °C (Fig. 4.31) and significant differences of the grain structure between individual materials could be found.
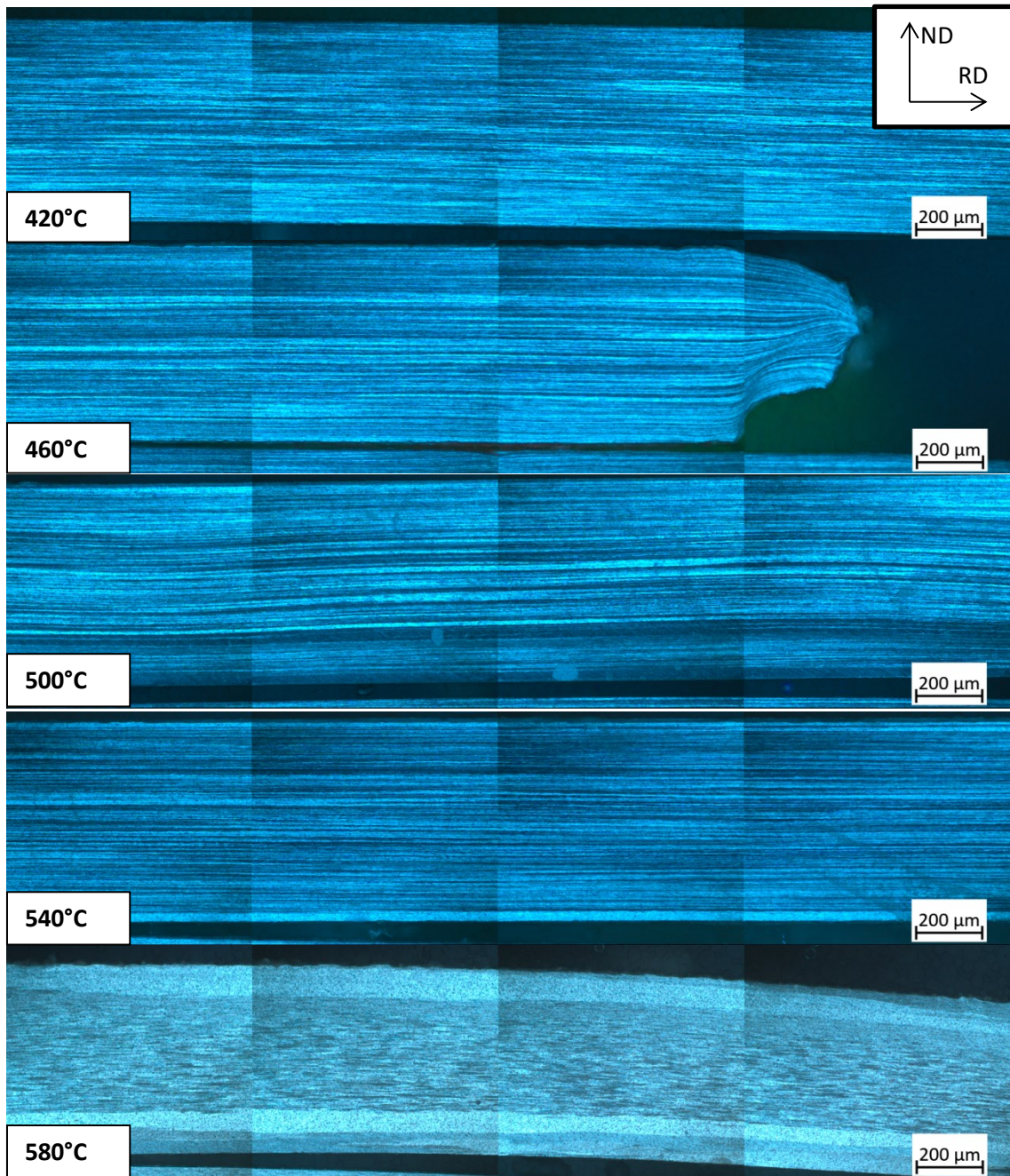
Figure 4.29: Grain structure of the 600 µm material after annealing to 50 °C

The 580 °C homogenized material now contains a fairly homogenous dispersion of fine equiaxed grains in the centre of the strip however the surface layer remains lined with coarse grains that have so far undergone only a partial recrystalization. The 540 °C homogenized material contains a dispersion of fine equiaxed grains throughout the strip however there are slightly coarser elongated grains inbetween the fine ones. The 420 °C and

500 °C homogenized materials so far contain a large amount of recrystallized small grains however the majority of the volume remains mostly unrecrystallized. While this is in line with the two phase microhardness drops of the 500 °C homogenized material it is unclear how this correlates with the microhardness drop of the 420 °C homogenized material. The 460 °C homogenized material is mostly recrystallized with grains elongated and much coarser than the grains observed in some of the materials homogenized at higher temperatures.
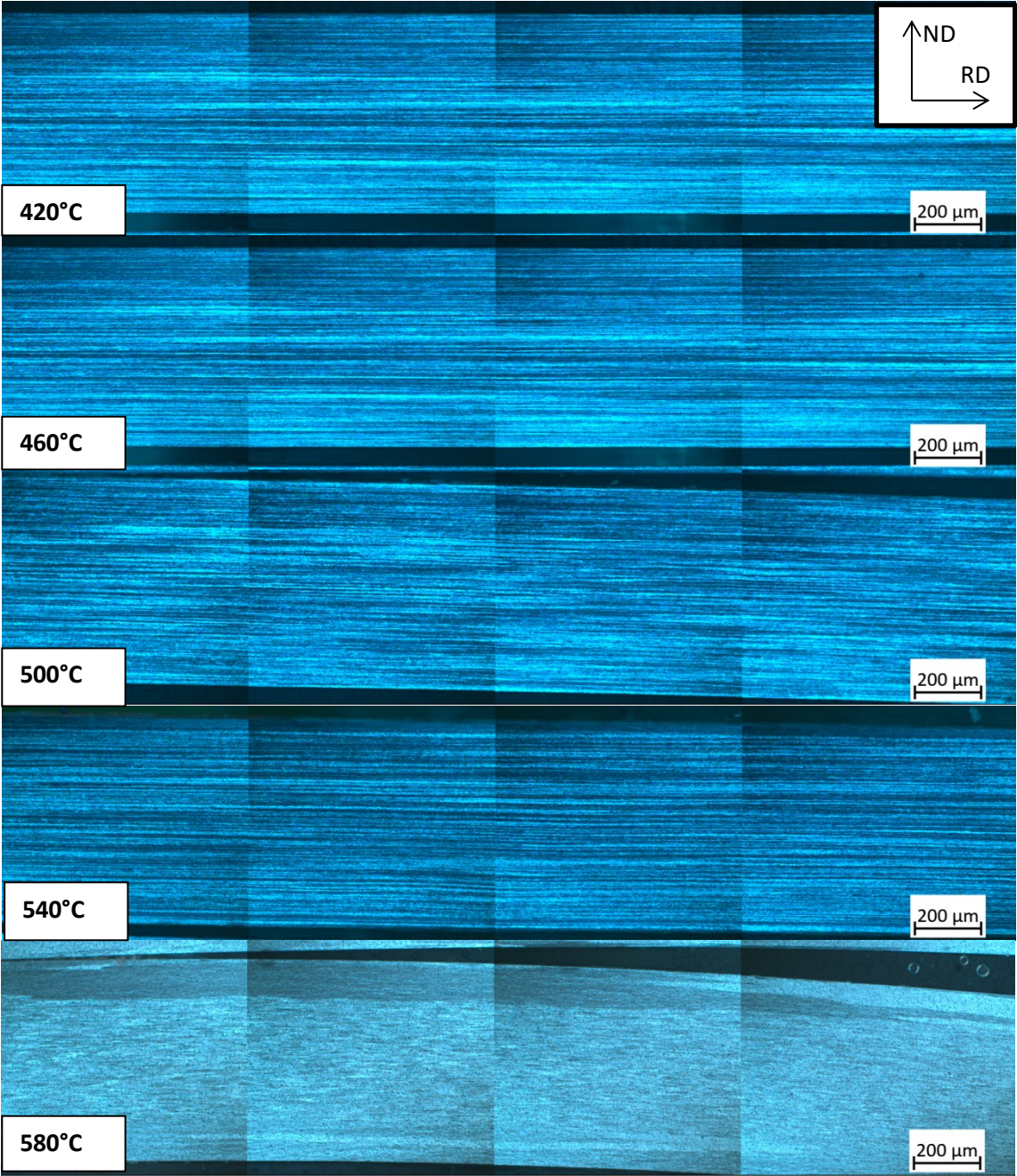
Figure 4.30: Grain structure of the 600 μm material after annealing to 250 °C

The nature of the grain structure of these strips is in line with the expected predictions that could be made based on the observed homogenized structures. The higher homogenized materials do contain coarser particles than the lower homogenized ones and as such promote a finer recrystallized structure after rolling through PSN.
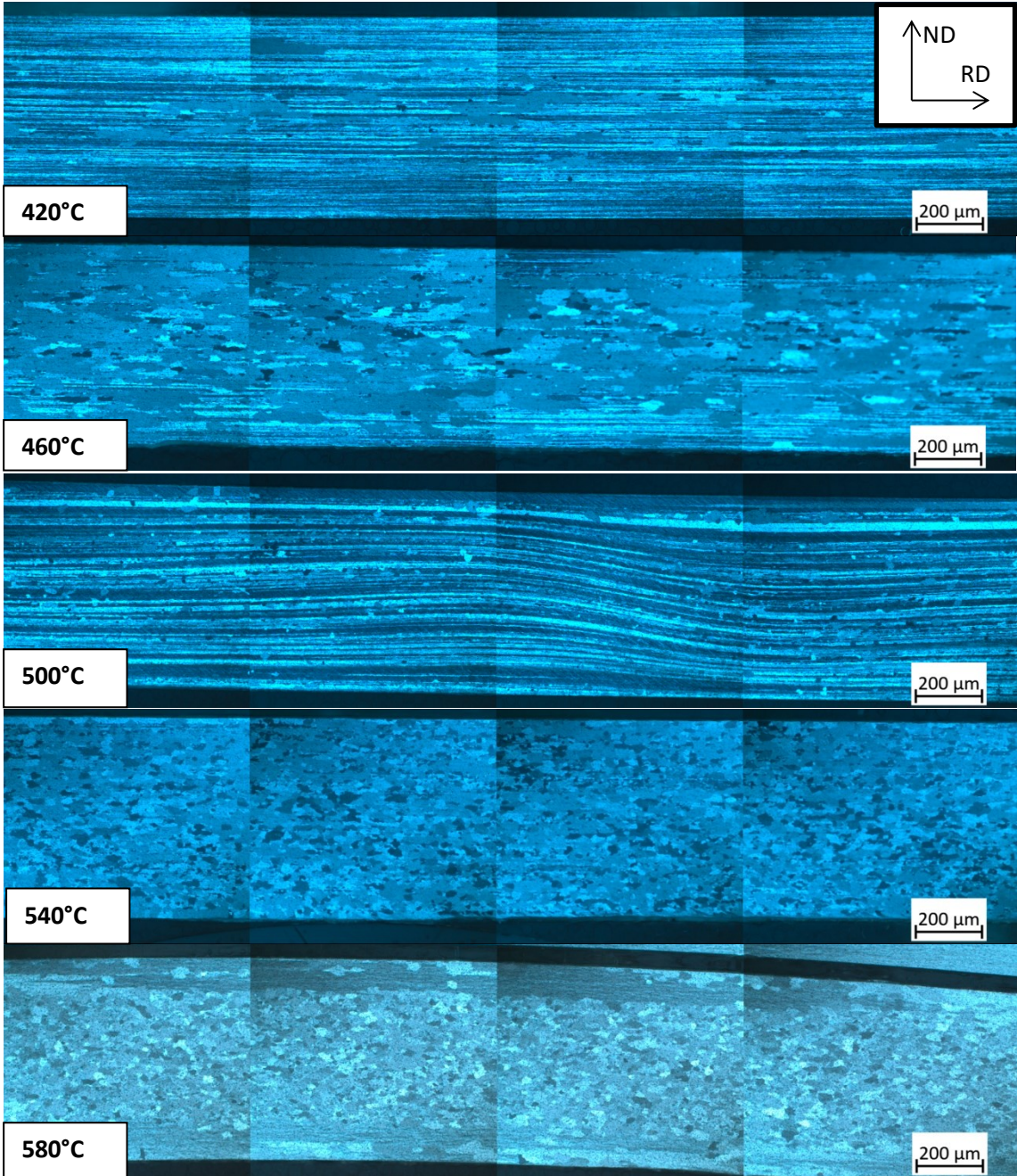
Figure 4.31: Grain structure of the 600 μm material after annealing to 300 °C

The strips have all fully recrystallized at 350 °C (Fig. 4.32) including strips

homogenized at 420 °C and 500 °C. The structural features of the remaining materials are generaly the same as in samples annealed up to 300 °C.

The 500 °C homogenized material finaly recrystallizes showing a dispersion of finer grains in the centre of the strip and coarser grains on the surface. This trend continues towards lower homogenization temperatures with fewer fine grains in the 460 °C homogenized materials centre and coarser grains overall. The 420 °C homogenized material consists of coarse grains only.
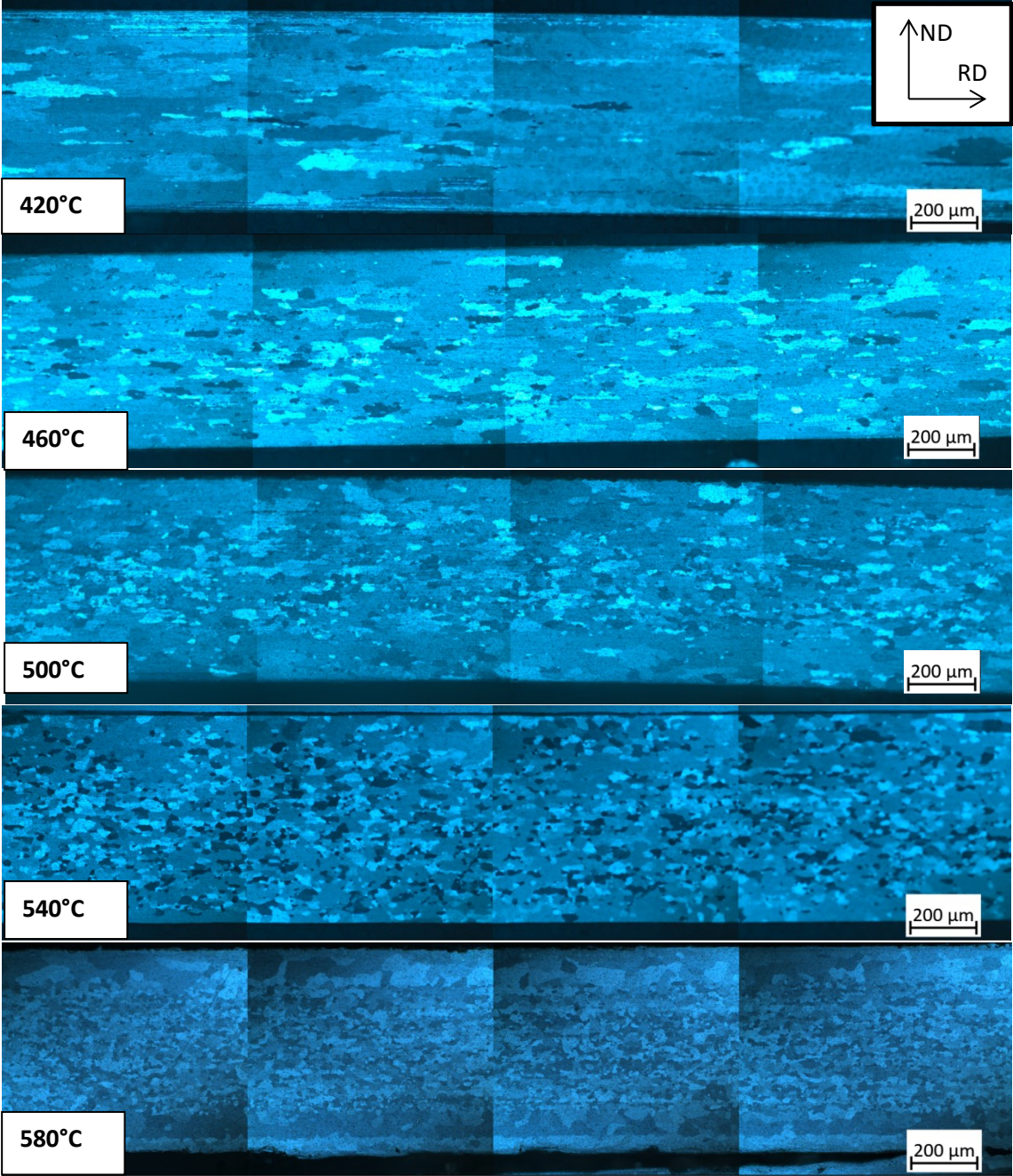
Figure 4.32: Grain structure of the 600 µm material after annealing to 350 °C

The grain structure then remains stable during annealing up until the point where grain growth begins. Grain growth temperature is different for different homogenization temperatures however it is not observed below 500 °C and is apparent at 550 °C (Fig. 4.33). No change could be found in the 420 °C homogenized material as that one already contains only coarse grains. The fraction of large grains increases in the 460 °C homogenized strip. The fraction of fine grains is still dominant in the 500 °C and 540 °C homogenized materials. However, the coarse surface layer of the 580 °C homogenized material grows further inward and partialy grows over the previously fine grains in the centre of the strip.
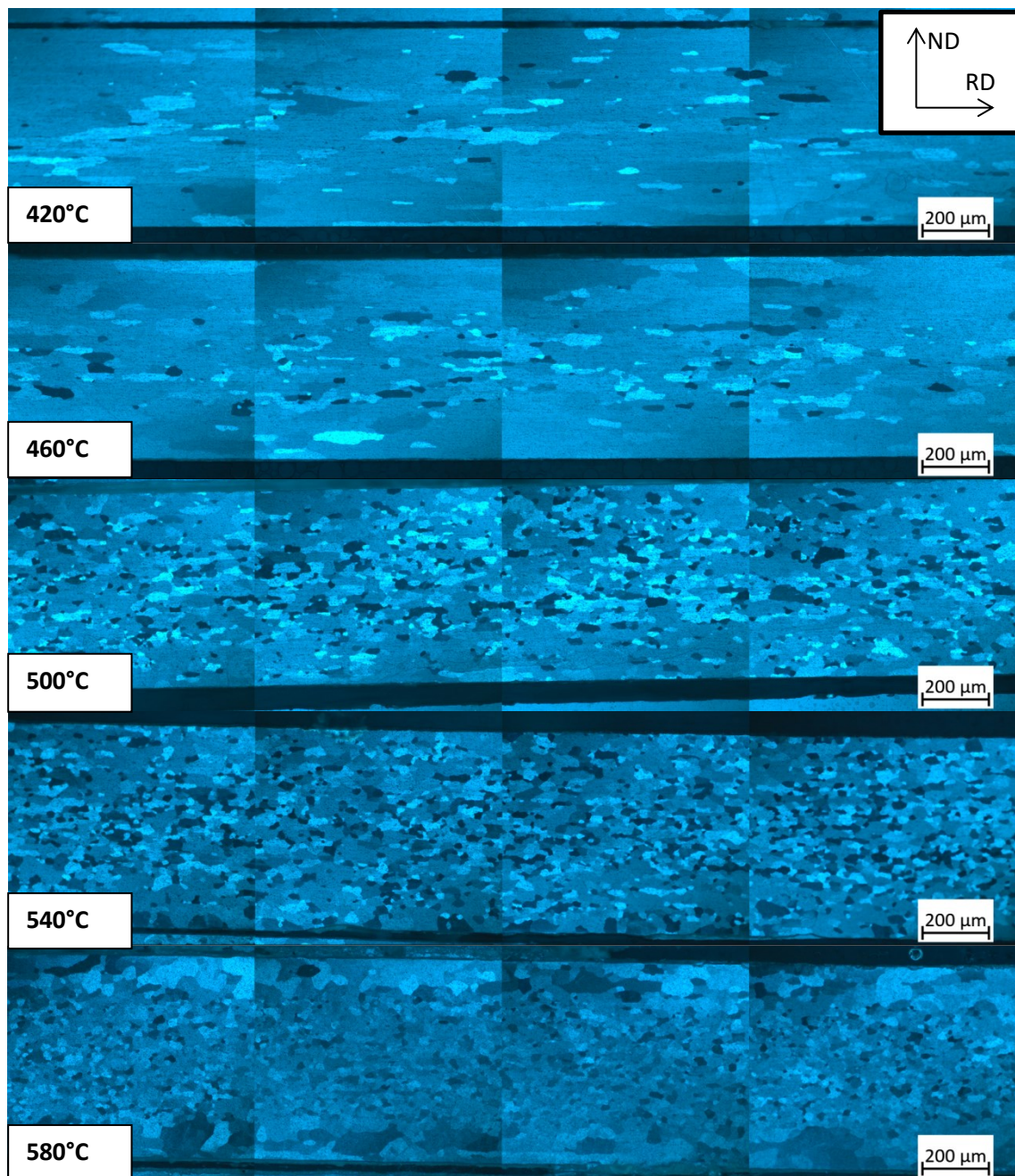
Figure 4.33: Grain structure of the 600 µm material after annealing to 550 °C

Nevertheless, its is worth to mention that the detrimental grain growth was observed at high temperatures. These temperatures would never be employed during a real industrial treatment. Generally, the temperature of intemediate annealing does not exceed 400 °C.

An overview of grain sizes in recrystallized materials is shown in Table 4. Where possible, the intercept method drawing a straight line along the image and counting the number of grains the line intercepts was employed.

	300	350	400	450	500	550	600
420	-	118	158	159	164	162	157
460	-	82	84	75	114	131	124
500	-	57	58	60	61	59	-
540	37	-	40	43	41	41	58
580	43	43	45	48	45	56	-

Table 4.1: Recrystallized grain size of the 600 µm rolled material in µm

The scatter of measured values was estimated to be about 10 % for materials with homogenous grain structures. However, in materials which were less homogenous this error could be up to 20 %.

The homogenized material rolled to 60 µm

There is not a significant difference between the grain structures of the 600 µm and 60 µm rolled materials. The thinner material still contains the same elongated thin grains in the rolling direction (Fig. 4.34). There is still a pronounced coarse surface layer in the 580 °C material showing that even when rolled to extremely thin gauges the effect of growth during homogenization is not fully removed. However in the 540 °C homogenized material the surface layer could not be distinguished anymore. No changes in the grain structure were observed up until 150 °C which was expected from the analysis of microhardness measuerements.

First recrystallized grains are visible at 200 °C in the surface layer of samples homogenized at 580 °C and 540 °C (Fig. 4.35). At 250 °C most of the samples exhibit at least some degree of recrystallization with the exception of the 420 °C homogenized one, which finally shows traces of recrystallization at 300 °C. This is once again in line with the

measured microhardness curves in which the 420 °C homogenized material had its softening shifted towards higher annealing temperatures.

The remaining samples show a more or less homogenous size distribution with varying degrees of recrystallization.
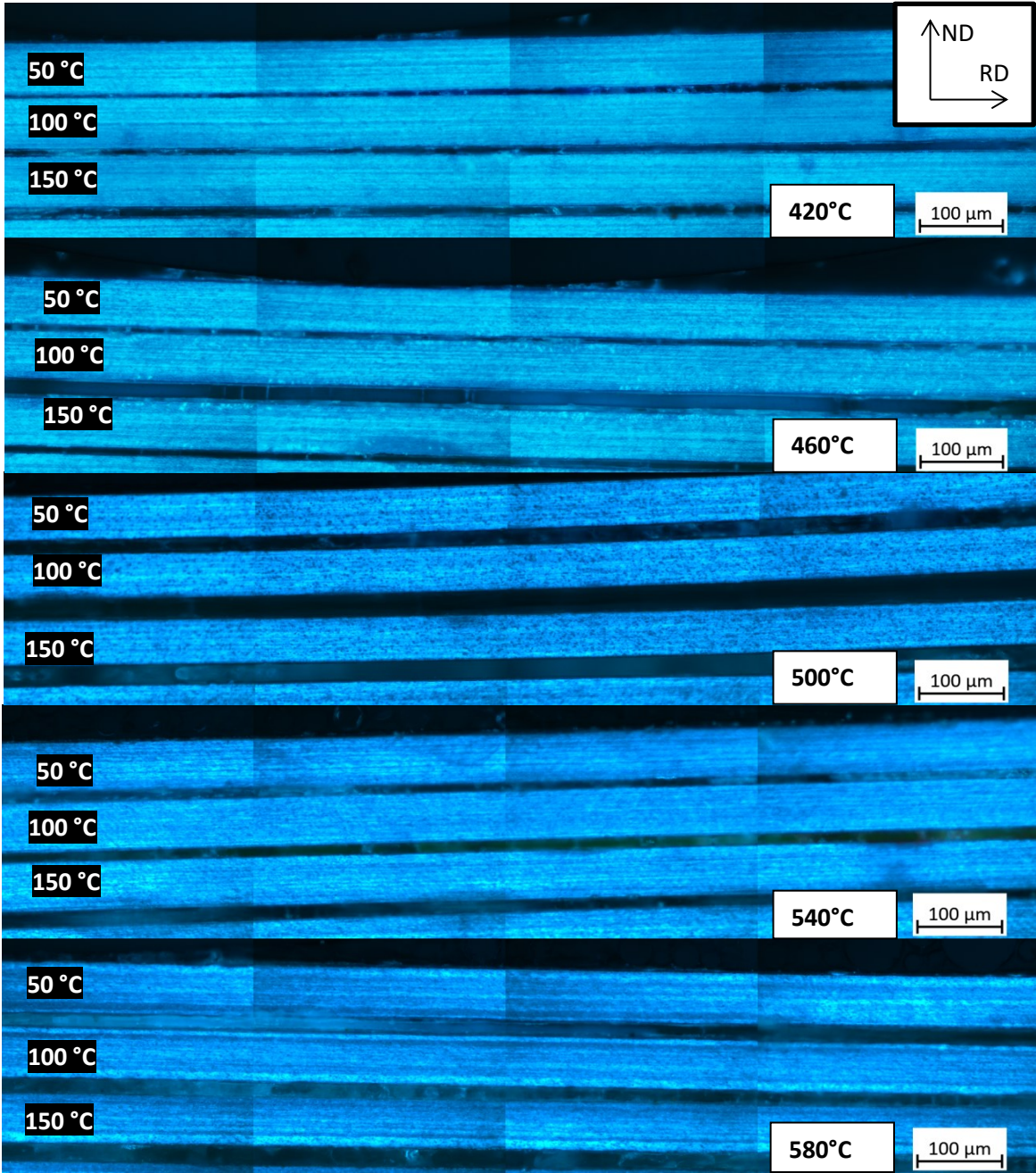
Figure 4.34: Grain structure of the 60 µm rolled material annealed to 50, 100 and 150 °C
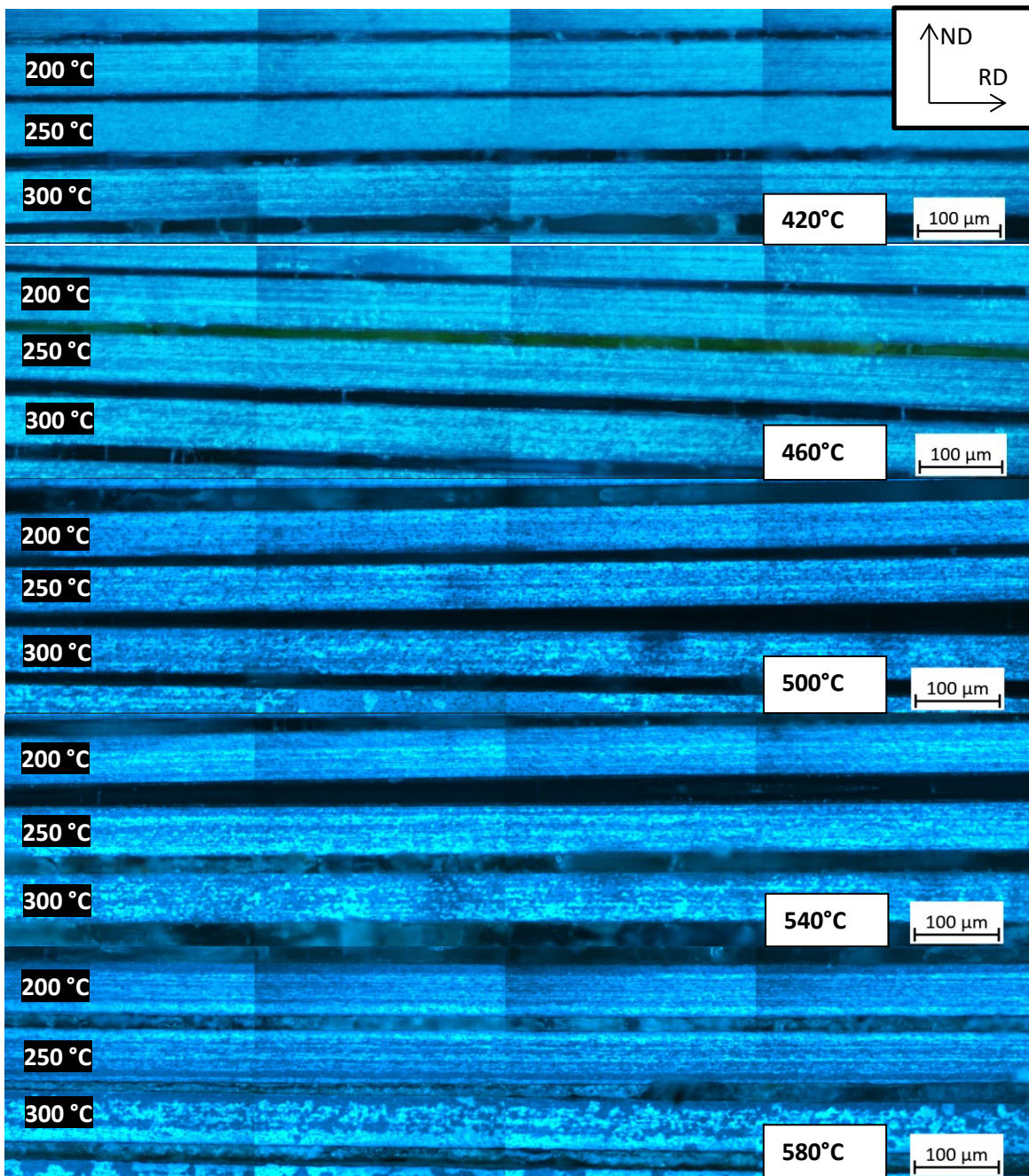
Figure 4.35: Grain structure of the 60 µm rolled material annealed to 200, 250 and 300 °C

A significant difference in structures is observed at higher annealing temperatures (Fig. 4.36). The surface grains start to grow towards the centre of the strip already at 350 °C. The homogenously recrystallized structure of the 500 °C and 460 °C homogenized materials remains mostly stable at 350 °C however at higher temperatures these materials begin to experience significant grain growth consuming the entire width of the strip. The only

materials in which recrystallization continues homogenously up until 450 °C are the 420 °C and 460 °C homogenized ones.
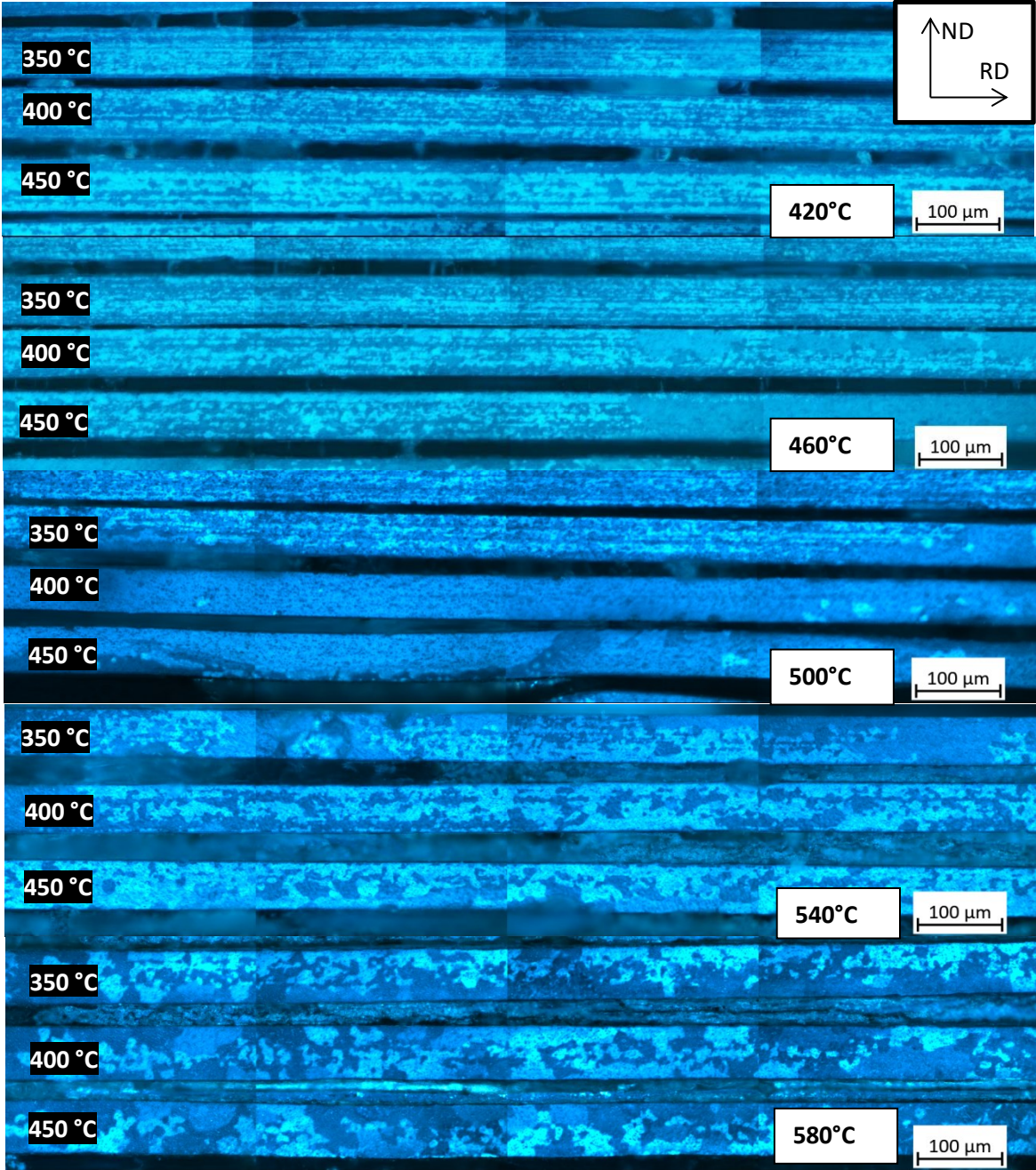
Figure 4.36: Grain structure of the 60 µm rolled material annealed to 350, 400 and 450 °C

These single large grains grow over the entire width of the strips at higher annealing temperatures. The only materials at least partialy resistant to this coarse grain growth are the two with highest homogenization temperatures, which have a coarse grained structure formed at lower temperatures (Fig. 4.37).
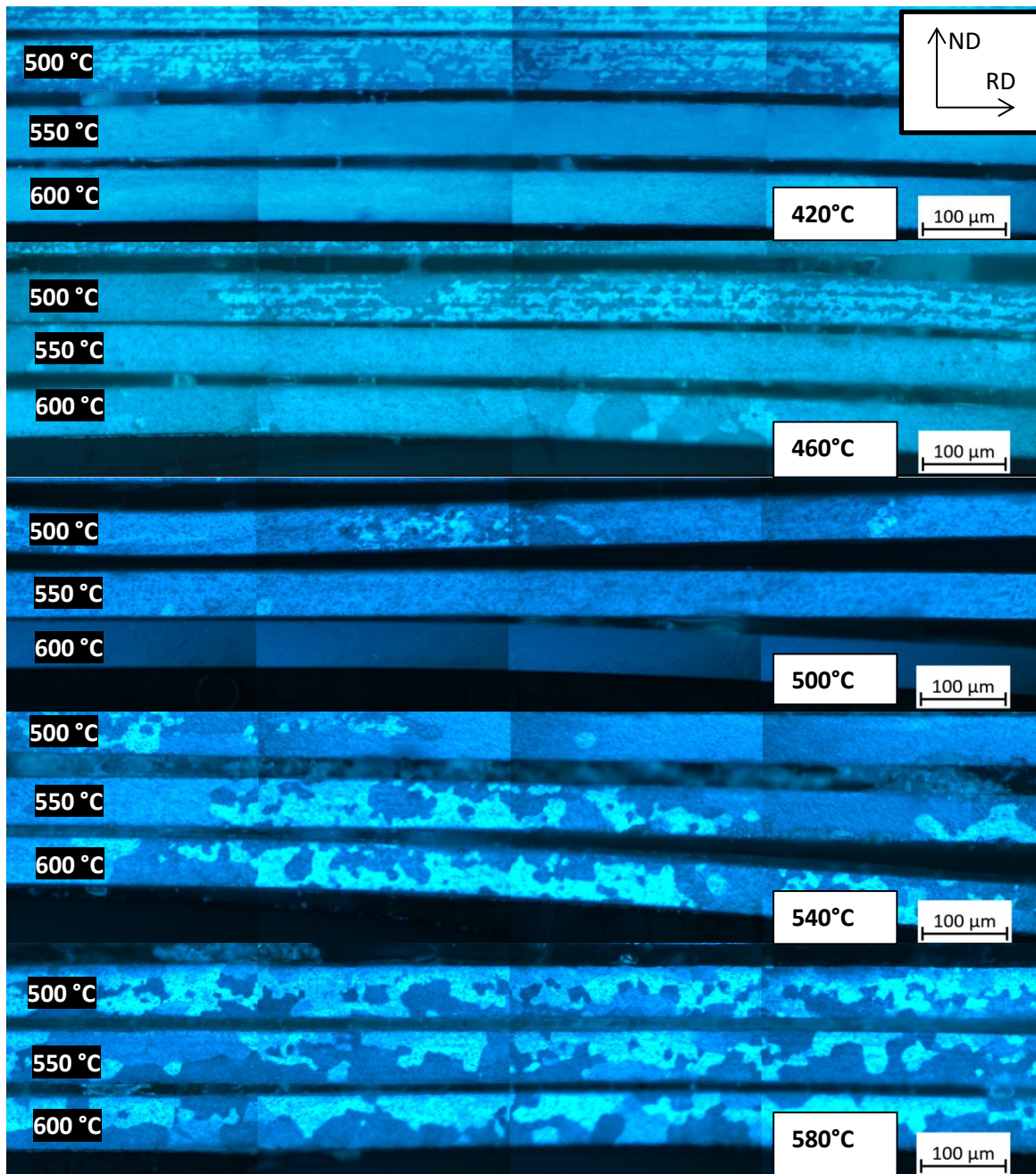
Figure 4.37: Figure 60: Grain structure of the 60 μm rolled material annealed to 500, 550 and 600 °C

The thin samples overall show a higher variation in recrystallization temperatures than the thicker samples. Samples homogenized at higher temperautres suffer from the grain growth during homogenization and show a coarser grain structure after high temperature annealing however, this structure with medium sized grains is more stable and not so susceptible to

grain growth at higher temperatures.

4.4.4. LOM of particle structure in rolled materials

These observations serve mainly to evaluate the average particle size and the volume fraction of particles present after homogenization and subsequent rolling. While the particle size itself does not differ significantly from the homogenized states their distribution is different especially for samples homogenized at lower temperatures, in which the original particle colony structure persisted after the homogenization.

This is clearly confirmed by observing the 420 °C homogenized state (Fig. 4.38), which shows a relatively homogenous dispersion of fine particles, where previously colonies of eutectic particles were present. Some colonies of particles remain undispersed by the rolling process (white circles), but they are marginal. Coarser particles, which were also present after homogenization, are also clearly distinguishable in the material. The images can then be thresholded in order to separate the

Figure 4.38: Particle structure of a 420 °C homogenized 600 µm rolled material

particles from the background of the matrix and the average size and area fraction of these particles can be calculated by an appropriate software (Image J). Results serve as input parameters for the calculation of Zener drag through equation 2.9. A thresholded image is visible in Fig. 4.39 a).

The sample homogenized at 580 °C shows a mixture of finer and coarser particles (Fig. 4.39 b)) similar to the one observed after homogenization. However, the role of rolling is not so pronounced, because their distribution was relatively homogenous after homogenization as well.
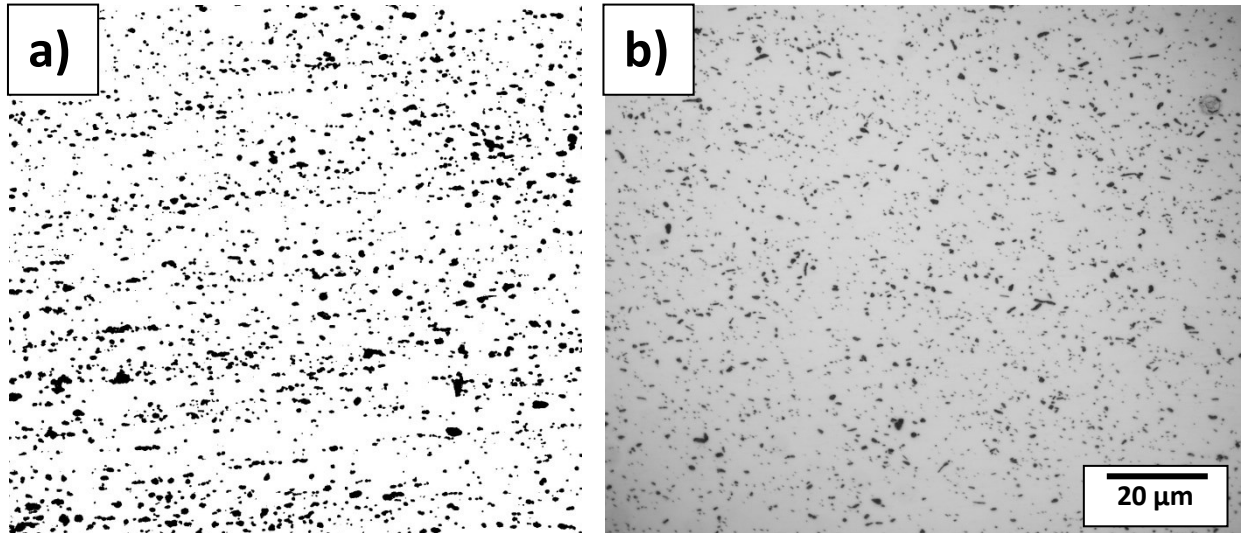
Figure 4.39: a) Example of particle structure thresholding, b) particle structure of a 580 °C homogenized material

This structure is similar in all homogenized states. The rolling process broke down most of existing particle clusters and colonies and a relatively homogenous dispersion of particles present after homogenization is observed. The evaluated particle sizes and volume fractions are summarized in Table 4.2.

However these values are heavily affected by measurement fault. Both the fraction and radius values are heavily dependent on the thresholding which is performed manually as well as the resolution of the used microscope and the ability to distinguish individual particles in their aggregates during thresholding. Due to this the measurement error is estimated to be high approximately 20%.

	fraction [%]	radius [μm]	fraction [%]	radius [μm]
	600 μm		60 μm	
420 °C	9.0	0.48	8.0	0.41
460 °C	7.0	0.53	6.2	0.44
500 °C	7.6	0.55	6.7	0.47
540 °C	5.6	0.58	6.5	0.58
580 °C	5.8	0.61	6.8	0.63

Table 4.2: Area fractions and average radii of observed particles

4.4.5. In-situ TEM and STEM annealing experiment

Annealing experiments were performed on samples of both available thicknesses. To determine the influence of a homogenization temperature on recrystallization behavior and phase composition. The experiments were performed for samples homogenized at 400 °C and 580 °C since the difference in homogenized microstructure is the most significant for these samples.

The annealing regime was adapted from the original cast material experiments with a 25 °C/5 min rate of the temperature increase. However unlike the cast material experiments the initial temperature for these experiments is the equilibrium temperature for the sample inserted into the TEM, which is slightly above 50 °C.

The reason for performing both TEM and STEM annealings is that TEM images could be overwhelmed a contrast from the dislocation structure of the deformed material, as seen in overview images (Fig. 4.40). This is however not the case for STEM images (Fig. 4.41) which are much less sensitive to contrast from dislocations and much more sensitive to contrast originating from subgrain and grain boundaries and particles which is certainly beneficial for this type of experiment.
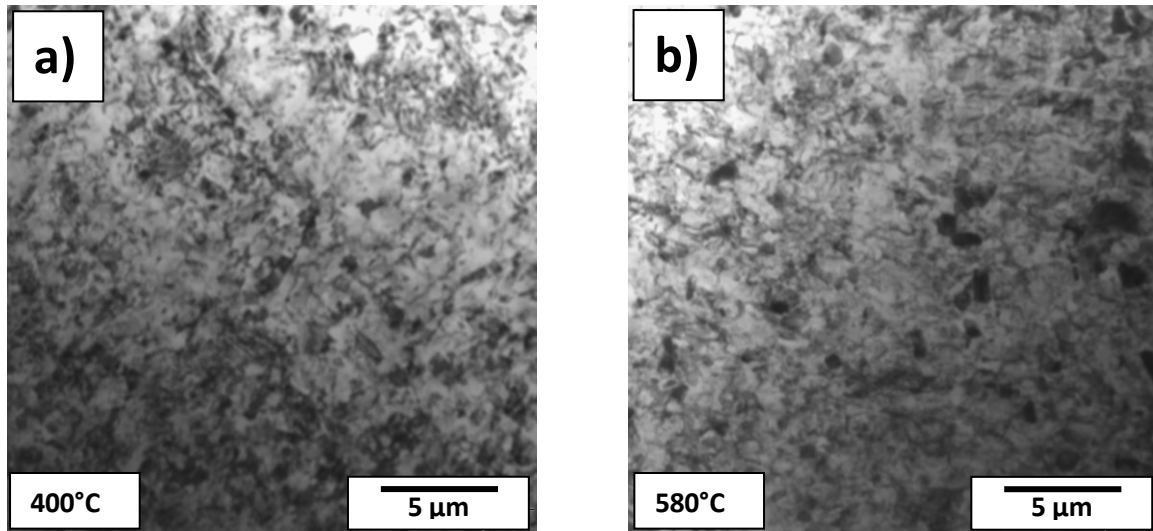
Figure 4.40: TEM overview images of materials homogenized at a) 400 °C b) 580 °C
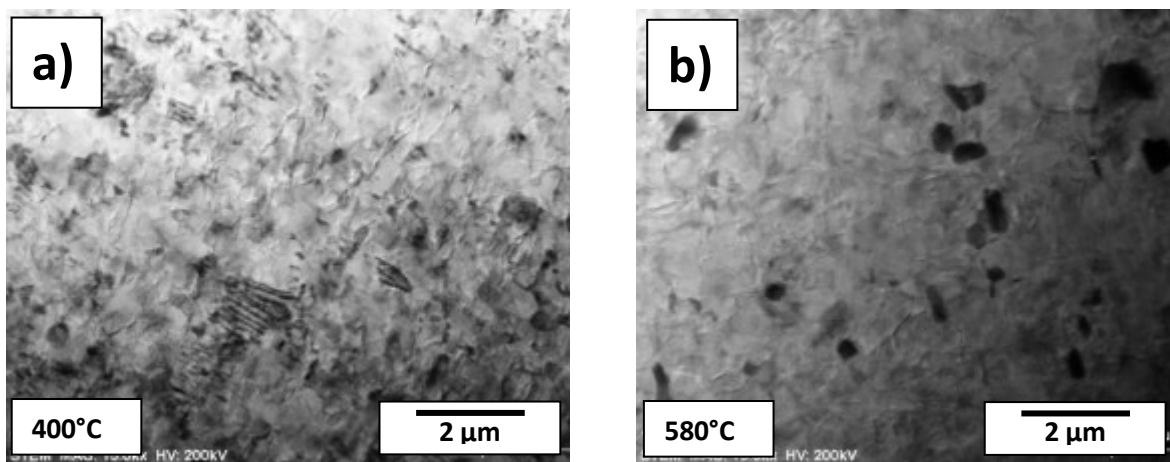
Figure 4.41: STEM images of materials homogenized at a) 400 °C b) 580 °C

Both Fig. 4.40 and 4.41 are taken from the same area of the sample. This is slightly more visible for the b) images as the size contrast of the particles after homogenization is more pronounced. However any kind of detail is completely lost in the TEM image of the material homogenized at 400 °C (Fig. 4.40 a)).

The 600 μm rolled 400 °C homogenized material

Similarly to the previous images the amount of deformation in these samples makes regular TEM images too messy to analyze (Fig 4.42 a)). While the eutectic particles present in the material are visible in the STEM image the dislocation structure is so dense even the STEM image is initialy distorted (Fig. 4.42 b)). The selected colony serves as a reference point for observations during the annealing experiment as well as a subject of phase transformations that could occur at higher temperatures seeing as the low homogenization temperature left the initial particle structure unchanged.
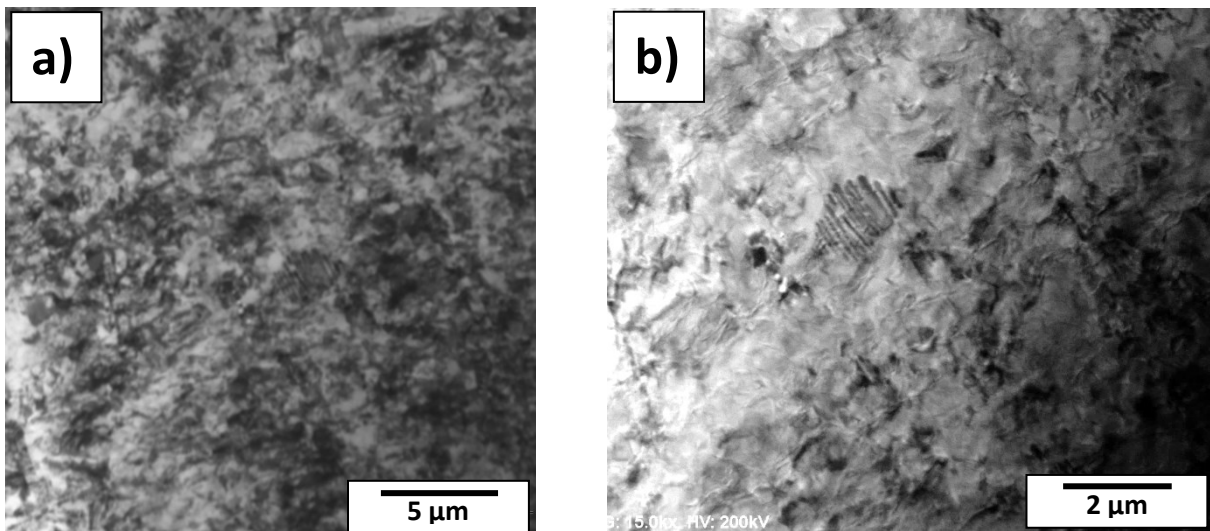
Figure 4.42: Initial state of the 400 °C homogenized 600 μm rolled material in: a) TEM, b) STEM

The first process occuring in the material is a recovery of the dislocation structure and polygonization. This begins almost immediately at 100 °C and continuesat higher annealing temperatures. At 350 °C (Fig. 4.43) the TEM image is much clearer however contrast of the differently oriented domains still prevails. The STEM image reveals more of the materials particle structure – the original colonies of particles were broken down by the rolling process however certain clusters of particles remain intact. The particles are stable even at this temperature.

Figure 4.43: State of the 400 °C homogenized 600 µm rolled material after annealing to 350 °C in: a) TEM, b) STEM

The material changes continue by a growth of selected subgains consuming the energetically less favourable ones and finally at 450 °C (Fig. 4.44) spheroidization of particles is also observed. This is very close to the temperature at which spheroidization was observed in the cast material showing that the rolling process does not significantly affect the temperature of occuring phase transformations.
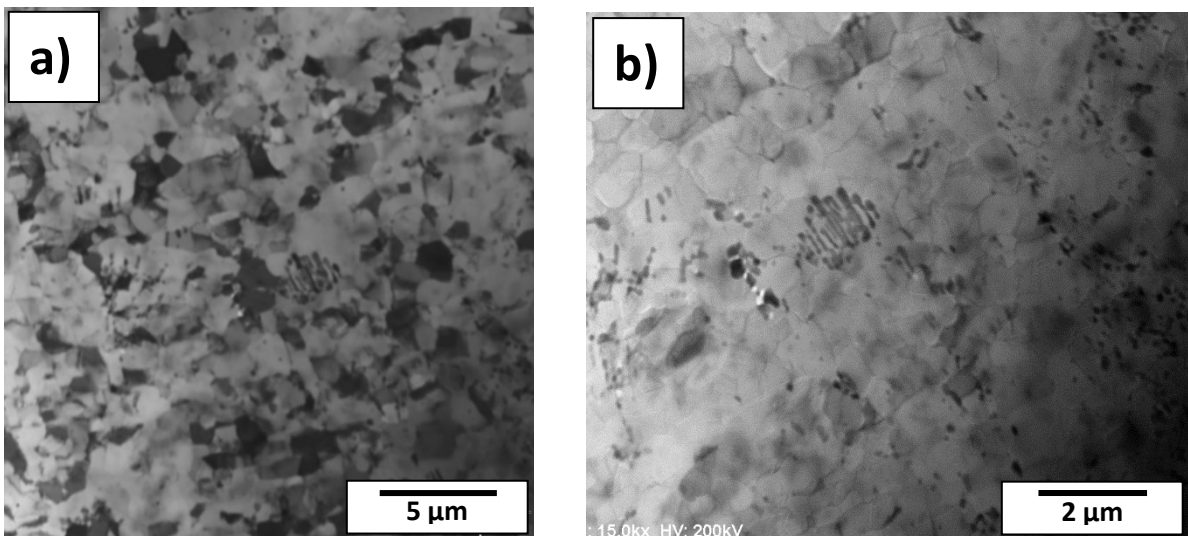
Figure 4.44: State of the 400 °C homogenized 600 µm rolled material after annealing to 450 °C in: a) TEM, b) STEM

The process continues with further spheroidization of particles, their consecutive dissolution and subgrain growth. The final state of the particles at 550 °C is once again a mixture differently oriented coarse particles (Fig. 4.45 b)) with remnants of the undisolved spherical particles still present. Similarly the subgrains further grow consuming a large part of the smaller subgrains in the process (Fig. 4.45 a)).
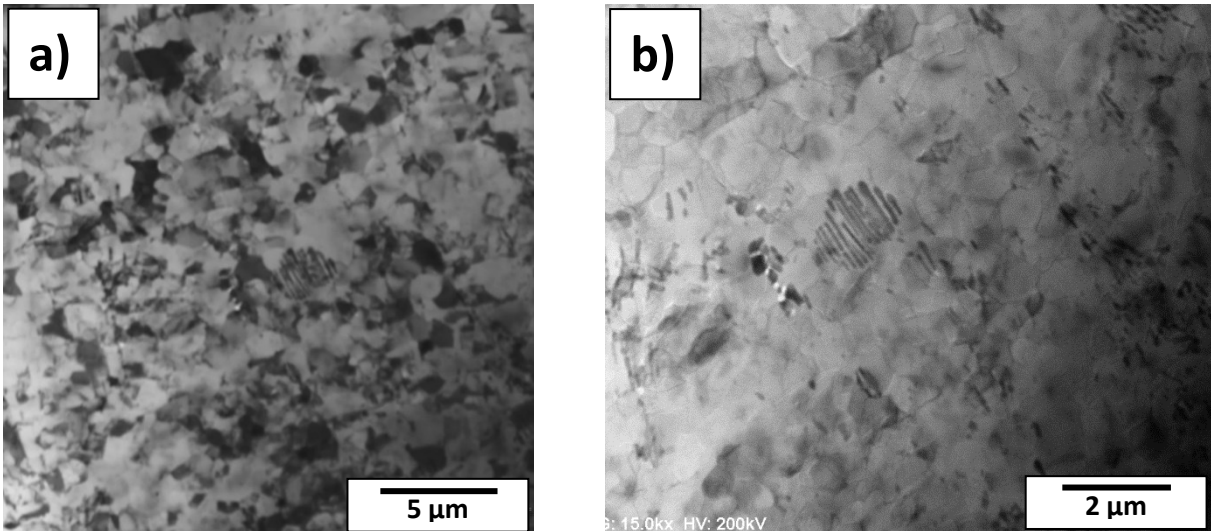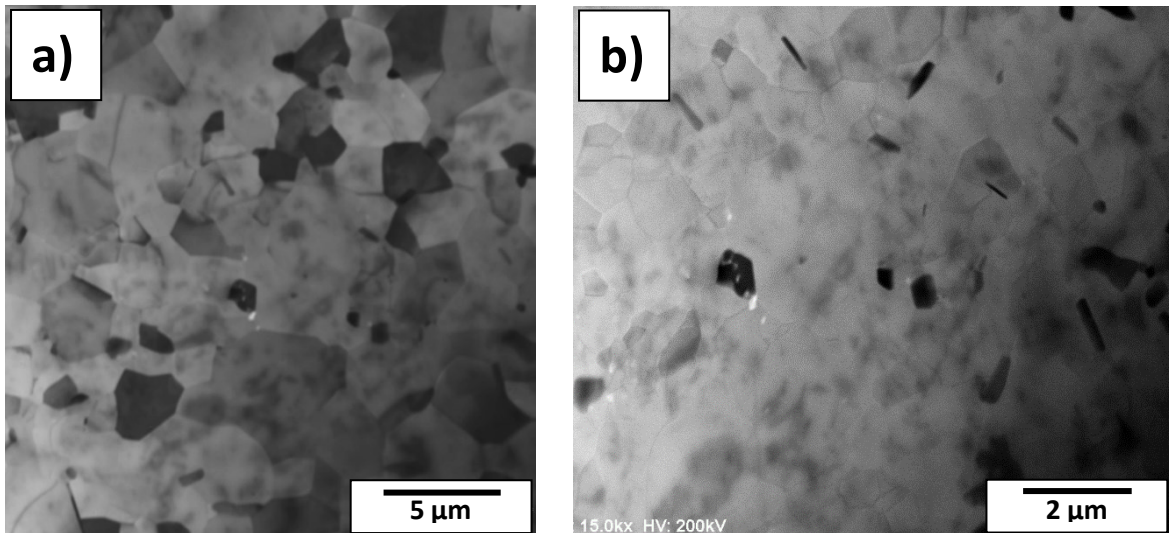

Figure 4.45: State of the 400 °C homogenized 600 µm rolled material in: a) TEM at 575 °C, b) STEM at 550 °C

Further annealing at higher temperatures resulted in a destruction of the sample.

The 600 µm rolled 580 °C homogenized material

The material contains coarser particles as a result of the high homogenization temperature. Similarly the degree of deformation is high and as such both the TEM and the STEM images are affected (Fig. 4.46). The recovery process starts almost immediately after the annealing is initiated at around 100 °C. Unlike in the 400 °C homogenized material the recovery process is more rapid with a simmilar degree of recovery observed at 275 °C (Fig. 4.47) as was observed in the previous material at 350 °C. An important thing to note is that there is no clear line for a „high degree of recovery" and as such the observations might be misleading.
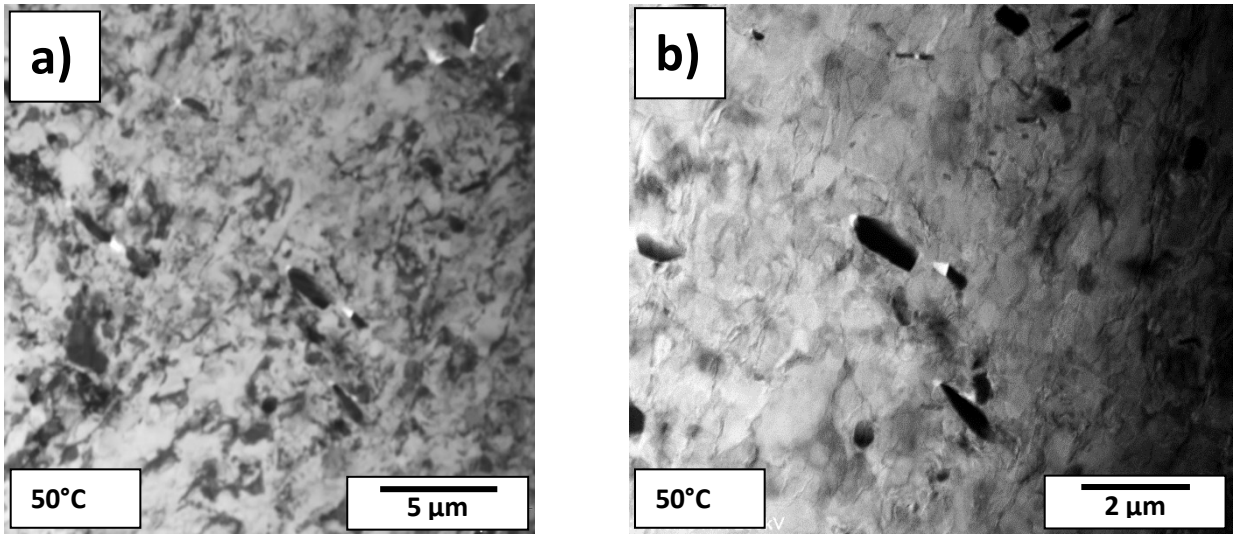
Figure 4.46: Initial state of the 580 °C homogenized 600 µm rolled material: a) TEM,
b) STEM
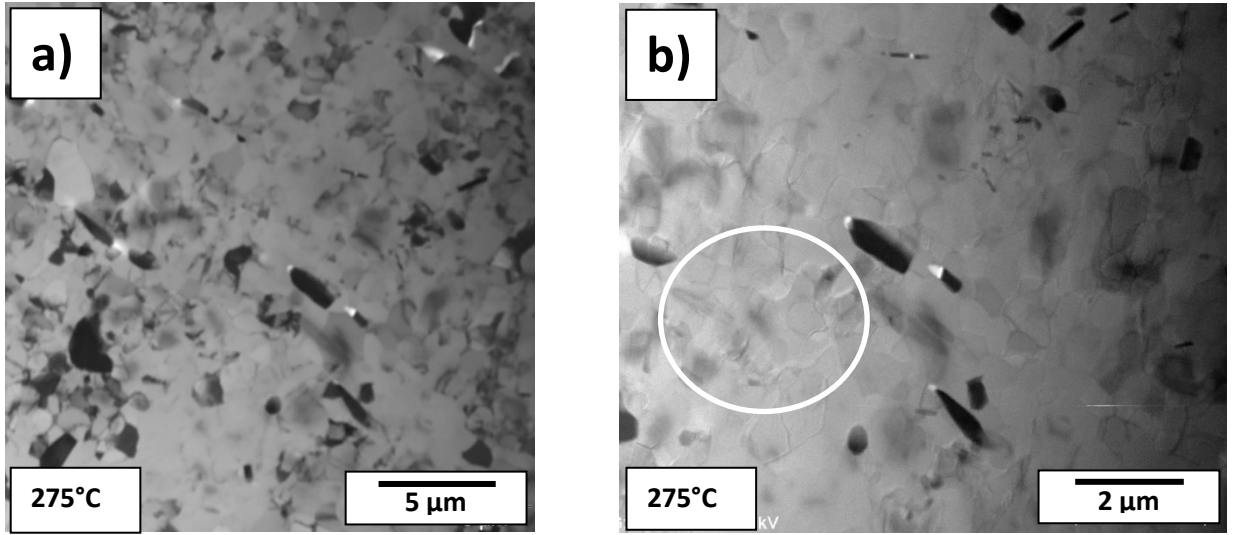
Figure 4.47: State of the 580 °C homogenized 600 µm rolled material annealed at 275 °C in:
a) TEM, b) STEM

From here on we mainly focus on the state of particles and the subgrain structure of the material. There is not much change expected for the particles seeing as they have already coarsened during homogenization however there is still a fraction of finer particles present that might be a subject of interest.

The finer particles begin to dissolve at temperatures close to 525 °C and higher once again in favour of other already coarsened particles. This is well visible during annealing at 575 °C. While the change the size of coarse particles is relatively low the fine particles scattered in the top right corner of the STEM image have obviously dissolved (Fig. 4.48). Fig. 4.47 also shows a vastly different grain structure with a significant grain growth. only impeded by the remaining particles. The STEM images show this progression well (Fig. 4.49) as the subgrain structure remains relatively stable after annealing to 425 °C.

Figure 4.48: STEM of the 580 °C homogenized 600 μm rolled material at 575 °C

At higher temperatures some more energeticaly beneficial subgrains grow at the expense of other grains. At 575 °C (Fig. 4.48) a sudden increase in grain growth occurs compared to the lower temperatures
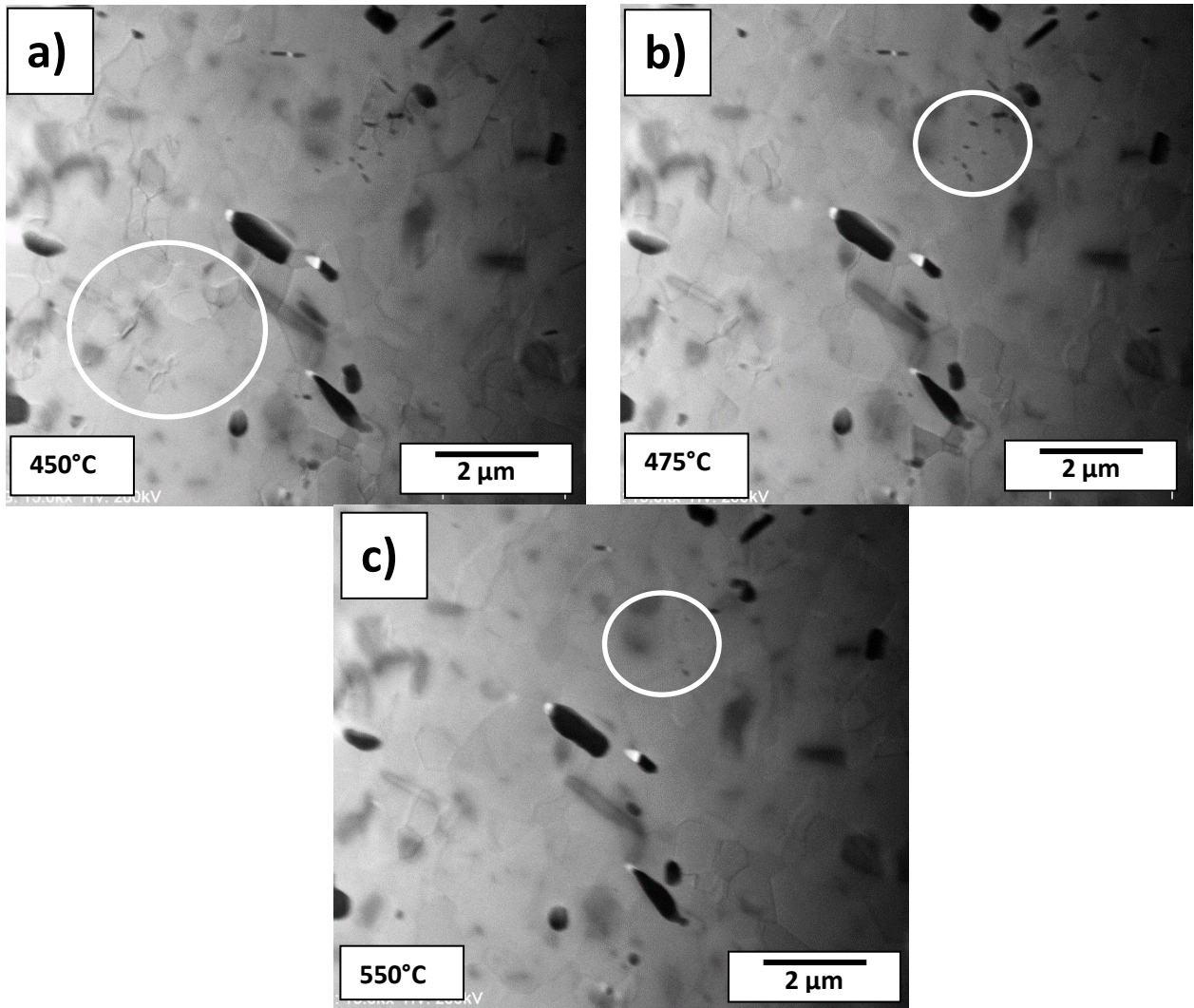
Figure 4.49: STEM of the 580 °C homogenized 600 µm rolled material annealed at: a) 450 °C, b) 475 °C, c) 550 °C

The 60 μm rolled homogenized materials

The thinner rolled materials, despite showing a significantly different recrystallization process as seen in the LOM images, do not behave much differently during the in-situ annealing. This is potentialy because the nature of the samples is the same regardless of the rolling thickness prior to the sample's extraction and polishing.

Once again recovery occurs right after the initiation of the annealing with the higher temperature homogenized material showing a higher degree of recovery at lower temperatures (Fig. 4.50 a,b)). The recovery process establishes a subgrain structure that remains mostly stable (Fig. 4.51 a,b)) with only a slight growth of a select few subgrains up to about 500 °C. Once this temperature is reached (Fig. 4.51 c, d)) the grain growth starts rapidly peaking at the last observed temperature of 575 °C when only a few of the smaller grains remain mostly in the vicinity of the observed intermetallic particles.
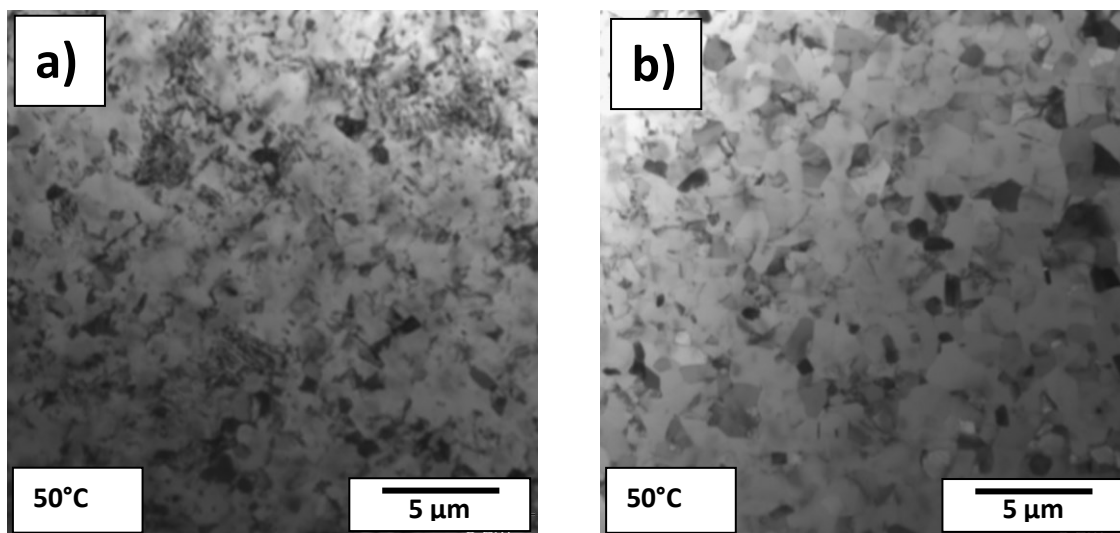
Figure 4.50: TEM images of the 60 μm rolled materials upon annealing to 250 °C:
a) homogenized at 400 °C, b) homogenized at 580 °C

Behaviour of particles in these thinner samples is also similar with spheroidization occuring for the lower temperature homogenized material. A spheroidization of the particles leads to their dissolution and the occurence of Ostwald ripening (Fig. 4.51 c), Fig. 4.52 a)). However the spheroidization occurs earlier at about 450 °C and the coarsening starts immediately after at 475 °C (Fig. 4.53).
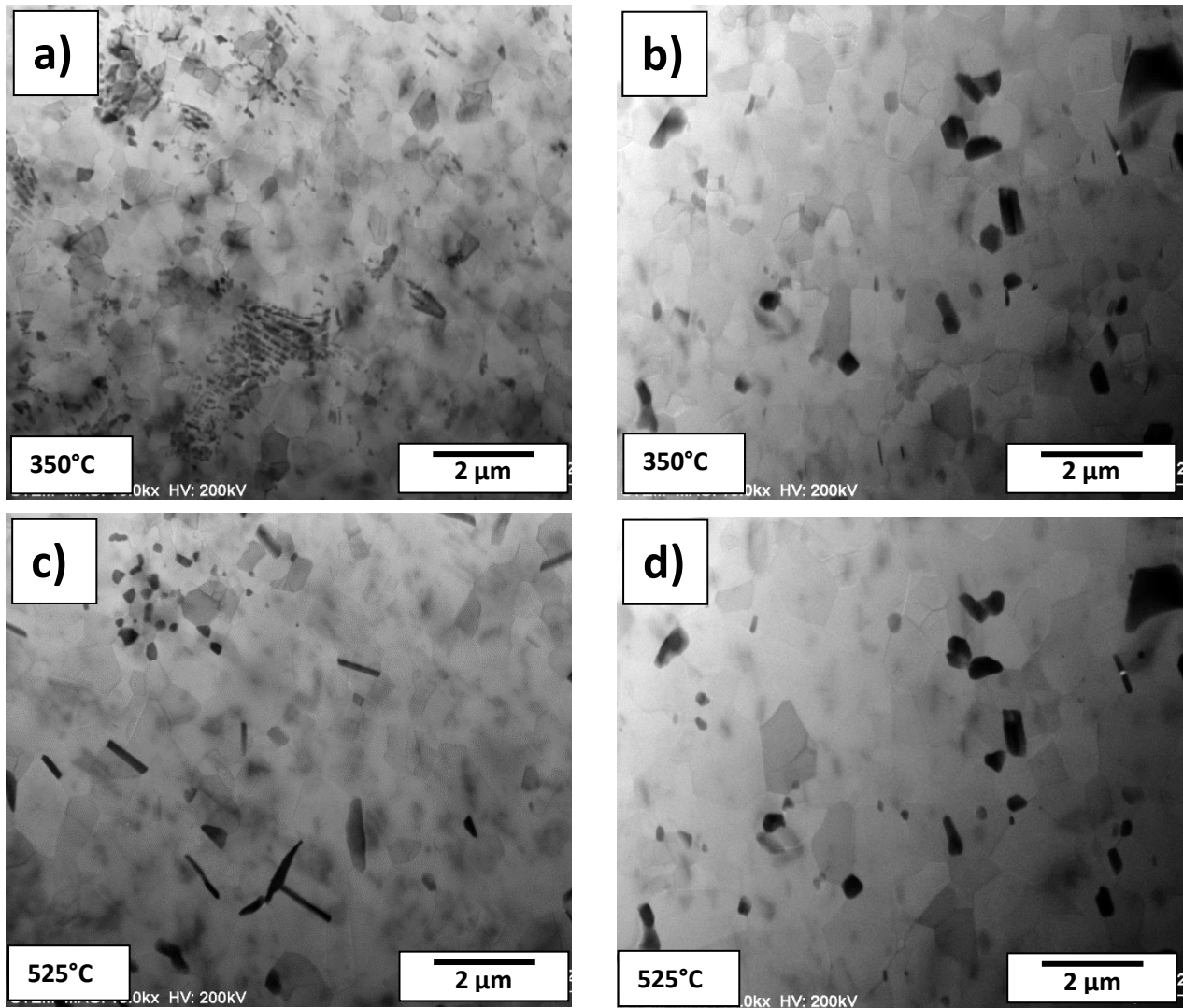
Figure 4.51: STEM images of the 60 µm rolled materials: a) homogenized at 400 °C annealed to 350 °C, b) homogenized at 580 °C annealed to 350 °C, c) homogenized at 400 °C annealed to 525 °C, d) homogenized at 580 °C annealed to 525 °C

Figure 4.52: STEM images of the 60 µm rolled materials annealed to 575 °C: a) homogenized at 400 °C, b) homogenized at 580 °C

Figure 4.53: STEM images of the 60 µm rolled materials homogenized at 400 °C:
a) annealed to 450 °C, b) annealed to 475 °C

4.5. Isothermal annealing of the homogenized and rolled material

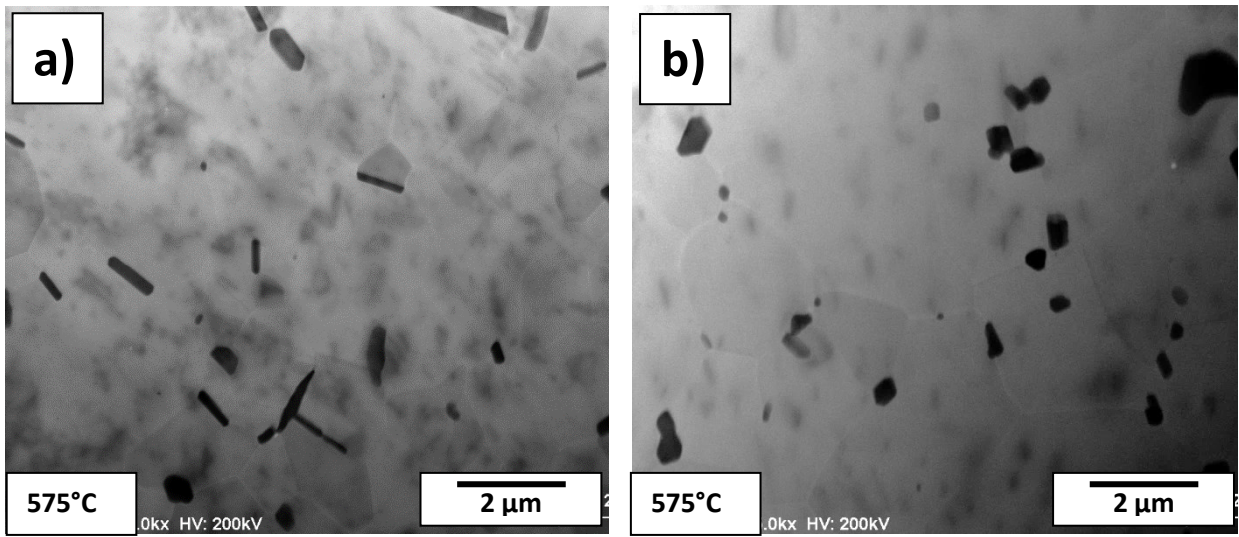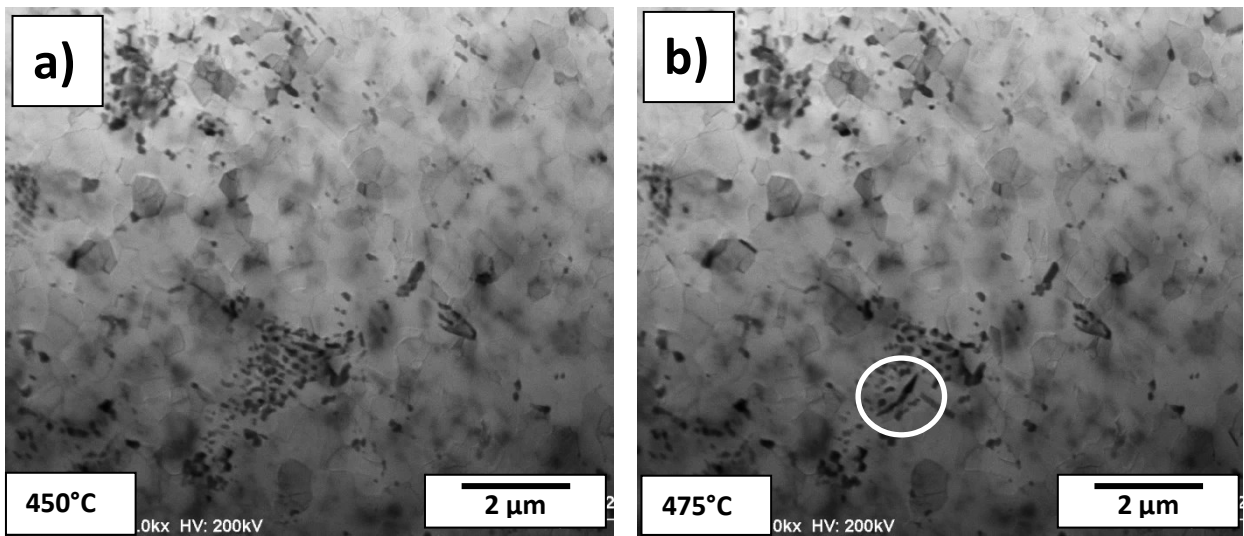To finalize the study an isothermal annealing of the material is required to determine the recrystallization kinetics at different temperatures of interest in the various homogenized and rolled states. A series of samples was prepared for annealing at three selected temperatures – 250 °C, 275 °C and 300 °C. These temperatures were selected based on the results of the isochronal annealing. 250 °C is the lowest temperature to initialize recrystallization in a reasonable period of time. Similarly temperatures above 300 °C could lead to a recrystallization that occurs too fast. Samples from the series were quenched at selected temperature intervals – 10, 20, 40, 80, 160, 320 and 480 minutes. Aditional measurement was then performed after 960 minutes for samples that showed little to no recrystallization even after 480 minutes.

The recrystallized volume fraction of the material was measured through the microhardness model. These volume fractions are shown in a semilogarithmic plot. The Avrami plot axis values were then calculated and analyzed in order to determine the *n* constant of the process.

The results and commentary are once again split between the two material thicknesses.

4.5.1 The 600 µm thick homogenized materials

Calculating the recrystallized volume fraction by the microhardness model brings the question of which values of microhardness to use as HV_0 and HV_e the initial and recrystallized microhardnesses respectively. For the 600 µm rolled material this is fairly simple. The microhardness values measured during the isochronal annealing are fairly stable and differ only within the range of the measurement scatter until the decrease in the 250 °C – 300 °C interval and as such almost any of these values can be used. Similarly after the material softened at 350 °C the microhardness values once again showed very little variation outside of the experimental scatter. While this makes normalizing the sigmoidal curve simple it might not always be the case and will not be the case for the thinner rolled material.

Based on the results of the isochronal annealing of the thicker material series it would be expected for the higher temperature homogenized materials to recrystalize after shorter periods of time. This holds true for 275 °C and 300 °C (Fig. 4.54 c,e) however recrystallization at 250 °C (Fig. 4.54 a) shows recrystallization begins after a 480 m hold at the temperature and for a majority of the homogenization temperatures does not fully recrystalize even after 960 min. This presents an issue with evaluating the Avrami plot (Fig. 4.54 b) as

most materials only contain up to two points for regression and in the case of the 420 °C homogenized material there are no signs of recrystallization at all.

Not only do the higher temperature homogenized materials recrystallize after shorter time intervals they also show a higher degree of recrystallization after the initial 10 m time period. For recrystallization at 300 °C (Fig. 4.54 e) almost all the materials recrystallize after 160 min with the exception of the 420 °C homogenized one which finishes recrystallizing after about 320 min. The materials do not show further softening after recrystallizing at this temperature.

Similarly at 275 °C the materials recrystallize after upwards of 480 min. The 420 °C homogenized material is once again the exception as it does not recrystallize even after an extended 960 min annealing.

For a proper analysis according to Eq. 2.7 only the points according in the steep part of the Avrami curves are selected as the points measured at a stage of the material during which recrystallization has not yet initiated or has already finished would only shift the n values towards lower unreasonable numbers. The values of the Avrami constant n for the 600 µm rolled material are listed in Table 4.3.

Both the recrystallized volume fraction values and parameter n values are affected by the scatter of microhardness values. This scatter results in an error of approximately 0.06 of X_V. The regression error is significantly lower than the measurement error. An equivalent error for the Avrami plot values was estimated as 0.15.

Figure 4.54: Recrystallization curves of the 600 μm rolled material: a) sigmoidal curve at 250 °C , b) Avrami plot at 250 °C, c) sigmoidal curve at 275 °C, d) Avrami plot at 275 °C, e) sigmoidal curve at 300 °C, f) Avrami plot at 300 °C

n 600 μm	250	275	300
420°C	-	-	1.3
460°C	0.9	1.0	1.1
500°C	2.3	1.0	1.2
540°C	1.5	1.0	1.4
580°C	1.3	0.8	0.9

Table 4.3: The Avrami n constant values of the 600 μm material recrystallization

There are no values for comparison between the annealing temperatures of the 420 °C homogenized material due to the lack of measured points. There is also a discrepancy for the remaining values of 250 °C recrystallization as these values are overall higher due to the afforementioned lack of measured points. The only value that remains somewhat in accordance with the other is for the 460 °C material. The value for 500 °C at 250 °C is clearly way too high.

All the calculated values of n are slightly higher than 1 with the exception of the 580 °C homogenized material. This is possibly due to an early recrystallization and coarsening of the surface layer. The use of Avrami formalism is thus not rigorous.

4.5.2. The 60 μm thick homogenized materials

The choice of a starting hardness and recrystallized hardness is a bit less trivial as the decrease was not instantaneous during the isochronal annealing and seeing as it started even before reaching the selected temperatures for the isothermal annealing. A value from the last measured temperature before the isothermal annealing temperature was usualy selected for the initial value and similarly the recrystallized hardness value was usualy selected as the next measured point beyond the isothermal annealing temperature. In certain situations these values yielded results that were clearly wrong and different value from the isochronal annealing microhardness curve was calculated instead.

The curves (Fig. 4.55 a,c,d)) do not follow as well a theoretical sigmoidal shape as the thicker materials.

Similarly to the thicker material the 250 °C annealing results in a higher recrystallized fraction in the higher temperature homogenized materials (Fig. 4.55 a). This is also the case for the 275 °C and 300 °C isotherms. The 300 °C annealing (Fig. 4.55 e) results in a sigmoidal curve for the 420 °C homogenized material. The higher temperature homogenized material curves have a concave shape possibly because the nucleation of recrystallized grains occurs very early in the process well below the initial 10 min interval. This might also be the case for the 275 °C with the two lowest temperature homogenized material curves having a shape reminiscent of the sigmoidal curve however the higher temperature homogenized material curves are flatter similar to the curves received from the 250 °C isotherms.

As a result of these flatter curves the Avrami plot curves do not show a sigmoidal shape, at least not to such an extent. Therefore only parts of Avrami plots representing recrystallization were used for the evaluation of n. The measured values for the parameter n are shown in Table 8.

Overall the n values for the 60 µm rolled material are significantly lower all being well below 1 and are generally around 0.6. Interestingly enough both the materials show lower values of the parameter n for the isotherms measured at 275 °C than for the other two, which is not in line with the expectation of the parameter being annealing temperature independent, which held more or less true for the thicker material. The measurement errors are larger due to issues with microhardness measurements discussed in part 4.3.1. The errors are therefore estimated as 0.1 and 0.25 for X_V and Avrami plot points respectively.

n 60 µm	250	275	300
420°C	0.6	0.4	0.8
460°C	0.7	0.3	0.6
500°C	0.7	0.4	0.6
540°C	0.6	0.3	0.5
580°C	0.5	0.3	0.6

Table 4.4: The n values of the 60 µm material recrystallization process
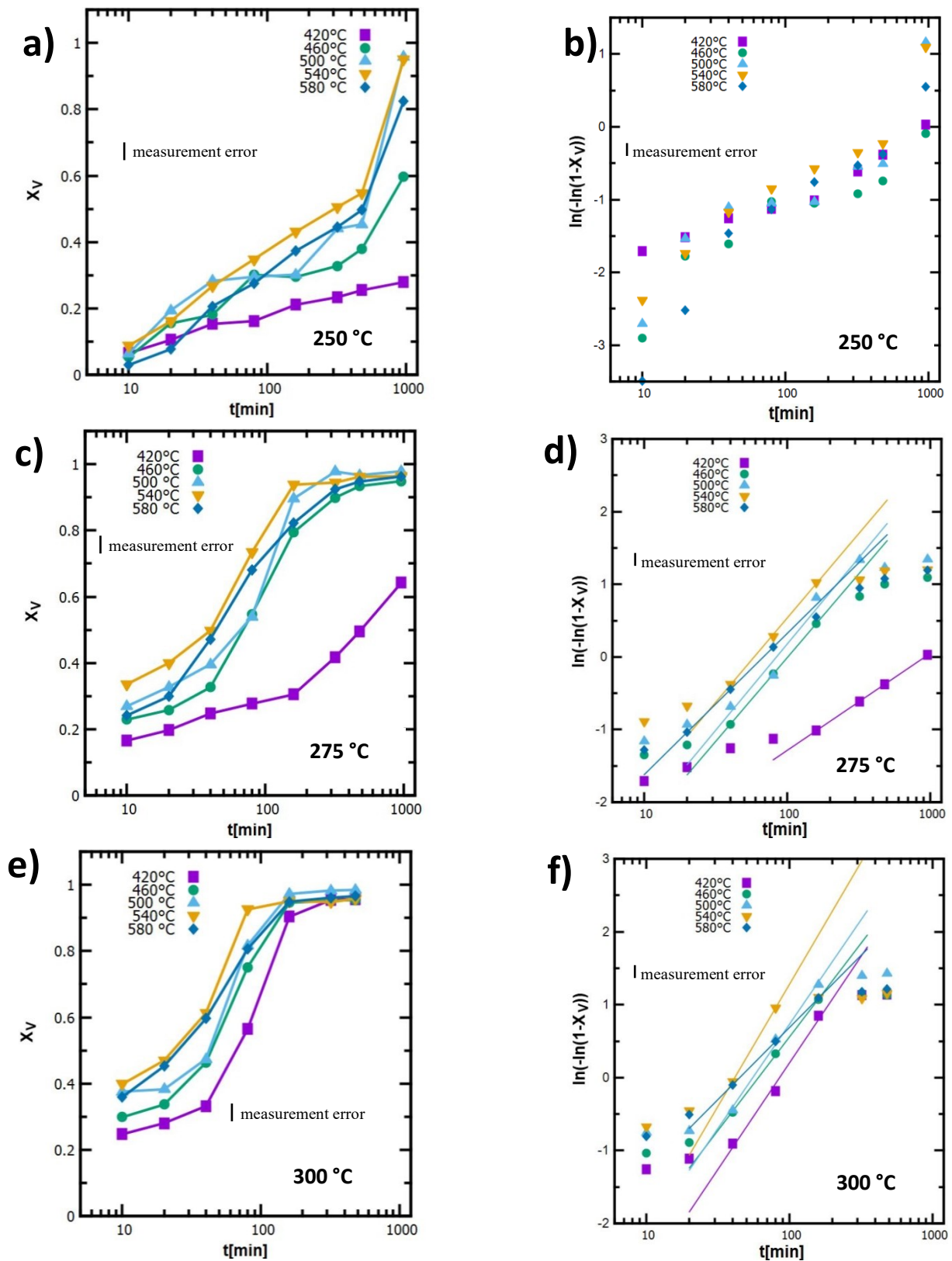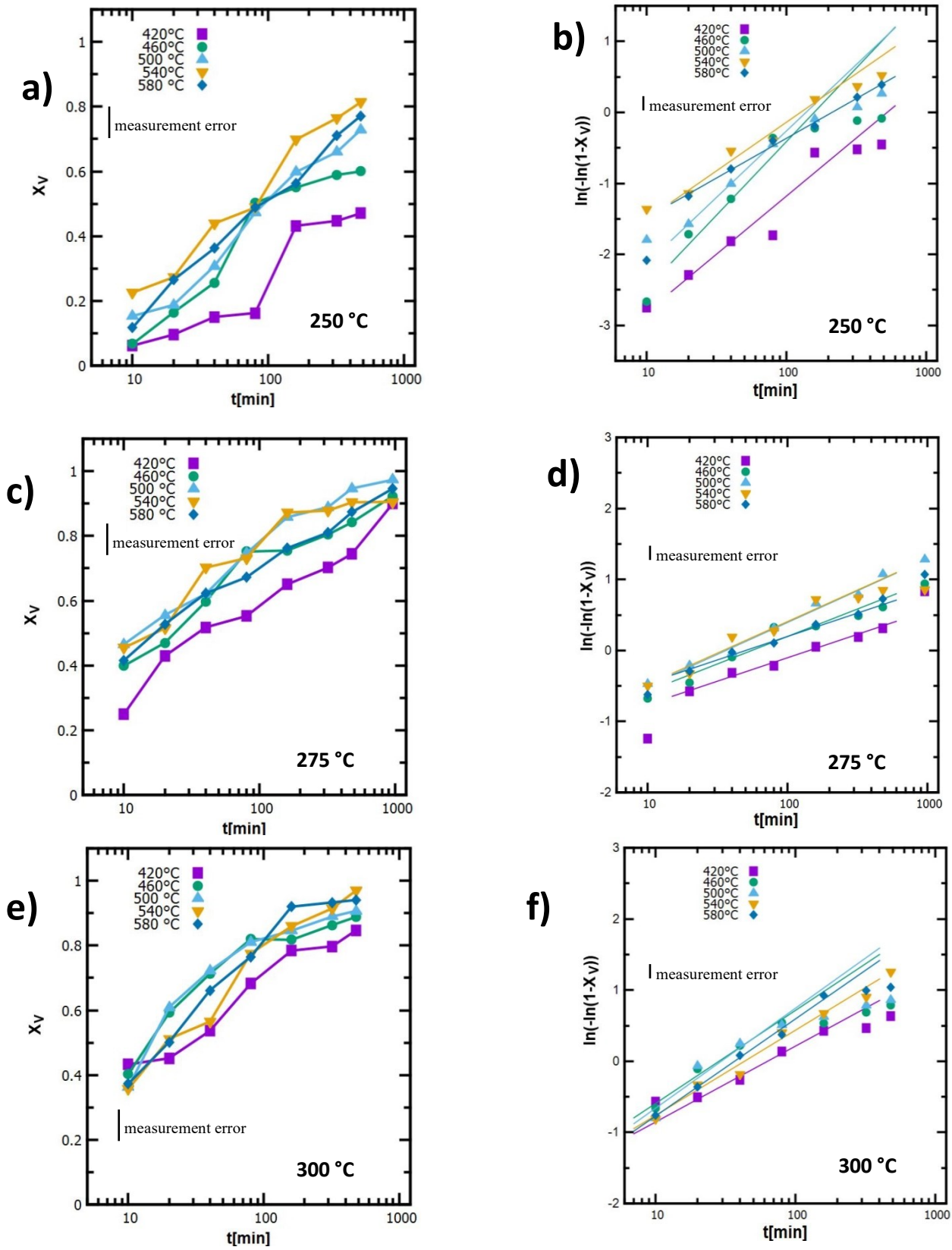
Figure 4.55: Recrystallization curves of the 60 µm rolled material: a) sigmoidal curve at 250 °C , b) Avrami plot at 250 °C, c) sigmoidal curve at 275 °C, d) Avrami plot at 275 °C, e)

sigmoidal curve at 300 °C, f) Avrami plot at 300 °C

5. Discussion

5.1. As-cast state

The 8mm thick TRC strip shows typical TRC microstructure with very fine grains at the surface of the strip gradualy growing towards the centre of the strip. The grains are elongated in the direction of rolling during casting and the aspect ratio of individual grains decreases towards the center of the strip. Thin needle shaped particles formed in colonies around eutectic cells. The LOM observations (Fig. 4.3) showed that they are smaller than individual grains, TEM observations (Fig. 4.6) then confirmed that they enclose groups of subgrains. The high Fe/Si ratio of the material combined with the observed shape and distribution indicates that these should be the $Al_{13}Fe_4$ particles with a possible undefined fraction of metastable AlFe phases present [59].

5.2. Isochronal annealing of the as-cast strip

The resistivity measurements showed little change in the material at lower temperatures below 300 °C. Comparing this with the in-situ TEM annealing (Fig. 4.8) experiment only recovery was observed at this point during the annealing. Considering a low contribution of dislocations to the total resistivity of the material and low dislocation density observed in TEM these results correlate well. Above 300 °C the resistivity significantly decreases up to about 450 °C at which then stays relatively constant up to about 520 °C and increases again above this temperature. Comparing this with the in-situ annealing it seems that signicifant matrix depletion occurs before the particle spheroidization.

78

During the spheroidization the resistivity remains constant and starts to increase again coinciding with dissolution and coarsening of particles. Assuming the particles have a minor influence on the resistivity compared to matrix saturation this means that a reversion of solutes into matrix occurs. This makes sense assuming that a portion of the solute elements present in the dissolved particles remain in the matrix. This is an effect that was previously observed in studies that performed chemical analysis of the aluminum matrix at different stages of annealing [59]. An estimation of Fe concentration in the matrix was made from these results (Fig. 5.1). This estimation assumed equilibrium iron concentration in the matrix at the point of lowest measured resistivity and complete dissolution of Si in the matrix. We assume that the material has the equilibrium solubility of iron at 600 °C. Furthermore the measurements were performed in liquid nitrogen in which aluminum has resistivity value of 0.25 $\mu\Omega$.cm [3]. The equation used was Eq. 2.11. The graph unsurprisingly follows the same shape as the resistivity curve showing about 0.048 at.% concentration of Fe in the Al matrix in the as-cast state dropping to approximately 0.016 at.% at 500 °C. Higher

Figure 5.1: Estimated iron content in the Al matrix

temperatures are responsible for the reversion of the solid solution to equilibrium concentration of 0.025 at% at 600 °C [3] in accordance with the estimation.

5.3. Homogenization

Homogenization processes occur in accordance with published results observed by other authors [65] as well as the in-situ experiment (Fig. 4.8). The obtained microstructures range from undispersed particles of colonies to mixtures of homogenoulsy dispersed fine and coarse particles (Fig. 4.12, 4.22). Simillar effects were observed by Spathis and Engler [58,60]. The higher temperature homogenized materials were expected to exhibit preferable recrystallization behaviour which was confirmed by annealing of the materials at intermediate gauges. A notable occurance was recrystallization and significant coarsening of grains in the surface layer of the higher temperature homogenized materials. This was later shown to

influence recrystallization behaviour of the thicker 600 μm material because the rolling process was not sufficient to suppress the formation of this layer.

An interesting point is the cause of softening during homogenization. A decrease of microhardness of the material was observed in materials homogenized at 420 °C and higher temperatures with the minimum value at 520 °C. Microhardness then remains constant within the limits of the experimental scatter.. It is clear that this is not the result of dispersion strengthening changes as particle distribution changes were the most significant in temperature ranges with constant microhardness.

Another possible explanation is that the material softens as a result of a change in the matrix solution concentration. Comparing the resistivity and microhardness curves (Fig. 5.2) shows that the decreases are by about 50 °C shifted on the temperature scale. The microhardness also does not increase at temperatures where the alloying elemetns diffuse back into the material.

This shift could be a result of vastly different annealing schematics of both experiments. However, an attempt to identify main softening mechanisms was made based on estimations of their individual values. For this purpose equations 2.1, 2.2 and 2.3 were used. Yield strength of pure aluminum has been reported to vary between 11 - 30 MPa with the most commonly reported value being 17 MPa [76]. The Hall-Petch constant k has been reported as 0.08 MPa.m$^{-1/2}$ [76]. The calculated components of yield strength were then converted into hardness using equation 3.2. The entire hardness is therefore calculated as

Figure 5.2: Results of an isothermal resistivity measurement and homogenized material's microhardness measurement

$$HV = 0.3(\sigma_0 + \sigma_{HP} + \sigma_{SS} + \sigma_{DH}) \tag{5.1}$$

where HP, SS and DH are Hall-Petch, solid solution and dispersion hardening component respectively. Due to lack a of recrystallization the Hall-Petch component remains constant. A diameter of (68 ± 7) μm was evaluated from the images in part 4.1.1. The solid solution is
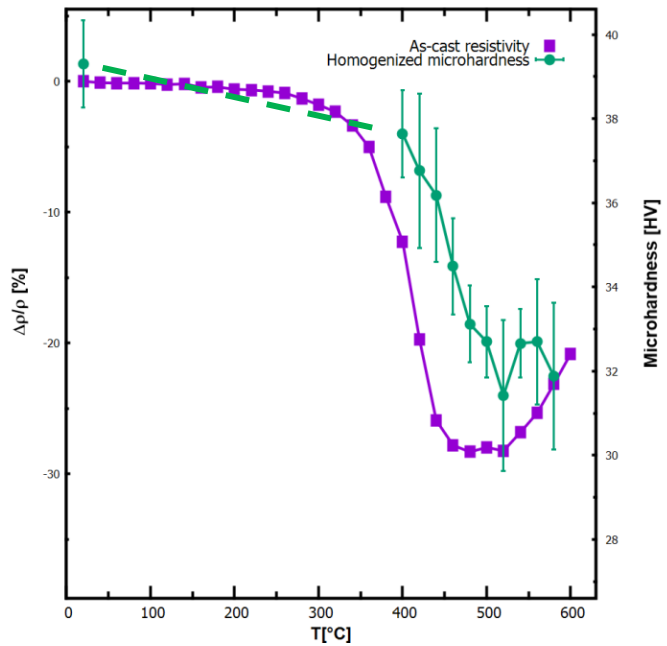
comprised of hardening by Fe and Si of which Si is assumed to remain constant however due to low concentrations it increases the value of microhardness in the range of units. Dispersion hardening changes only when particle changes are observed. Comparison of the calculated and measured hardness is in Fig. 5.3.

There is an increase in the calculated hardness at 500 °C and 520 °C. This is due to an issue with the thresholding proces of images through which the average spacing of particles and particle size is calculated. The LOM images do not provide enough about the size of individual particles to be measured while they remain in the original eutectic colonies. The average distance is also affected at these temperatures because most particles remain in the original colonies but new particles precipitate inside the eutectic grains. The evaluated spacing at these temperatures was approximately 0.8 μm. The particle spacing is also significantly less homogenous than at higher temperatures affecting the result. Estimations using increased average particle spacings are also presented in Fig. 5.3. The major decrease in hardness is facilitated by a decrease of solid solution strengthening. The solid solution component is presented in Fig. 5.4. The measured decrease of hardness was approximately 6 HV, which is the same as the calculated decrease through solid solution strengthening. The increase in solution

Figure 5.3: Microhardness measurement and calculated estimation in homogenized materials
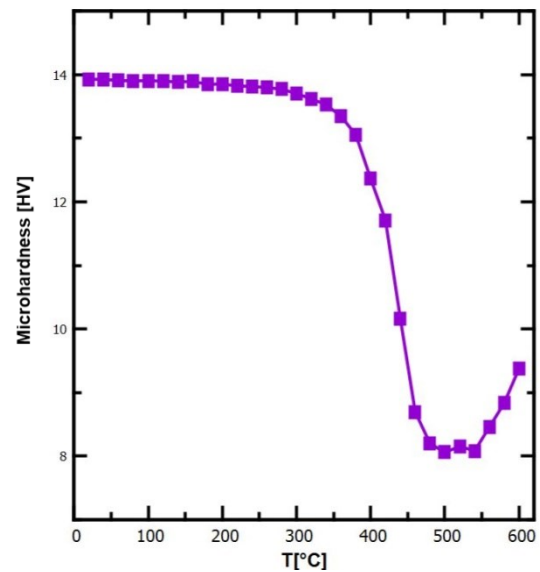
Figure 5.4: Solid solution strengthening element of material hardness

strenghtening at the end of the proces above 540 °C is compensated by a decrease of the dispersion strengthening during particles coarsening. The calculated hardness is overall lower however this could be resolved by using different values of pure aluminum yield strength and
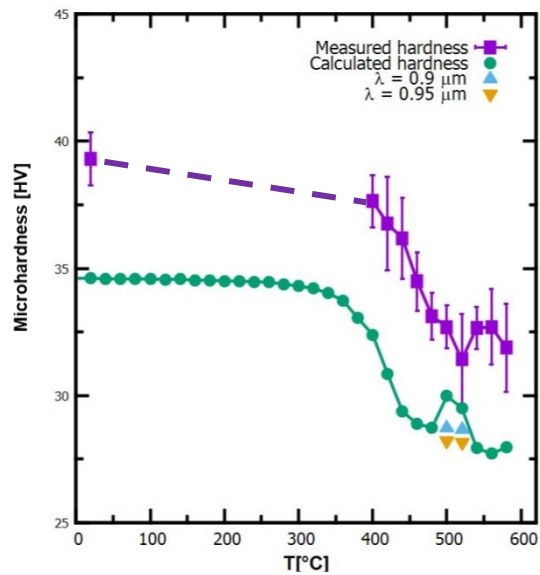
81

the Hall-Petch constant which have also been measured [76]. Finally since the concentration of Fe does not significantly change below 350 °C the calculated hardness does not either. This means that a slight decrease of the microhardness in this instantce is due to a recovery. The work hardening component was not evaluated due to a very low contribution to a total drop of the microhardness.

5.4. Resistivity measurements of the rolled material

The as-cast material matrix was depleted by the homogenization process as shown by the RRR measurement. However, at higher temperatures reversion of solutes into the matrix occurs (Fig. 4.7). These differently homogenized materials were then rolled, and resistivity measurements were repeated with the same effective heating rate. There is a variation in initial RRR value for these rolled materials, which correspond with the temperatures at which they were homogenized (Fig. 4.24). Specimen homogenized at 580 °C has the lowest initial RRR value and the one homogenized at 500 °C has the highest which is in accordance with the measurements performed on the as-cast material. However the values measured for the rolled materials are slightly higher than those for the as-cast strip indicating a higher purity material despite being significantly more cold worked and as such having higher dislocation density. The simplest explanation would be the experimental error. The values measured in nitrogen are significantly more precise than the ones measured in the 20 °C ethanol as the temperature of the nitrogen is stable and should be homogenous across the volume of the Dewar flask. The flask with ethanol is continuously kept at 20 °C however, there can be fluctuations of temperature present during the measurements. Measuring the material at 19 °C and 21 °C revealed a difference of about 1 % in the measured resistance values. Another error occurs as a result of thermal forces when the ends of the sample are at different temperatures. If we assume similar magnitude for both of these errors the difference in RRR values is still too high for the 600 µm rolled material. The initial values are overall lower for the 60 µm and would fall within the measurement error however these lower values could be explained by a higher degree of cold working of the material. Since there is no annealing during rolling there is also no expected change in the matrix saturation. The only remaining explanation is then the change in the distribution of particles is more homogenous due to rolling.

Once the rolled material is annealed the RRR increases. This can be attributed to the matrix being depleted of solutes however it increases for the 460 °C and 500 °C homogenized materials which should be theoreticaly well depleted during homogenization. This means that this increase most likely corresponds with other material changes. Given the cold working of

the material recovery of dislocation substructure seems to be the obvious one. The thicker materials experience about 10 % drop of resistivity (Fig. 4.25) while the thinner ones experience a 15 % drop (Fig. 4.26) during the annealing. Furthermore microhardness measurements were compared with these analyzed rezistivity curves (Fig. 5.5, 5.6). It appears resistivity decreases faster once recrystallization begins. Recovery is thus responsible for resistivity changes up to 300 °C. This decrease is approximately 5-10 % depending on the material. Assuming a $1.8x10^{-13}$ $\mu\Omega.cm^3$ contribution per unit dislocation density [43] and assuming that the contribution of dislocations to resistivity after recovery is 0 as dislocation density lowers by several degrees of magnitude the required dislocation density of the material would have to be about 10^{11} cm/cm^3 which is common for cold rolled materials as shown other authors [77 - 79]. This would explain the eariler increases or decreases of RRR or resistivity respetively for the thiner matterrials as those experience a higher degree of cold working.

Figure 5.5: Rezistivity and microhardness curves comparison for the material rolled to 600 μm homogenized at: a) 420 °C, b) 460 °C, c) 500 °C, d) 540 °C, e) 580 °C
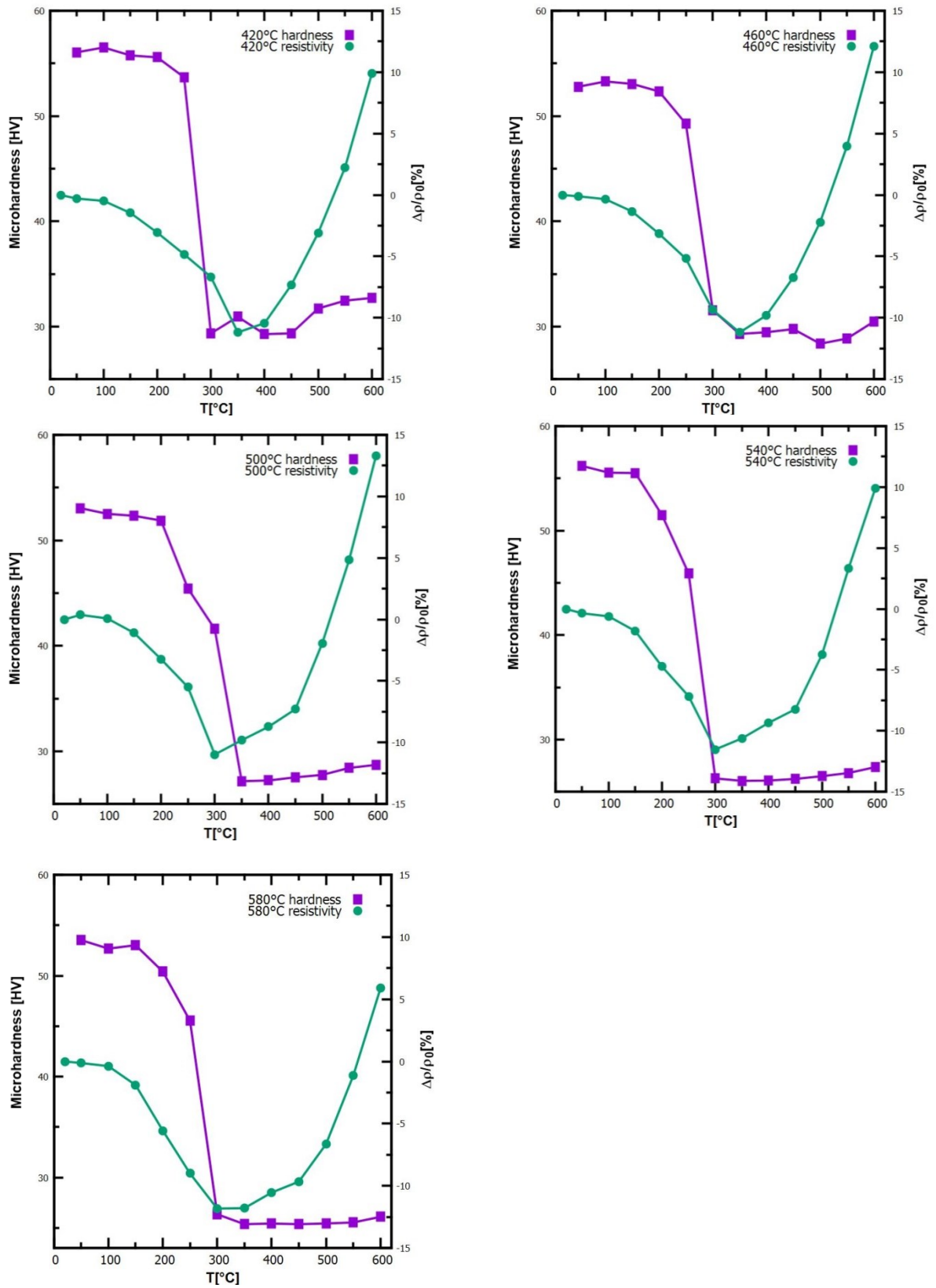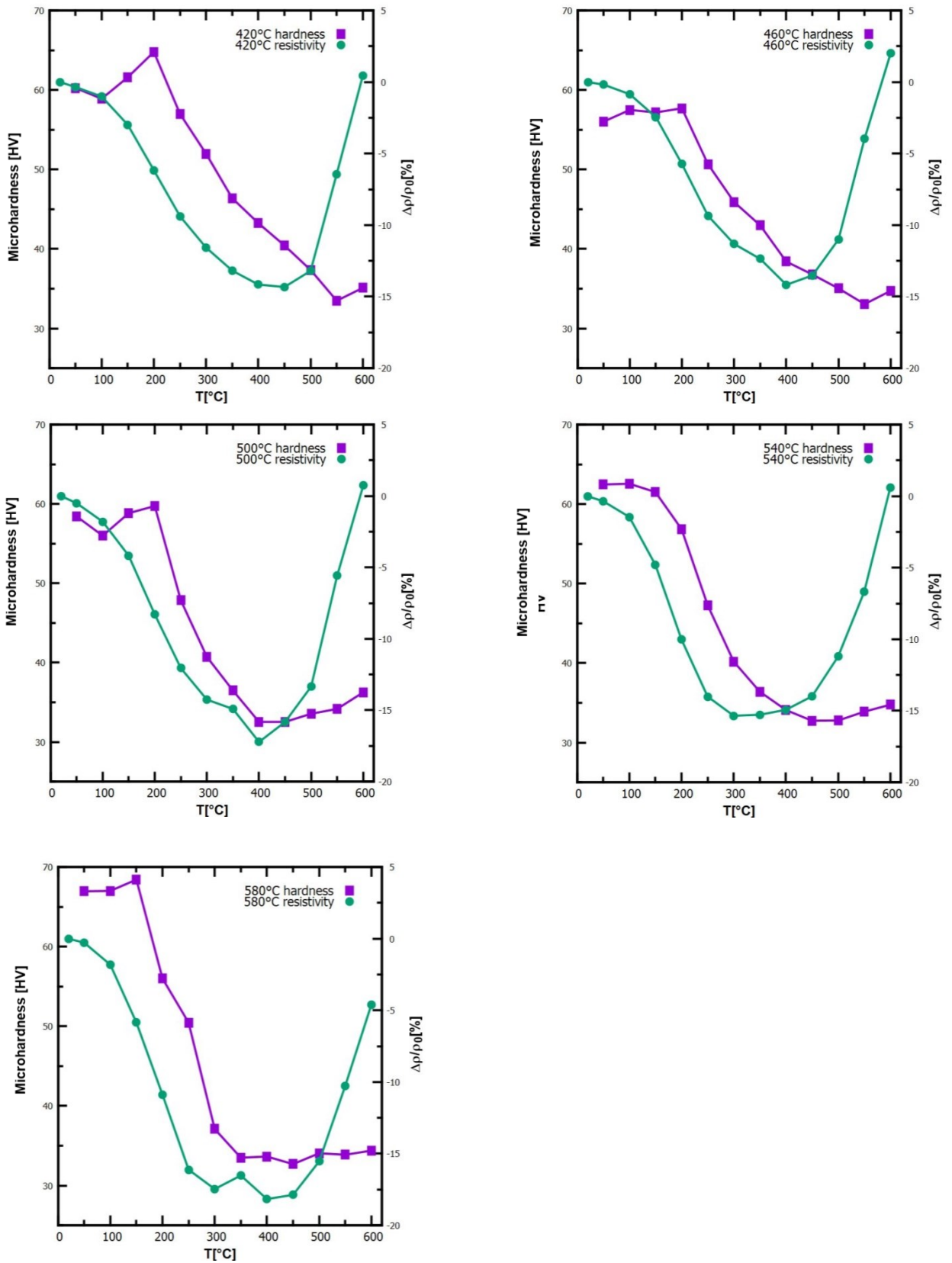
Figure 5.6: Rezistivity and microhardness curves comparison for the material rolled to 60 μm homogenized at: a) 420 °C, b) 460 °C, c) 500 °C, d) 540 °C, e) 580 °C

5.5. Recrystallization of the rolled material

For the isochronal recrystallization the LOM observations and microhardness measurements are mostly in line with each other with the exception of 420 °C homogenized which was rolled to 600 μm when annealed at 300 °C which already softened according to microhardness measurements however no recrystallization was observed despite both of these experiments being performed on the same sample. Other states are mostly in accordance with microhardness measurements showing instantaneous recrystallization in the case of the thicker materials and a recrystallization extended over larger temperature range in the case of the thinner materials.

There is a discrepancy however in the thicker materials showing higher microhardness values for the series that have coarser grains (Fig. 33) which is the opposite of what is expected according to the Hall-Petch equation (Eq. 2.1). To illustrate this, yield strength values were calculated from the microhardness measurements (Eq. 3.2) and plotted against inverted square root of grain size (Fig. 5.7). According to the Hall-Petch equation, the trendline should be an ascending straight line. However for these materials the yield strength either remains constant regardless of grain size or exhibits
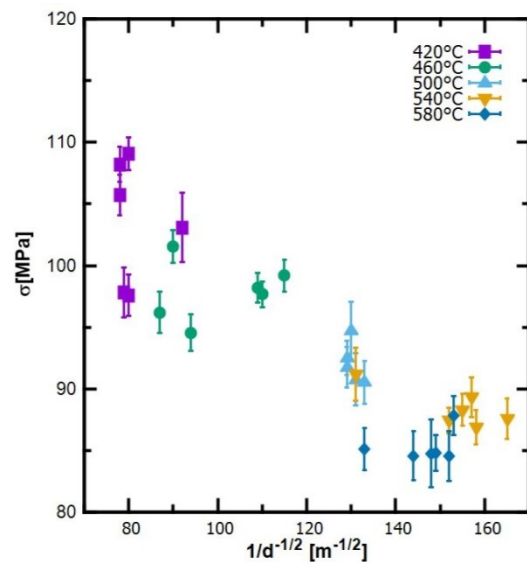
Figure 5.7: Hall-petch plot of the 600 μm rolled materials grain size

a large dispersion for materials which retain relatively constant grain size. This indicates the grain size is actualy a minor component of total material hardness. However, after the full recrystallization annealing the materials have the same Fe concentration in matrix and component of solid solution hardening is the same. This leaves dispersion hardening which as in the case of a stody of particular contributions in homogenized specimens exhibits contributions up to 2 HV which is not enough to explain the differences which are in the range of 10 HV. Similarly, a contribution of the dislocation substructure could be anulled after recrystallization. This anomalous behaviour where the material with highest grain size has the

highest hardness was not explained and remains a topic of further study.

The evaluated fractions and sizes of particles allow for calculations of Zener drag factor Z (Eq. 2.9). The calculations were made assuming a value of γ the grain boundary energy to be approximately 0.3 J/m^2 [80]. The calculated values are in Table 5.1. The average scatter of these values as discussed in part 4.4.4. is up to 30%.

	Z[kPa]	
	600 µm	60 µm
420 °C	37	43
460 °C	35	32
500 °C	31	32
540 °C	26	25
580 °C	21	24

Table 5.1: The values of Zener drag for different materials

With these values we can further estimate how the particle distribution affects recrystallization temperatures. The thicker material recrystallizes at 300 °C for most homogenization temperatures however, the 420 °C homogenized material recrystallizes at 350 °C. The calculated value of Zener drag for the material homogenized at 420 °C is about 75% higher than for the one homogenized at 580 °C. Using the equation for grain boundary mobility (Eq. 2.4) we can estimate a relative increase of the grain boundary mobility as a function relative to a selected temperature. According to these estimations grain boundary mobility only increases by about 18 % at 350 °C compared to 300 °C (Fig. 5.8). Similarly, the material homogenzied at 580 °C recrystallizes at 350 °C while the one homogenized at 420 °C only recrystallizes at 550 °C. There is a similar difference in Zener drag for the thinner materials of about 80%. However, there is an approximate 57% increase in grain boundary mobility between these temperatures (Fig. 5.8). While these values differ significantly it is important to
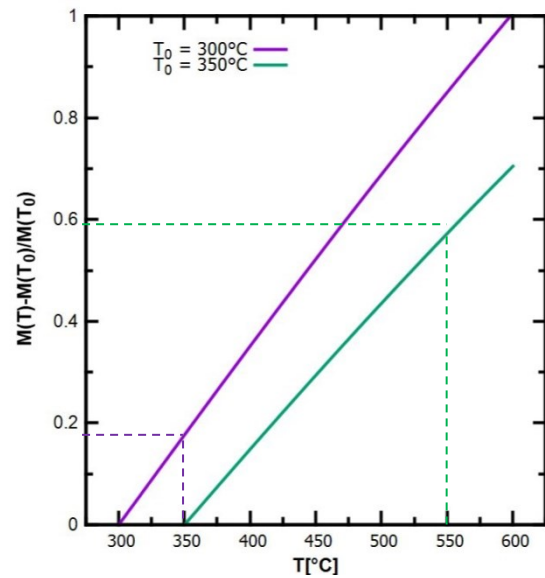

Figure 5.8: Relative grain boundary mobility increase

note the high measurement error of these values. Compounding the errors of size and fraction gives approximately 30% measurement error of Zener drag. Equation 2.5 is also only exact for a homgoenous distribution of spherical particles, neither of which holds exactly true for our material. In conlusion there is an increase of Zener drag in materials homogenized at lower temperatures which correlates with an increase in homogenization temperatures of these materials. however due to imperfect measurements and the differences in model assumptions and the materials state the exact effect on recrystallization could not be evaluated.

In the standard Avrami model the values of parameter n for the thicker material imply a 1D growth of grains however the grains have been observed to grow in both RD and ND. As stated in part 2.1.3. recovery could decrease the values of n to values between 1 and 2 even in materials with 3D growth of grains. The analysis of resistivity measurements (part 5.4.) confirms, that a high degree of recovery is responsible for a significant drop of hardness in all materials. Furthermore the presence of dispersoids and other defects can further retard recrystallization kinetics. Humphreys [81] specificaly quotes iron in aluminium alloys as an element that has a negative effect on recrystallization kinetics when present as a solute. He then further states that rate of recovery has a retarding effect on recrystallization as does inhomogenity of the deformation structure in the material.

Thinner material exhibits lower values of parameter n, although these materials are affected by the same composition and simillar particle distributions. Nevertheless, constrained volume and the role of a surface are additional parameters, which should be taken into account. As explained by Weinberg [17] high stored energy could promote inhomogenous recrystallization at the surface of the strip. Consequently, the process runs with significantly different kinetics from the one of a promary recrystallization and the rest of the process consists only of grain growth. The thinner material also shows a systematicly lower value of n during annealing at 275 °C. A possible origin of this effect is the influence of intensive recovery, which in heavily deformed Al materials creates fully recovered substructure with well developed and uniform subgrains resulting not only in an increase of strength of the material but also such a structure is less prone to recrystallization [82]. Due to the significant recovery the material loses it's driving force towards recrystallization.

5.6. Optimization of the production process

The temperatures for homogenization of foil stock materials are traditionaly in the 500 °C – 600 °C range on materials ~ 0,5 thick. Previous results support this practice as it seems that higher homogenization temperatures provide a finer recrystallized grain structure after rolling and annealing treatment. Similarly, softening annealing at an intermediate gauge is usualy performed at temperatures of about 360 °C for a sufficient softening to occur before the rollign to final gauge. However performing both annealing steps at lower temperatures is of commercial interest due to higher energy savings.

Our observations show, that optimal particle structure and distribution could improve recrystallization behavior through particle stimulated nucleation or Zener drag. Rather coarse particles (~1-3 μm) formed during homogenization at 540 °C or 580 °C support the formation of uniform recrystallized structure after intermediate annealing through PSN. This control of a final recrystallized structure is rather insensible to the reduction imposed by rolling before intermediate annealing.

Dispersion of finer particles, which is a most pronounced feature of materials homogenized at lower temperatures (420 °C or 460 °C), control the final grain size through ZD. However, to prevent abnormal grain growth at the temeperature of intermediate annealing it is necessary to impose larger reduction into the material. The resulting recrystallized structure is significantly finer than the one developed through PSN control. The management of optimal structure after intermediate annealing through ZD is more cost-effective however, it provides less stored deformation energy for the control of the last reduction step during rolling to the final gauge. This limited imposed stored energy could play a significant role in the homogenity of the microstructure and mechanical properties of the resulting foil after final degreasing annealing.

6. Conclusion

- Microstructure and mechanical properties were studied in a TRC strip prepared from AA8079 alloy. The study was focused mainly on the behavior of the material after different homogenization treatments and on the influence of the resulting microstructure on behavior of the material after rolling and recrystallization annealing simulating intermediate industrial annealing.

- The choice of the homogenization temperature influences mainly particle size, their morphology and dispersion. The as-cast material contains fine elongated intermetallic particles clustered into eutectic colonies. These particles transform at temperatures higher than 480 °C into spherical ones. A homogenous dispersion of coarse intermetallic particles forms above 500 °C.

- Different mechanisms contributing to a total strength of the material were identified and their magnitude was estimated.

- A significant impact of particle distribution on softening processes during annealing of rolled materials was proben and two main recrystallization controlling processes were identified – particle stimulated nucleation and Zener drag. Both processes could control the final structure.

- Optimization of the downstreaming process based on microstructural observations and physical properties analysis was proposed.

7. References

[1] KERRY, J. (2012). Aluminum foil packaging. *Packaging Technology*, *Fundamentals, Materials and Processes,* 163-177.

[2] HIND, A. R., BHARGAVA, S. K., et al. (1999). The surface chemistry of Bayer process solids: a review. *Colloids and Surfaces A: Physicochemical and Engineering Aspects*, **146**(1-3), 359-374.

[3] HATCH, J.E. (1984). Aluminum: Properties and physical metallurgy. American Society for Metals, Metals park, OH. ISBN 0-87170-176-6

[4] HANSEN, N. (2004). Hall-Petch Relation and Boundary Strengthening. *Scripta Materialia,* **51**(8), 801-806.

[5] FLEISGHER, R. L. (1961). Solution Hardening. *Acta Metallurgica*, **9**(11), 996-1000.

[6] ERICSSON, T. (1966). On the Suzuki Effect and Spinodal Decomposition. *Acta Metallurgica*, **14**(9), 1079-1084.

[7] UESUGI, T., HIGASHI, K. (2010). Modeling solid solution strengthening using first-principles results of misfit strain with Friedel model in Al-based alloys. *Proceedings of the 12th international conference on Aluminium alloys*, 1421-1425.

[8] HORNBOGEN, E. (2001). Hundred Years of Precipitation Hardening. *Journal of Light Metals*, **1**(2), 127-132.

[9]ŠMILAUEROVÁ, J. Lecture on precipitation hardening https://material.karlov.mff.cuni.cz/people/smilauerova/vyuka/FyzMat_I/FyzMat_I_7_precipitates.pdf [accessed. 25.05.2020]

[10] KRATOCHVÍL, P., LUKÁČ, P. a SPRUŠIL, B. (1984). *Úvod do fyziky kovů*.SNTL/Alfa - Nakladatelství technické literatury, Prague.

[11] HIRSCHHORN, J. S. (1963). Stacking faults in the refractory metals and alloys — A review. *Journal of the Less Common Metals*, **5**(6), 493-509.

[12] A table of stacking fault energies of commonly used metals http://www.engineeringenotes.com/metallurgy/defects-metallurgy/surface-defects-in-crystals-3-types-metallurgy/43279 [accessed 17.12.2019]

[13]SEDLÁČEK, V. et al. (1985). *Zotavení a rekrystalizace*. Academia, Prague..

[14] WEINBERG, M. C., DUNBAR, P., et al. (1997). Crystallization kinetics and the JMAK equation. *Journal of Non-Crystalline Solids*, **219**, 89-99.

[15]KALU, P. N., WARYOBA, D. R. (2007). A JMAK-microhardness model for quantifying the kinetics of restoration mechanisms in inhomogeneous microstructure. *Materials Science and Engineering: A*, **464(1-2)**, 68-75

[16]FIELD, D.P., BEHRENS, L., ROOT, J.M. (2009). Identification of Particle Stimulated Nucleation during Recrystallization of AA 7050. *Computers, Materials and Continua,* **14(3)**, 171-184.

[17]WEINBERG, C. B., et al. (1997). Crystallization kinetics and the JMAK equation. *Journal of Non-Crystalline Solids*, **219**, 89-99.

[18]MATSUI, T., OGAWA, T., ADACHI, Y. (2019). Relationship between three-dimensional microstructure and Avrami exponent for recrystallization in pure iron. *Results in Materials,* **1**.

[19]TAJALLY, M., HUDA, Z. (2011). Recrystallization kinetics for aluminum alloy 7075. *Metal Science and Heat treatment*, **53**, 213-217.

[20]KALU, P., WARYOBA, D. (2007). A JMAK-microhardness model for quantifying the kinetics of restoration mechanisms in inhomogeneous microstructure. *Materials Science and Engineering: A*, **464(1-2)**, 68-75.

[21] HILLERT, M. (1965). On the Theory of Normal and Abnormal Grain Growth. *Acta Metallurgica*, **13**(3), 227-238.

[22] TROEGER, L. P., STARKE, E. A. jr. (2000). Particle-stimulated nucleation of recrystallization for grain-size control and superplasticity in an Al–Mg–Si–Cu alloy. *Materials Science and Engineering: A*, **293**(1-2), 19-29.

[23]HUMPHREYS, F. J. (1977). The nucleation of recrystallization at second phase particles in deformed aluminium. *Acta Metallurgica*, **25(11)**, 1323-1344.

[24]NES, E., RYUM N., HUNDERI, O. (1985). On the Zener drag. *Acta Metallurgica*, **33(1)**, 11-22..

[25]Foundry lexicon – strengthening mechanisms overview: https://www.giessereilexikon.com/en/foundry-lexicon/Encyclopedia/show/strengthening-mechanisms-4698/?cHash=a1de8b3f251a87d649ec6d341ee39d8d [accessed 28.05.2020]

[26]ZHANG, Y., et al. (2012). Three-dimensional investigation of recrystallization nucleation in a particle-containing Al alloy. *Scripta Materialia*, **67(4)**, 320-323.

[27]RATKE, L., VOORHEES, P. W. (2013). Growth and Coarsening: Ostwald Ripening in Material Processing. Springer. ISBN-13: 978-3540425632.

[28]VOORGEES, P. W. (1985). The Theory of Ostwald Ripening. *Journal of Statistical Physics*, **38**, 231-252.

[29]HUANG, W. H., OU, B.L. (2009). Evolution of precipitation during different homogenization treatments in a 3003 aluminum alloy. *Materials and Design*, **30(7)**, 2685-2692.

[30] DAVIS, J.R. (2001). Aluminum and Aluminum Alloys. *Alloying: Understanding the Basics,* 351-416.

[31] SHARMA, A., JAE, P. (2016). Possibility of Al-Si Brazing Alloys for Industrial Microjoining Applications. *Journal of the Microelectronics and Packaging Society,* **24**, 35-40.

[32] HENAGER, CH. H. (2007). *Materials for the Hydrogen Economy.* CRC Press, Boca Raton. ISBN 9780429123283

[33] SKJERPE, P. (1987). An Electron Microscopy Study of the Phase Al_3Fe. *Journal of Microscopy,* **148**(1), 33-50.

[34] HAN, Y., BAN, CH., et al. (2007). Alignment behavior of primary Al_3Fe phase in Al–Fe alloy under a high magnetic field. *Materials Letters*, **61**(4-5), 983-986.

[35] LIANG, D., JONES, H. (1993). Morphologies of primary Al_3Fe in Bridgman solidification and TIG weld traversing of hypereutectic AlFe alloys. *Materials Science and Engineering: A*, **173**(1-2), 109-114.

[36] ROY, R. K., KAR, S., DAS, K., DAS, S. (2006). A study of precipitation and recrystallization behaviour of aluminium alloy AA1235. *Journal of Materials Science,* **41**, 1039-1045.

[37] KIM, D. H., CANTOR, B. (1994). Structure and decomposition behaviour of rapidly solidified Al-Fe alloys. *Journal of Materials Science,* **29**, 2884-2892.

[38] GOULART, R. P., SPINELLI, J. E., et al. (2010). The effects of cell spacing and distribution of intermetallic fibers on the mechanical properties of hypoeutectic Al–Fe alloys. *Materials Chemistry and Physics*, **119**(1-2), 272-278.

[39]KUIJPERS, N. C. W., et al. (2005). The dependence of the β-AlFeSi to α-Al(FeMn)Si transformation kinetics in Al–Mg–Si alloys on the alloying elements. *Materials Science and Engineering: A*, **394(1)**, 9-19.

[40] KUIJPERS, N. C. W., KOOL, W. H., et al. (2002). Assessment of different techniques for quantification of α-Al(FeMn)Si and β-AlFeSi intermetallics in AA 6*xxx* alloys. *Materials Characterization,* **49**(5), 409-420.

[41] KIM, H. Y., PARK, T. Y., et al. (2006). Effects of Mn on the crystal structure of α-Al(Mn,Fe)Si particles in A356 alloys. *Journal of Crystal Growth*, **291**(1), 201-211.

[42] KITTEL, Ch. (1985). *Úvod do fyziky pevných látek*. Academia, Prague.

[43] HAŠLAR, V. (1983). Vliv podmínek deformace na produkci a zotavování mřížkových poruch v kovech deformovaných za studena.Univerzita Karlova, Katedra Fyziky Kovů, Praha.

[44] KELES, O., DUNDAR, M. (2007). Aluminum foil: Its typical quality problems and their causes. *Journal of Materials Processing Technology*, **186(1-3)**, 125-137.

[45] NADELLA, R., et al. (2008). Macrosegregation in direct-chill casting of aluminium alloys. *Progress in Materials Science*, **53(3)**, 421-480.

[46] YUN, M., LOKYER, S., HUNT, J. D. (2000). Twin Roll Casting of Aluminum Alloys. *Materials Science and Engineering: A*, **280**(1), 116-123.

[47] COOK, R., GROCOCK, P. G. et al. (1995). Development of the twin-roll casting process. *Journal of Materialls Processing Technology*, **55**(2), 76-84.

[48] HAGA, T., TKAHASHI, K., et al. (2004). Twin roll casting of aluminum alloy strips, *Journal of Materials Processing Technology*, **153-154**, 42-47.

[49] SONG, R., HARADA, Y., KUMAI, S. (2017). Influence of cooling rate on primary particle and solute distribution in high speed twin-roll cast Al-Mn based alloy strip. *Materials Transactions*, **51(1)**, 110-116.

[50] Science Direct overview – what is Centreline Segregation
https://www.sciencedirect.com/topics/engineering/centerline-segregation
[accessed 28.05.2020]

[51] LV, Z., DU, F., et al. (2015) Centerline segregation mechanism of twin-roll cast A3003 strip. *Journal of Alloys and Compounds*, **643**, 270-274.

[52] BIROL, Y. (2009). Analysis of macro segregation in twin-roll cast aluminium strips via solidification curves. *Journal of Alloys and Compounds,* **486**(1-2), 168-172.

[53] SANDERS, R. E. jr., HOLLINSHEAD, P. A., SIMIELLI, E. A. (2004). Industrial Development of Non-Heat Treatable Aluminum Alloys. *Proceedings of the 9th International Conference on Aluminium Alloys*, 53-64.

[54] GUAN, R., TIE, D. (2017). A Review on Grain Refinement of Aluminum Alloys: Progresses, Challenges and Prospects. *Acta Metallurgica Sinica*, **30**(5), 409-432.

[55] MALCIOGU, A. U., DOGAN, C., et al. (2019). Effects of Casting Speed on Thin Gauge Foil Surface Quality of 8079 Aluminum Alloy Produced by Twin Roll Casting Method. *Transaction of the Indian Institute of Metals*, **72**, 1001-1011.

[56] BIROL, Y. (2008). Thermomechanical processing of a twin-roll cast Al–1Fe–0.2Si alloy. *Journal of Materials Processing Technology*, **202**(1-3), 564-568.

[57]BIROL, Y. (2009). Homogenization of a twin-roll cast thin Al–Mn strip. *Journal of Alloys and Compounds*, **471(1-2)**, 122-127.

[58]SPATHIS, D., SPIROS, J. (2013). The influence of casting speed in the as cast strip mechanical properties of 8079 and 8006 alloys. *Light Metals 2013*, 305-309.

[59] LENTZ, M., LAPTYEVA, G., ENGLER, O. (2016). Characterization of second-phase particles in two aluminium foil alloys. *Journal of Alloys and Compounds*, **660**, 276-288.

[60]ENGLER, O., AEGERTER, J., CALMER, D. (2020) Control of texture and earing in aluminium alloy AA 8011A-H14 closure stock . *Materials Science and Engineering: A,* **775**.

[61] BIROL, Y. (2009) Recrystallization of twin-roll cast Al–Fe–Si foil stock processed without homogenization. *Journal of alloys and compounds*, **488(1)**, 112-116.

[62]ALLEN, C.M., et al. (1998). Intermetallic phase selection in 1XXX Al alloys. *Progress in Materials Science*, **43(2)**, 89-170.

[63]SHAKIBA, M., PARSON, N., CHEN, X. G. (2014). Effect of homogenization treatment and silicon content on the microstructure and hot workability of dilute Al–Fe–Si alloys.

[64] BIROL, Y. (2009). Interannealing twin-roll cast Al–Fe–Si strips without homogenization. *Scripta Materialia*, **61**(2), 185-188.

[65] BIROL, Y. (2008). Response to annealing treatments of twin-roll cast thin Al–Fe–Si strips. *Journal of Alloys and Compounds,* **458**(1-2), 265-270

[66] Struers firm site – OPS suspension
https://e-shop.struers.com/FI/EN/products/Polishing/Silica_Oxide/OP-S_004_m_1_l(40700000).aspx [accessed 28.05.2020]

[67] CERRI, E., EVANGELISTA, E. (1999). Metallography of Aluminium Alloys. *Talat Lecture 1202.*

[68] Barker Etch method – official Struers company website
https://www.struers.com/en/Knowledge/Etching#etching-how-to

[69] Encyclopetia Britannica – what is Vickers Hardness
https://www.britannica.com/science/Vickers-hardness [accessed 28.05.2020]

[70]Vicker's hardness to yield strength conversion http://www.tribonet.org/hardness-calculation-vickers-indenter [accessed 28.05.2020]

[71] CIESLAR, M., VOSTRÝ, P., et al. (1997). Inhomogeneity of mechanical properties and deformation instabilities in Al-Cu-Li-Mg alloy. *Materials Science and Engineering: A*, **234-**

236, 790-793.

[72] JIANG, F., ZUROB, H. S., et al. (2016) Characterizing precipitate evolution of an Al–Zn–Mg–Cu-based commercial alloy during artificial aging and non-isothermal heat treatments by *in situ* electrical resistivity monitoring. *Materials Characterization*, **117**, 47-56.

[73]CAN, A., ARIKAN, H. (2016). Analysis of twin-roll casting AA8079 alloy 6.35-μm foil rolling process. *Materials and Technologies*, **50(6)**, 861-868.

[74]SPATHIS, D., SPIROS, J. (2013). The influence of casting speed in the as cast strip mechanical properties of 8079 and 8006 alloys. *Light Metals 2013*, 305-309.

[75]ALSHABAT, N., AL-QAWABAH, S. (2015). Effect of 4%wt. Cu Addition on the Mechanical Characteristics and Fatigue Life of Commercially Pure Aluminum. *Jordan Journal of Mechanical and Industrial Engineering*, **9(4)**, 297-301.

[76] T.SHANMUGASUNDARAM et al. (2010). On the Hall–Petch relationship in a nanostructured Al–Cu alloy. *Materials Science and Engineering A*, **527(29-30)**, 7821-7825.

[77]ZUIKO, I., KAIBYSHEV, R. (2017) Deformation structures and strengthening mechanisms in an Al-Cu alloy subjected to extensive cold rolling. *Materials Science and Engineering A*, **702**, 53-64.

[78]GUYOT, P., RAYNAUD, G. M. (1991). Dislocation structure distributions and properties of heavily cold rolled aluminum and aluminum-magnesium alloys. *Acta Metallurgica et Materialia*, **39(3)**, 317-322.

[79]DE SOUSA, T. G., SORDI, V. L., BRANDAO, L. P. (2018) Dislocation density and texture in copper deformed by cold rolling and ECAP. *Materials Research*, **21**.

[80]University of Cambridge: Zener Drag https://www.phase-trans.msm.cam.ac.uk/2005/Zener/ [accessed 28.05.2020]

[81]HUMPHREYS, F. J., HATHERLY, M. (2004). Recrystallization and related annealing phenomena – second edition. ELSEVIER Ltd, Kidlington, Oxford OX5 1GB, UK. ISBN: 0 08 044164 5

[82]CIESLAR, M., POKOVÁ, M. (2014). Annealing Effects in Twin-Roll Cast AA8006 Aluminium Sheets Processed by Accumulative Roll-Bonding. *Materials,* **7(12)**, 8058-8069.